

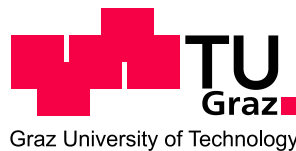
**Stephanie Rožker, BSc**

# **Fabrication of multiphase artificial cellulose substrates for AFM based real time investigations of enzymatic degradation**

## **MASTER THESIS**

For obtaining the academic degree  
Diplom-Ingenieurin

Master Programme of  
Technical Physics



**Graz University of Technology**

Supervisor:

Ao.Univ.-Prof. Dipl.-Ing. Dr.techn. Gerald Kothleitner

Co-Supervisor:

Dipl.-Ing. Dr.techn. Harald Plank

Institute of Electron Microscopy and Nanoanalysis

Graz, December 2013

Deutsche Fassung:  
Beschluss der Curricula-Kommission für Bachelor-, Master- und Diplomstudien vom 10.11.2008  
Genehmigung des Senates am 1.12.2008

## EIDESSTÄTTLICHE ERKLÄRUNG

Ich erkläre an Eides statt, dass ich die vorliegende Arbeit selbstständig verfasst, andere als die angegebenen Quellen/Hilfsmittel nicht benutzt, und die den benutzten Quellen wörtlich und inhaltlich entnommenen Stellen als solche kenntlich gemacht habe.

Graz, am .....

.....  
(Unterschrift)

Englische Fassung:

## STATUTORY DECLARATION

I declare that I have authored this thesis independently, that I have not used other than the declared sources / resources, and that I have explicitly marked all material which has been quoted either literally or by content from the used sources.

.....  
date

.....  
(signature)

# Abstract

The second generation of biofuels produced from cellulose is an alternative to renewable resources that are based on the fermentation of material otherwise used in food production. The abundance of cellulose in the biosphere makes it an ideal candidate for environmental friendly biofuels. On the other hand, the recalcitrance of this biological polymer causes the hydrolytic degradation process triggered by enzymes (cellulases) to be rather inefficient.

This work focuses on real time investigations of enzymatic degradation of cellulose via atomic force microscopy (AFM) in liquid environments to provide approaches to improve the production of the second generation of biofuels. This method necessitates artificial, nano-flat cellulose samples which feature both amorphous and crystalline phases of cellulose. The hitherto utilized substrates derive from solving microcrystalline cellulose (Avicel) in an ionic liquid followed by removal of the solvent and embedding in epoxy. For nano-flat surfaces the samples are cut by ultramicrotomy. The control over the properties of the substrate, especially over size, content, and distribution of the crystalline features, is improved. Enzymatic degradation experiments that investigate the influence of the family 61 glycoside hydrolase (GH61) on cellulose and cellulases from the fungi *Trichoderma reesei* are conducted. The increase in activity of the cellulases endo-glucanase 1 (EG1), cellobiohydrolase 2 (CBH2) and the supernatant SVG is proven. Throughout this experimental series it turns out that the enhanced samples are not entirely suitable for the structural and quantitative analysis of the enzymatic degradation of cellulose. Further substrate development is required. This leads to the introduction of spin cast cellulose samples. Nano-crystalline cellulose features are embedded in an amorphous cellulose matrix. The solvent is removed by spin casting the solution onto a silicon wafer which implicates the formation of nano-flat surfaces. The new substrates are characterized by light microscopy, X-ray diffraction, Raman spectroscopy, scanning electron microscopy, transmission electron microscopy and atomic force microscopy in liquid environments. Enzymatic degradation experiments conducted on the tunable, quickly prepared spin cast samples reveal their compelling suitability for detailed structural and quantitative analysis in all respects. Progress in comprehension of the enzymatic degradation process will be facilitated by this development in the preparation of artificial cellulose substrates.

# Kurzfassung

Biokraftstoffe der zweiten Generation aus Cellulose sind eine Alternative für erneuerbare Energieträger, die auf der Fermentation von Stoffen basieren, die ansonsten für die Lebensmittelproduktion verwendet werden. Das reichhaltige Vorkommen von Cellulose in der Biosphäre macht sie zu einem idealen Kandidaten für umweltfreundliche Brennstoffe. Durch die schwere Erschließbarkeit dieses biologischen Polymers ist der von Enzymen (Cellulasen) ausgelöste, hydrolytische Abbauprozess allerdings relativ ineffizient.

Diese Arbeit konzentriert sich auf Echtzeituntersuchungen des enzymatischen Abbaus von Cellulose mit Hilfe von Rasterkraftmikroskopie (AFM) in flüssiger Umgebung, um Ansätze zur Optimierung in der Produktion der Biokraftstoffe der zweiten Generation zu liefern. Diese Methode verlangt artifizielle, nanoflatte Cellulose-Substrate, die sowohl amorphe als auch kristalline Cellulose-Phasen aufweisen. Die bisher eingesetzten Substrate stammen aus der Lösung mikrokristalliner Cellulose (Avicel) in einer ionischen Flüssigkeit gefolgt von der Entfernung des Lösungsmittels und der Einbettung in Epoxidharz. Um nanoflatte Oberflächen zu erhalten, werden die Proben mittels Ultramikrotomie angeschnitten. Die Kontrolle über die Eigenschaften der Substrate, insbesondere über Größe, Anteil und Verteilung der kristallinen Merkmale, wird verbessert. Enzymatische Abbauxperimente, die den Einfluss der Familie 61 der Glycosidasen (GH61) auf Cellulose und Cellulasen aus dem Pilz *Trichoderma reesei* untersuchen, werden durchgeführt. Der Aktivitätsanstieg der Cellulasen Endoglucanase 1 (EG1), Cellobiohydrolase 2 (CBH2) und des Überstands SVG wird erwiesen. Während dieser experimentellen Serie stellt sich heraus, dass die verbesserten Proben nicht gänzlich für die strukturelle und quantitative Analyse des enzymatischen Abbaus von Cellulose geeignet sind. Dies erfordert die weitere Entwicklung des Substrats und führt zur Einführung der Spin-Cast-Cellulose-Proben. Nanokristalline Cellulose-Charakteristika werden in einer Matrix aus amorpher Cellulose eingebettet. Das Lösungsmittel wird entfernt, indem die Lösung im Spin-Casting-Verfahren auf einen Siliziumwafer aufgebracht wird, was die Ausformung nanoflatter Oberflächen zur Folge hat. Die neuen Substrate werden mittels Lichtmikroskopie, Röntgendiffraktion, Ramanspektroskopie, Rasterelektronenmikroskopie, Transmissionselektronenmikroskopie und Rasterkraftmikroskopie in flüssiger Umgebung charakterisiert. Enzymatische Abbauxperimente werden auf einstellbaren, schnell hergestellten Spin-Cast-Proben durchgeführt und zeigen deren überzeugende Eignung für die detaillierte strukturelle und quantitative Analyse in allen Belangen. Diese Entwicklung in der Präparation artifizieller Cellulose-Substrat ermöglicht somit Fortschritte im Verständnis des enzymatischen Abbauprozesses.

# Acknowledgments

Many people contributed to the success of this thesis.

First I would like to thank the head of the Institute of Electron Microscopy and Nanoanalysis Prof. Ferdinand Hofer and the head of the Institute of Biotechnology and Biochemical Engineering Prof. Bernd Nidetzky for the opportunity to work in this interdisciplinary group. I also wish to thank Prof. Gerald Kothleitner for his supervision.

I would like to express my gratitude to Dr. Harald Plank for his invaluable guidance, encouragement and motivation. In numerous discussions he has taught me a lot.

Special thanks goes to DI Thomas Ganner for his assistance and advice, the substrate preparation, the supporting experiments and the Pacman idea.

I also want to thank DI Timothy Aschl for his initial introductions and DI Manuel Eibinger of the Institute of Biotechnology and Biochemical Engineering for his biochemical support and for providing the enzymes.

I wish to thank Ing. Claudia Mayrhofer for performing the ultramicrotomy cuts, Dr. Boril Chernev for the Raman measurements, Mag. Johanna Kraxner for the TEM images and Dr. Stefan Mitsche for his support with XRD.

A special thanks of mine goes to the members of the lab crew for their assistance with the substrate preparation and to the rest of the FELMI staff for the good atmosphere at the institute.

Last but not least I would like to express my gratitude to my family and friends for their support and constant motivation.

# Table of Content

|        |   |    |
|--------|---|----|
| 1      | Introduction.....                         | 1  |
| 2      | Biological & chemical fundamentals .....  | 2  |
| 2.1    | Cellulose .....                           | 2  |
| 2.1.1  | Molecular structure .....                 | 2  |
| 2.1.2  | Supramolecular structure .....            | 3  |
| 2.1.3  | Morphological structure .....             | 4  |
| 2.2    | Cellulases .....                          | 4  |
| 2.2.1  | CBH1 (Cel7A) .....                        | 6  |
| 2.2.2  | CBH2 (Cel6A) .....                        | 6  |
| 2.2.3  | EG1 (Cel7B) .....                         | 6  |
| 2.2.4  | Supernatant (SVG).....                    | 7  |
| 2.2.5  | GH61 (AA9, PMO).....                      | 7  |
| 3      | Experimental techniques .....             | 8  |
| 3.1    | Atomic Force Microscopy .....             | 8  |
| 3.1.1. | Principle .....                           | 8  |
| 3.1.2. | Components .....                          | 8  |
| 3.1.3. | Effective forces in AFM .....             | 11 |
| 3.1.4. | Operation modes .....                     | 12 |
| 3.2    | X-ray diffractometry .....                | 14 |
| 3.3    | Raman spectroscopy .....                  | 15 |
| 3.4    | Transmission electron microscopy.....     | 15 |
| 3.5    | Scanning electron microscopy & EDX.....   | 16 |
| 4      | Sample preparation.....                   | 17 |
| 4.1    | Ultramicrotomy .....                      | 17 |
| 4.2    | FSEC.....                                 | 18 |
| 4.3    | Spin casting.....                         | 19 |
| 4.4    | Spin cast cellulose – TMSC.....           | 19 |
| 4.5    | Spin cast cellulose – NCC.....            | 19 |
| 5      | Strategy overview.....                    | 21 |
| 6      | Experiments.....                          | 22 |
| 6.1    | Further developments of FSEC samples..... | 23 |
| 6.1.1  | LIMI of FSEC .....                        | 24 |
| 6.1.2  | XRD of FSEC .....                         | 24 |

|         |  |    |
|---------|--|----|
| 6.1.3   | Raman spectroscopy of FSEC.....                              | 25 |
| 6.1.4   | AFM of FSEC.....   | 27 |
| 6.1.5   | Summary FSEC.....  | 28 |
| 6.2     | GH61 experiments.....  | 29 |
| 6.2.1   | Supernatant on FSEC1.....                                    | 29 |
| 6.2.2   | EG1 on FSEC1 and FSEC2.....                                  | 32 |
| 6.2.3   | CBH2 on FSEC2.....   | 34 |
| 6.2.4   | CBH1 on FSEC2.....   | 37 |
| 6.2.5   | Summary GH61 experiments of FSEC1 and FSEC2.....             | 43 |
| 6.3     | Spin cast cellulose.....                                     | 45 |
| 6.3.1   | TMSC.....  | 45 |
| 6.3.1.1 | XRD of TMSC.....   | 45 |
| 6.3.1.2 | Raman spectroscopy of TMSC.....                              | 46 |
| 6.3.1.3 | Thickness estimation of TMSC via LIM1.....                   | 46 |
| 6.3.1.4 | AFM of TMSC.....   | 47 |
| 6.3.1.5 | Enzymatic degradation experiments on TMSC.....               | 52 |
| 6.3.2   | NCC.....   | 54 |
| 6.3.2.1 | Raman spectroscopy of NCC.....                               | 54 |
| 6.3.2.2 | SEM and TEM of NCC.....                                      | 55 |
| 6.3.2.3 | AFM of pre-filtered spin coated NCC in dry environments..... | 56 |
| 6.3.2.4 | Enzymatic degradation experiments on NCC.....                | 58 |
| 6.3.3   | TMSC/NCC.....  | 61 |
| 6.3.3.1 | Enzymatic degradation experiments on TMSC/NCC.....           | 62 |
| 6.3.4   | Summary and outlook SCC.....                                 | 65 |
| 7       | Summary.....   | 67 |
| 8       | Outlook.....   | 69 |
| 9       | List of abbreviations.....                                   | 70 |
| 10      | List of tables.....  | 71 |
| 11      | List of figures.....   | 72 |
| 12      | Bibliography.....  | 77 |

# 1 Introduction

The mineral oil reservoirs are predicted to run dry in the foreseeable future. This gives rise to the need for renewable resources. Concerning fuels, blending of biofuels made from crops is widely implemented across the world. These so-called first generation biofuels are a highly controversial topic as plants otherwise used for food production are turned into fuels. Here cellulose comes into play, which is the most abundant material in the biosphere [1] and thus more or less infinitely available. This biological polymer consists of glucose and cannot be digested by most mammals which makes it an interesting, morally unproblematic material for the ethanol fermentation. The production of biofuels by degrading cellulose into its main components (glucose) followed by fermentation is known as the second generation of biofuels. The degradation process is based on the enzymatic hydrolysis of cellulose by cellulases. However, cellulose is insoluble in water and most organic solvents [1]. This causes the process to be rather inefficient.

The purpose of this thesis is to conduct fundamental research in the field of enzymatic degradation of cellulose to provide approaches to improve the production of the second generation of biofuels. This is realized by conducting real time enzymatic degradation experiments in liquid environments which are observed by atomic force microscopy (AFM). For such investigations, nano-flat samples have to be used which can only be produced artificially. These artificial cellulose substrates have to represent natural circumstances in an optimal way, i.e. they have to exhibit both crystalline and amorphous structures. Suitable substrates have been introduced and well-studied in former works by J. Dohr [2], T. Ganner [3] and T. Aschl [4]. The focus in this thesis is placed on the development of the cellulose substrates to allow detailed structural and quantitative analysis of the degradation process. In this respect a new interesting enzyme (GH61) and its effects on cellulose and on the activity of cellulases from the fungi *Trichoderma reesei* are studied. These investigations will lead to the introduction of a new type of substrate, which is quickly prepared by the spin casting method and fully tunable. In numerous characterization experiments that involve light microscopy (LIM), X-ray diffraction (XRD), Raman spectroscopy, scanning electron microscopy (SEM), transmission electron microscopy (TEM), and atomic force microscopy the new substrate turns out to exhibit all required properties (nano-flat, crystalline and amorphous features, absolute markers of height for quantitative measurements). Subsequent enzymatic degradation experiments reveal that the new spin cast cellulose samples are an excellent alternative to the hitherto utilized samples and allow unprecedented possibilities of observing the degradation process in great structural and quantitative detail. By that, the main findings within this thesis represent an essential step towards real time tracking of single enzymes.

## 2 Biological & chemical fundamentals

### 2.1 Cellulose

Cellulose is a biological polymer with the empirical formula  $C_6H_{10}O_5$  of the repeat unit. Together with the natural products of starch and sugar it belongs to the group of carbohydrates [5]. Cellulose is produced by certain algae, bacteria and fungi and forms the main component in cell walls of higher plants. That makes cellulose the most naturally occurring material in the biosphere [1] with an annual production (and degradation [6]) of approx.  $10^{12}$  tons.

Before its scientific discovery in 1838 humans widely used cellulose for generation of energy, as construction material (wood) and for clothing. Cellulose is the raw material in paper production and the basis for packing material (cellophane), fabrics (viscose), and plastics (celluloid, one of the first plastics/thermoplasts) [7].

Whereas starch and sugar are integral parts of nutrition, most mammals are not able to digest cellulose because they lack the enzymes necessary for its hydrolysis [5]. This fact turns the renewable cellulose into an interesting material for ethanol fermentation, known as the second generation of biofuels. The production of these biofuels is morally unproblematic as it avoids the food vs. fuel concerns. Still, the recalcitrance of cellulose – it is insoluble in water and most organic solvents [1] – causes the process to be very inefficient. In the foreseeable future mineral oil reservoirs will run dry; thus resulting in the need for alternatives and improvement in the production of the second generation of biofuels.

#### 2.1.1 Molecular structure

Cellulose is an unbranched, linear polymer consisting of  $\beta$ -D-glucopyranose molecules (= anhydroglucose units, AGU) linked by  $\beta$ -1,4-glucosidic bonds (see Fig. 1).  $\beta$  denotes the equatorial alignment of the hydroxyl (OH) group in the glucose ring (in contrast to axial alignment of the  $\alpha$  configuration), the numbers 1 and 4 indicate the sites of bonding, and D stands for the configuration of the highest numbered asymmetric carbon atom (OH group on the right, H atom on the left) [8]. Pyranose is the stable cyclic modification of D-glucose; it is a six-membered ring of five carbon atoms and one oxygen atom (in contrast to the five-membered furanose). The AGU are in the  ${}^4C_1$  conformation ( $C$  = chair), which is energetically favored; adjacent AGU are rotated  $180^\circ$ , therefore the molecules adopt a flat structure that is stabilized by intramolecular hydrogen bonds. Hydrogen bonds facilitate the formation of cellulose crystals. This crystalline structure is responsible for the high strength of cellulose.

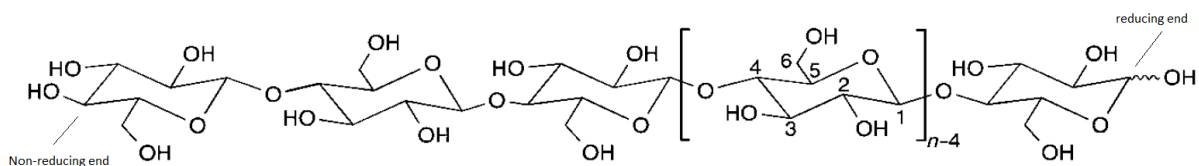


**Fig. 1: Molecular structure of cellulose showing the non-reducing and reducing ends and the numbering of the C atoms.  $n$  = degree of polymerization (DP). [7]**

The length of the cellulose chain (= number of replications of the AGU, degree of polymerization (DP)) ranges from 100 to 300 in artificial cellulose powders to 44000 for the *Valonia* algae. Generally, native celluloses have a higher degree of polymerization than regenerated celluloses.

One end of the cellulose chain is non-reducing and contains an additional hydroxyl group at C4, the other one is the reducing end with an unsubstituted hemiacetal. [1, 7]

## 2.1.2 Supramolecular structure

Nuclear magnetic resonance, infrared and diffraction studies showed that cellulose is polymorphic, i.e. it occurs in 7 different crystalline structures, namely cellulose I $\alpha$ , I $\beta$ , II, III<sub>I</sub>, III<sub>II</sub>, IV<sub>I</sub>, IV<sub>II</sub> (see Fig. 2 for the crystal structures of cellulose I and II). Most natural cellulose consists of cellulose I; the triclinic I $\alpha$  and the monoclinic, more stable I $\beta$  polymorphs coexist in this structure. Regeneration (dissolving and subsequent precipitation) or mercerization (swelling in concentrated sodium hydroxide and subsequent removing of the swelling agent) of cellulose I results in irreversible formation of cellulose II. By treating either cellulose I or II by liquid ammonia or amines followed by evaporation of ammonia/amines one gets cellulose III<sub>I</sub> or III<sub>II</sub>. Heating these polymorphs in glycerol yields cellulose IV<sub>I</sub> and IV<sub>II</sub>. Fig. 3 depicts the conversion of the polymorphs of cellulose. [1, 7, 9]

Cellulose crystallites are considered to be imperfect. This part of the cellulose structure is less ordered and commonly referred to as amorphous cellulose. [10]

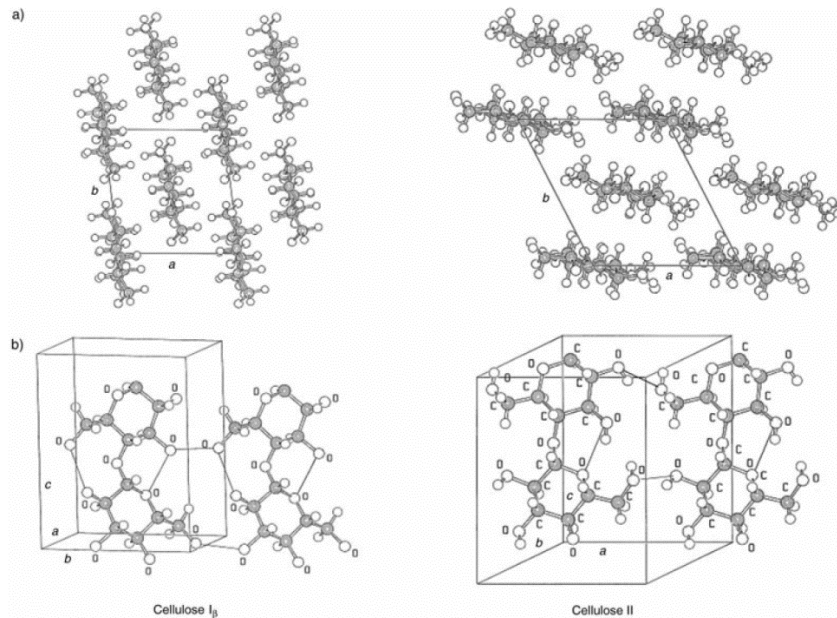


**Fig. 2:** Crystal structure of cellulose I $\beta$  (left) and cellulose II (right). a) Projection of the unit cell on the a-b plane; the parallel chains of cellulose I and the antiparallel chains of cellulose II can be seen. b) Projection of the unit cell parallel to the (100) plane of cellulose I and to the (010) plane of cellulose II. The hydrogen bonds are drawn as well. [7]

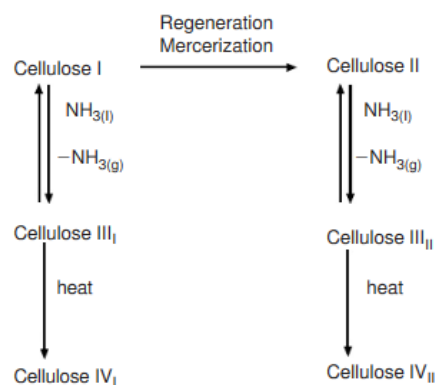


**Fig. 3:** Conversion of the polymorphs of cellulose. [9]

### 2.1.3 Morphological structure

Cellulose can be organized in several morphological structures such as microfibrils, fibres, layers, cell walls, and many more. Natural cellulose usually forms fibres. The structural organization in plants is depicted in Fig. 4. A variety of products like fibres, films etc. can be fabricated with regenerated cellulose. [1]

The basic crystalline elements of natural cellulose are microfibrils which have a width of approx. 2 nm to 50 nm and a length of up to several tens of microns [6]. In regenerated cellulose the width of the microfibrils is not dependent on the production method; it exhibits a rather constant value of approx. 5 nm [7].

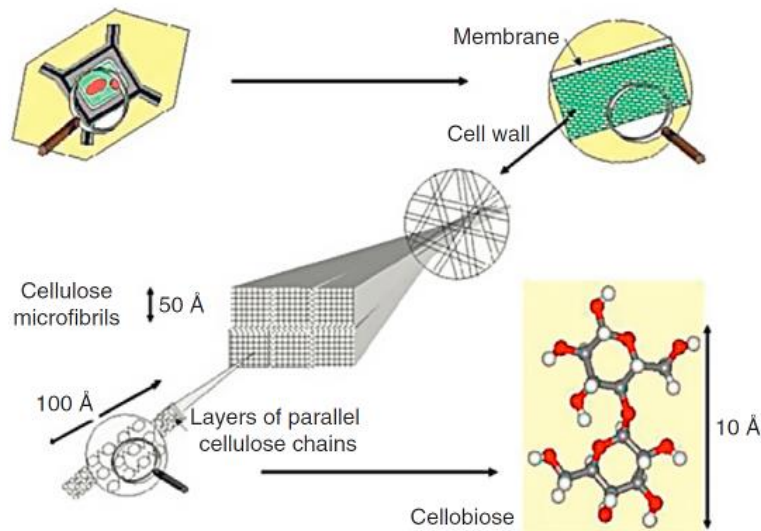


Fig. 4: Structural organization in plants. [6]

## 2.2 Cellulases

The strong  $\beta$ -1,4-glycosidic bonds make cellulose very stable. For the degradation of cellulose enzymes are needed. These so-called cellulases catalyse the hydrolysis reaction by lowering the activation energy and are not consumed by the reaction. Cellulases belong to the group of glycoside hydrolase (GH) families that hydrolyse polysaccharides in plant cell walls [1]. They are produced by microorganisms such as fungi, bacteria, certain plants, and invertebrate animals (e.g. termites and cockroaches [11]). Cellulases were discovered in World War II when the US Army noticed the quick deterioration of cellulosic material such as tents, sand bags and clothing caused by the *Trichoderma reesei* fungus. These findings triggered the intensive research on cellulose degradation. [12]

Most cellulases consist of a catalytic module and a carbohydrate-binding module (CBM or cellulose-binding domain, CBD). The catalytic module is the active part of the cellulase that hydrolyses the cellulose. The CBMs amplify the activity of the enzymes on insoluble substrates and influence the degradation of crystalline cellulose. They consist of amino acids which bind strongly to the cellulose chains through van der Waals interactions. When the CBM is connected to the crystalline substrate, the catalytic module is able to attack the cellulose chains.

Two types of cellulases exist: exo-glucanases (or cellobiohydrolases, CBH) and endo-glucanases (EG), depending on whether they split the bonds at the ends of the cellulose chains or internally, thus degrading it into cellobiose (see Fig. 5 for the structure of cellobiose).  $\beta$ -1,4-glucosidases (BGL) are able to cleave cellobiose into glucose.

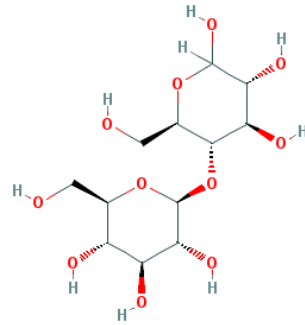


Fig. 5: Structure of cellobiose. [13]

The cellulases used in the experiments for this thesis come from the fungi *Trichoderma reesei*, which are well-studied and provide CBHs and EG. See Table 1 for the cellulases in *Trichoderma reesei*. CBH and EG produce cellobiose, which impedes the activity of both types of cellulases [14]. Therefore BGL is always added in the conducted degradation experiments to convert cellobiose into glucose. [1, 6]

Table 1: *Trichoderma reesei* cellulases. [1] The cellulases used within this thesis are marked bold.

| enzyme       | former name |
|--------------|-------------|
| <b>Cel7A</b> | <b>CBH1</b> |
| <b>Cel6A</b> | <b>CBH2</b> |
| <b>Cel7B</b> | <b>EG1</b>  |
| Cel5A        | EG2         |
| Cel12A       | EG3         |
| Cel61A       | EG4         |
| Cel45A       | EG5         |

To ensure efficient degradation of cellulose, multi-enzyme systems should be used as the cellulases show synergistic behaviour (see Fig. 6 for a scheme of the hydrolysis process and the synergism). Synergism means that the activity of the multi-enzyme system is higher than the activity of the individual enzymes. The multi-enzyme system can either be a combination of free cellulases or a multicomponent complex known as cellulosomes. [1]

Various types of synergism are known: endo-exo synergy between endo-glucanases and exo-glucanases and exo-exo synergy between exo-glucanases attacking from the non-reducing and reducing ends of cellulose chains. Moreover, there is synergy between exo-glucanases and  $\beta$ -glucosidases, where cellobiose is converted into glucose, as well as synergy between catalytic modules and CBMs. [14]

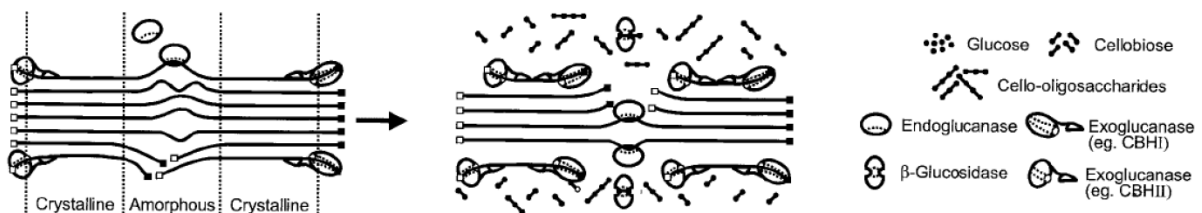


Fig. 6: Scheme of the hydrolysis of amorphous and crystalline cellulose by cellulases. Open squares represent non-reducing ends, solid squares represent reducing ends. The collaboration of the enzymes – the synergism – becomes clear. [14]

It has been reported that at least three enzymes (two CBHs + one EG) are required for effective hydrolysis of cellulose [12].

*The cellulases used in the experiments for this thesis all come from *Trichoderma reesei* and were prepared by Manuel Eibinger from the Institute of Biotechnology and Biochemical Engineering (headed by Prof. Dr. Bernd Nidetzky).*

### 2.2.1 CBH1 (Cel7A)

CBH1 (Enzyme commission number EC 3.2.1.91) is an exo-glucanase. It attacks the cellulose chain from the reducing end and degrade the cellulose into cellobiose. CBH1 has a catalytic module with a 50 Å long tunnel, where the cellulose is threaded and degraded (Fig. 7), and a CBM. Exo-glucanases are known to work on crystalline structures of cellulose. [14]

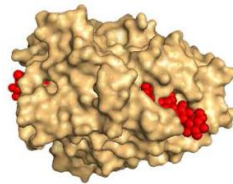


Fig. 7: Side view of the catalytic module of CBH1 processing a cellulose chain (red) in its tunnel. [3]

### 2.2.2 CBH2 (Cel6A)

CBH2 (EC 3.2.1.91) is also an exo-glucanase. In contrast to CBH1 it cleaves the cellulose from the non-reducing end. Its shape is similar to CBH2 (Fig. 8). [14]

T. Ganner found out that CBH2 works not only on crystalline regions but also shows significant activity on amorphous regions [3, 15].



Fig. 8: Front view of the catalytic module of CBH2. [3]

### 2.2.3 EG1 (Cel7B)

EG1 (EC 3.2.1.4) is an endo-glucanase. By cleaving the cellulose chain at random sites, it produces more chain ends which can be processed by exo-glucanases. Due to its shape – it has a grabber and a trench – it works best on amorphous structures of cellulose. [14]

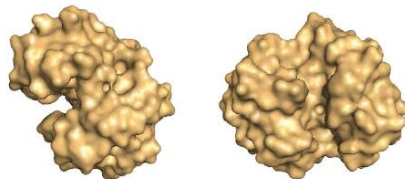


Fig. 9: Side and bottom view of EG3, representing the shape of EGs with the trench and the grabber. [3]

## 2.2.4 Supernatant (SVG)

The supernatant used in the experiments for this thesis consists of CBH1, CBH2, EG1 and BGL.

## 2.2.5 GH61 (AA9, PMO)

The family 61 glycoside hydrolase is also called AA9 (auxiliary activity 9) or PMO (polysaccharide monooxygenase). Its classification is not yet completed; at the moment it is subject to intensive research. Nevertheless, it will be referred to as GH61 throughout this thesis, since a lot of literature can still be found under this name. GH61 explains how saprophytes (organisms that live on dead or decomposing matter) attack cellulose and chitin.

By far the major limitation in the production of the second generation of biofuels is the efficiency of the enzymatic degradation of cellulose. GH61 has been repeatedly reported to accelerate the hydrolysis reaction [16, 17, 18, 19]. GH61 makes the substrate more accessible for cellulases by cleaving the cellulose chains without prior extraction from their crystalline matrix.

The GH61 protein catalyses an oxidative mechanism (in contrast to the hydrolytic mechanism of cellulases) in presence of an external electron donor and a divalent metal (copper). Cellobiose dehydrogenase (CDH) or e.g. ascorbate can donate an electron to the active site in GH61 where oxygen is partially reduced and the pyranose rings of cellulose are attacked. The glucosidic bonds become instable and eventually break. See Fig. 10 for the schematic representation of the process.

The active site of GH61 is a flat face of approx.  $40 \text{ \AA} \times 30 \text{ \AA}$  [16], differing from the known cellulases with grooves and tunnels. [16, 17, 18, 19]

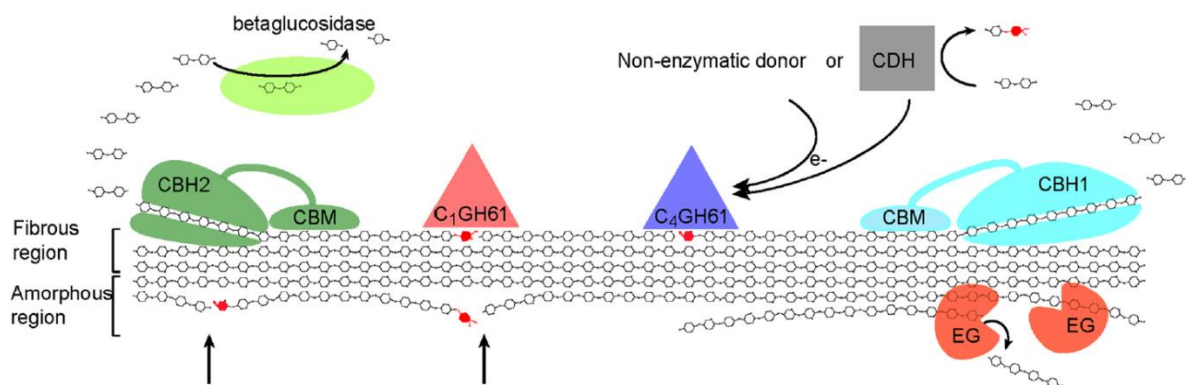


**Fig. 10:** Current view on enzymatic degradation of cellulose. C1 and C4 oxidizing GH61 enzymes are shown which generate optimal (non-oxidized) ends for CBH1 and CBH2 (oxidized sugars in red). Thus, new chain ends for the CBHs are created (indicated by the arrows on the bottom). [17]

## 3 Experimental techniques

### 3.1 Atomic Force Microscopy

The atomic force microscope (AFM) is a scanning probe microscope (SPM) that mechanically scans the sample. It provides images by “feeling” the sample’s surface. This makes the AFM an essential non-destructive instrument for the characterization of surfaces down to the scale of nanometres. It allows access to 3D topological representations, manipulation of surfaces and gives information about mechanical, chemical, electrical and magnetic properties.

The invention of the scanning tunnelling microscope (STM) in 1982 by G. Binnig, H. Rohrer and E. Weibel [20] led the way to the development of the AFM in 1986 by G. Binnig, C. F. Quate and C. Gerber [21]. The STM detects the current that flows between the sample and the metallic tip located closely above if an external voltage is applied. For this purpose, however, the sample has to be conductive, which is the big disadvantage of the STM. The basic principle of the STM resembles the one of the AFM, yet the AFM is not limited by the conductive characteristics of the sample.

Since then a lot of progress has been made, various operation modes have been introduced, starting from contact mode to amplitude modulation AFM, multi-frequency AFM, and high-speed AFM. Even measurements in liquid to observe dynamic biological processes in-situ are possible. These findings supply the experimental basis of this thesis. [22]

#### 3.1.1. Principle

The centrepiece of the AFM is the sharp tip that is mounted on a flexible cantilever. The tip interacts with the sample when it is moved closely along the surface together with the cantilever. The forces on the tip are kept constant, causing the cantilever to bend when the topology of the surface changes. The deflection of the cantilever is recorded and processed to obtain an image of the sample’s surface. See Fig. 11 for the main components of an AFM.

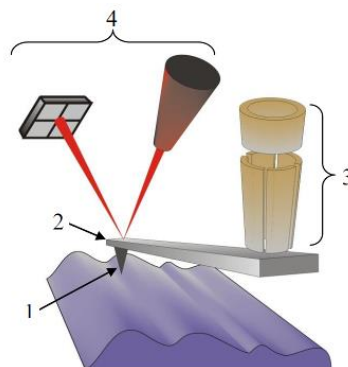


Fig. 11: The main components of the AFM. 1: tip. 2: cantilever. 3: motion system. 4: detection system. [23]

#### 3.1.2. Components

The main components of an AFM are explained in more detail: the cantilever-tip system, the motion system, the detection system, the feedback system, and the image processing unit.

### Cantilever-tip system

The micro-electronically manufactured cantilever-tip system is an essential part of the AFM. Materials used in production are silicon or silicon nitride. The sharp tip is mounted on the end of the cantilever which is attached to a glass plate for better handling. As the tip directly approaches the sample, its geometry (radius and apex) strongly influences the quality of the image. The sharper the tip, the better the resolution of the image; on the other hand those tips are more prone to picking up dirt or being damaged (see Fig. 12). Commonly used tips have a radius of approx. 5 nm to 10 nm; however, tips with a radius down to 2 nm are available.

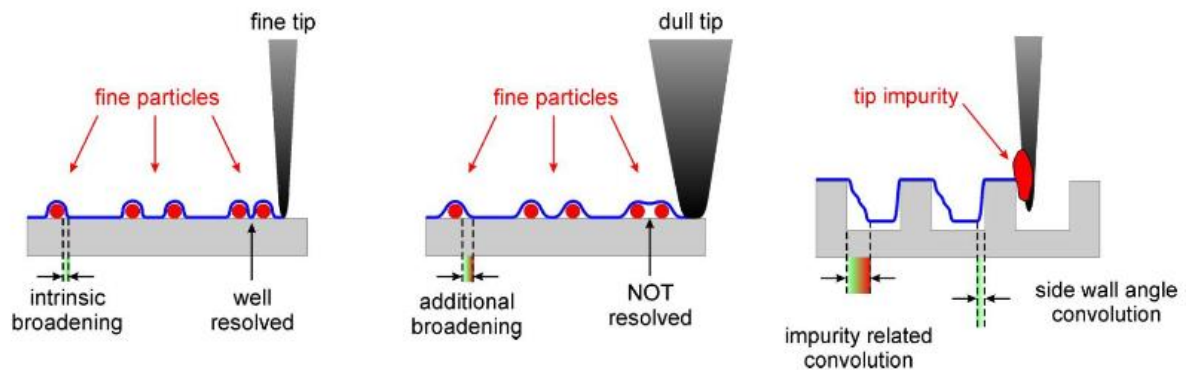


**Fig. 12: Influences on the image quality.** Higher resolution can be achieved with a fine tip (left); a dull tip (middle) is not able to resolve fine features. Particles that stick to the tip can distort the true structure of the sample (right). [23]

Generally, cantilevers feature two geometries, v-shaped or rectangular (see Fig. 13). V-shaped cantilevers have a smaller spring constant than rectangular ones; thus v-shaped cantilevers are softer. Each AFM operation mode uses its most suitable cantilever.

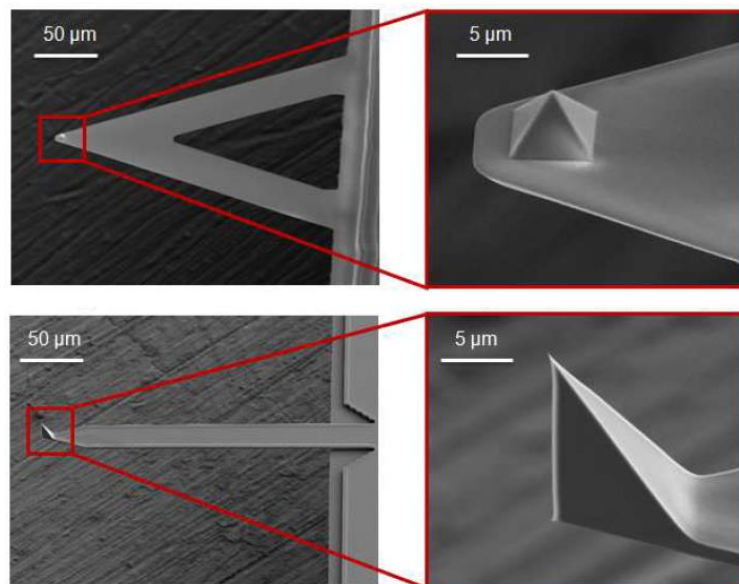


**Fig. 13: SEM images of v-shaped (top) and rectangular (bottom) cantilevers.** The right column shows a pyramidal (top) and a tetragonal (bottom) tip. [23]

### Motion system

Piezoelectric actuators guarantee the accurate and fine movements that are required to detect the deflection of the cantilever. The usual design of the motion system is a tube scanner, where the upper ring

is responsible for the vertical z-movement and 2 opposite segments of the 4-segmented lower ring control the x- and y-movements, respectively (see Fig. 14 and Fig. 15).

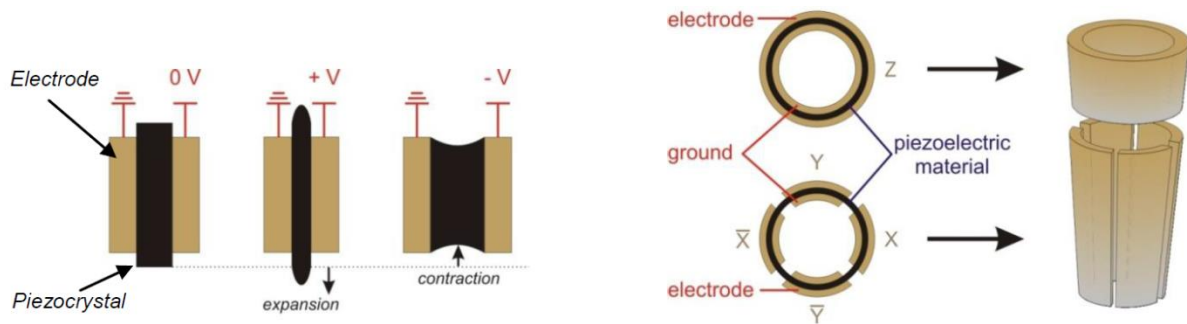


**Fig. 14:** Left: By applying a positive or negative voltage a piezocrystal either expands or contracts. This behaviour is used in the tube scanner of the motion system of an AFM (right). [23]

This set-up can capture a large range of scanning areas (from  $\text{nm}^2$  to  $\mu\text{m}^2$ ); on the other hand there is coupling between the lateral and vertical movements and the piezoelectric behaviour does not depend linearly on the voltage, thus inducing hysteresis, creeping and other effects. Most aberrations can be corrected by the software; still, regular recalibration is essential to achieve best results in AFM measurements. [22]

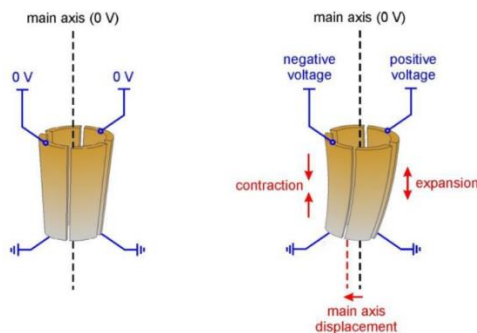


**Fig. 15:** The piezoelectric elements are moved by applying reverse voltage to the associated segments. [23]

### Detection and feedback system

There are various ways of detecting the deflection of the cantilever. The most commonly used method is the optical beam deflection method because it is a simple and highly sensitive technique. A laser beam is reflected from the back of the cantilever onto a 4 segmented position sensitive photodetector (PSD). When the cantilever is bent, the laser beam hits the PSD at a different position (see Fig. 16). The 4 segments allow the detection of lateral and normal forces. Lateral deflections characterise the friction force in contact mode. To ensure high sensitivity down to deflections of 0.01 nm or lower, the laser beam has to be well-adjusted. On the one hand it has to hit the cantilever at its outmost point, on the other hand the laser beam has to be centred along the cantilever to maximize the intensity of the signal at the PSD. This sophisticated alignment can be avoided by using self-sensing methods, such as piezoresistive cantilevers. A piezoresistive layer on the cantilever changes its resistance when the cantilever is deflected. This is due to geometrical reasons and influences that originate from the shift of the electrons in the band structure caused by the stress [24].

The information about the deflection of the cantilever is fed into the feedback system, which keeps the deflection constant by controlling the motion system. This interference of the feedback system at each x-y-position is recorded and processed into an image. [22]

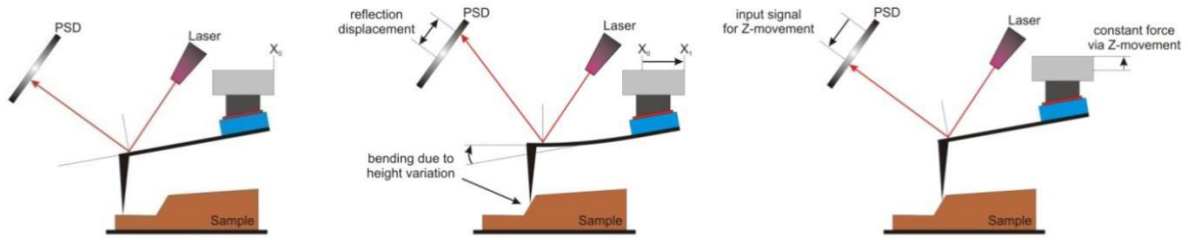


Fig. 16: Optical detection system and image acquisition of an AFM. Left: the cantilever's initial position/bending. Middle: The cantilever is deflected due to change in height, the laser beam hits a different position on the PSD. Right: the feedback system controls the motion system so that the cantilever gets back to its initial position/bending. The deflection signal is processed to obtain an AFM image. [23]

### 3.1.3. Effective forces in AFM

AFM is based on the interactions between the tip and the sample; a variety of forces affect the tip when it approaches the sample's surface (see Table 2).

Table 2: Effective forces between tip and sample

| Tip-sample distance $r$ | Effective forces                              | Dependence on potential<br>( $a, b, c \dots$ constants) |
|-------------------------|---|---|
| $> 10$ nm               | Electrostatic (magnetic)                      | $\frac{c}{r^2}$   |
| 10 to 5 nm              | Van der Waals<br>(dipole-dipole interactions) | $-\frac{a}{r^6}$  |
| $< 0.2$ nm              | $e^- - e^-$ repulsion<br>(Pauli principle)    | $\frac{b}{r^{12}}$                                      |

The distance between tip and sample is usually less than 10 nm, thus electrostatic and magnetic forces can be neglected. The influences of the remaining effective forces can be described by the Lennard-Jones potential  $V_{LJ}$ :

$$V_{LJ} = V_{ee} + V_{vdW} = \frac{b}{r^{12}} - \frac{a}{r^6} \quad (1)$$

The electron-electron interactions  $V_{ee}$  are repulsive, the Van der Waals contributions  $V_{vdW}$  are attractive. The distance between the tip and the sample is denoted as  $r$ ,  $a$  and  $b$  are constants.

This means that the tip is initially attracted when it moves towards the sample (attractive regime). As soon as it gets close enough so that the orbitals of the electrons in the sample and the tip overlay, the Pauli principle prohibits further approach and the tip is repelled (repulsive regime). This behaviour is illustrated in Fig. 17.

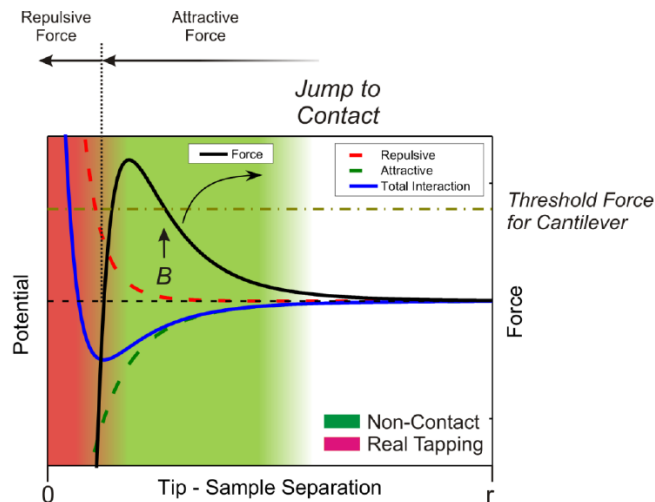


Fig. 17: Effective forces between tip and sample during the approach. The overall Lenard-Jones potential is depicted in blue, the repulsive electron-electron and the attractive Van der Waals interactions are drawn in red and green. [23]

When performing AFM measurements under ambient conditions capillary forces are an important factor. Water from vapour in the air condenses on the sample and can form a meniscus around the tip, which severely affects the image quality. The water films covering the sample's surface and their limiting effects have been reported by G. Binnig et al. in 1986 when introducing the AFM [21]. These disturbances vanish in liquid environments. [22]

### 3.1.4. Operation modes

The operation modes relevant for the work in this thesis are explained here.

#### Contact mode

In this mode the tip is constantly in contact with the sample. If the tip meets a higher feature on the sample while scanning, the cantilever is bent and the point where the laser hits the PSD is changed. Subsequently, the feedback loop controls the piezoelectric elements and adjusts the z-position of the cantilever to restore constant deflection of the cantilever and thus constant force on the sample. The samples are required to be rather mechanically stable when operating the AFM in contact mode, because the samples can easily be damaged by the moving tip.

#### Tapping and phase mode

These modes allow investigations of sensitive materials, as the tip does not touch the surface permanently; the cantilever is oscillating and only tapping the sample's surface during the measurement. The resonance frequency of the free system (in the range of 50 kHz to 400 kHz) is determined before approaching the surface and a fixed amplitude value of the oscillation is chosen.

When the tip moves towards the surface and scans it, the interaction with the sample causes damping of the amplitude (see Fig. 18). Since the amplitude value is kept constant by the feedback system to guarantee constant force on the sample, the z-coordinate of the cantilever has to be altered according to the surface features of the sample and is processed for image acquisition.

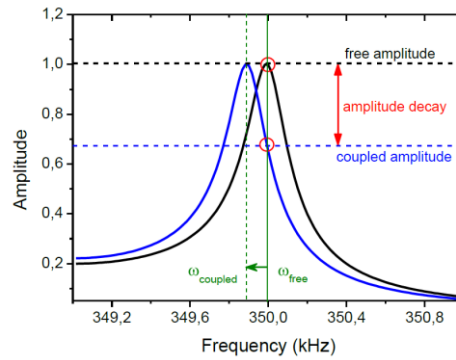


**Fig. 18: Damping of the amplitude and shifting of the resonance frequency when the tip couples with the sample in tapping mode. [23]**

In tapping mode the AFM can be either operated in attractive or repulsive working regime. The attractive regime, where just the Van der Waals forces are effective, corresponds to a non-contact mode, the tip never touches the surface. This is considered an ideal mode for very sensitive materials, although imaging can be severely complicated by the water meniscus forming around the tip. This can be avoided in the repulsive regime where the tip repeatedly hits the sample and the electron-electron repulsion is dominant.

Additionally, the tapping mode allows a more sophisticated operation method, the phase mode. Information retrieved from the phase lag between the excitation oscillation and the actual oscillation of the cantilever provides an additional image (see Fig. 19). This phase image is simultaneously recorded with the height image and represents variations in the composition or distribution of the material, for instance crystalline and amorphous structures of the sample, and can also emphasize distinct topographical features. [22]

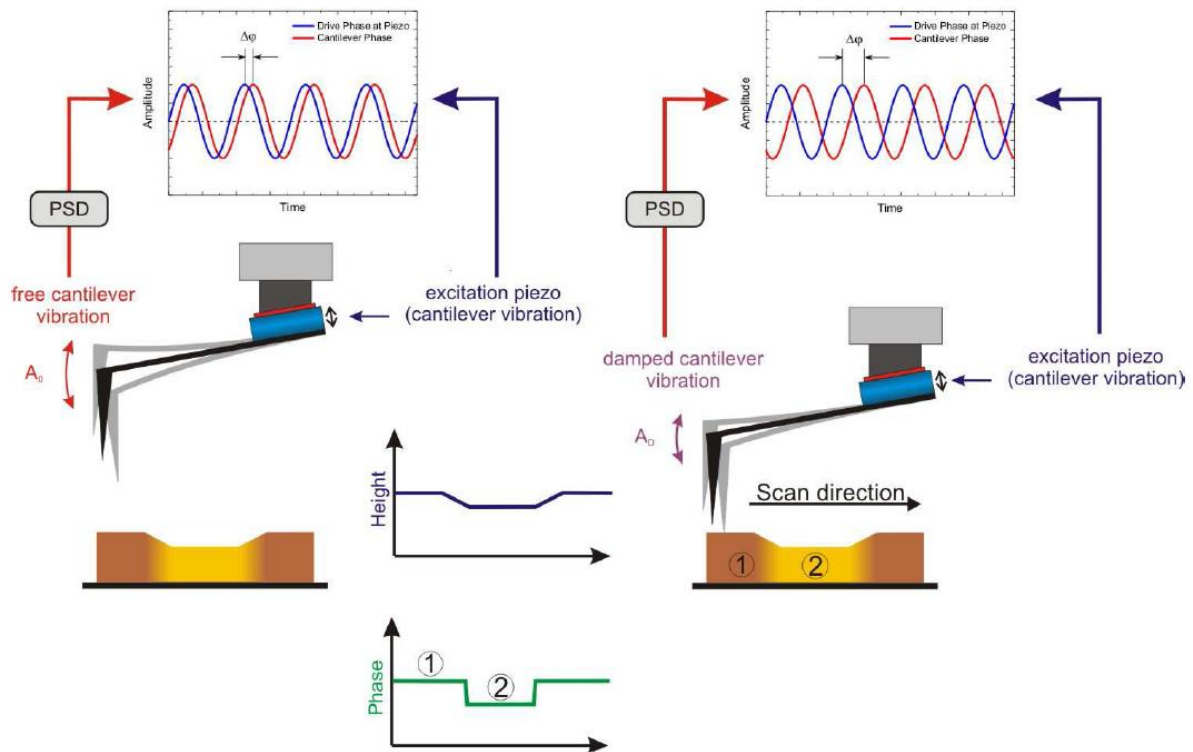


**Fig. 19: AFM phase mode. The phase lag of the free cantilever (left) is different from the phase lag of the cantilever that is coupled with the sample (right). The phase image provides information about the material's composition and topological features. [23]**

### Tapping mode in liquid AFM

Operating the AFM in liquid is a challenging yet very powerful application allowing for instance in-situ visualisation of biological processes. Liquid AFM requires a special set-up, containing a suitable tip holder, cantilever and a liquid cell (see Fig. 20). When the cantilever immerses into the liquid (water/buffer solution), capillary forces are avoided but electric double layer forces appear and the cantilever's behaviour changes. The alterations can be observed in the resonance curve (see Fig. 21). The resonance peak is shifted to lower frequencies by a factor of approx. 3 to 5 and is broadened, because the liquid damps the cantilever's oscillation more as compared to operation in air. Most of the resonances in the resonance curve do not represent eigenmodes of the cantilever but resonances of the surroundings (liquid and liquid cell). Moreover the cantilever's deflection is not symmetric anymore, thus it cannot be approximated by a sinusoidal wave and higher eigenmodes of the excitation frequency cannot be neglected any longer. [22]

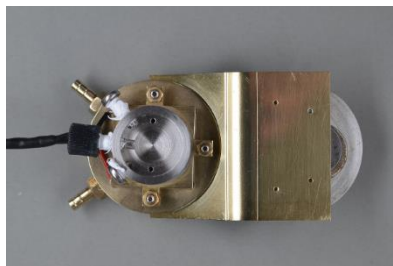


Fig. 20: Liquid cell (in-house construction by T. Ganner [3]).

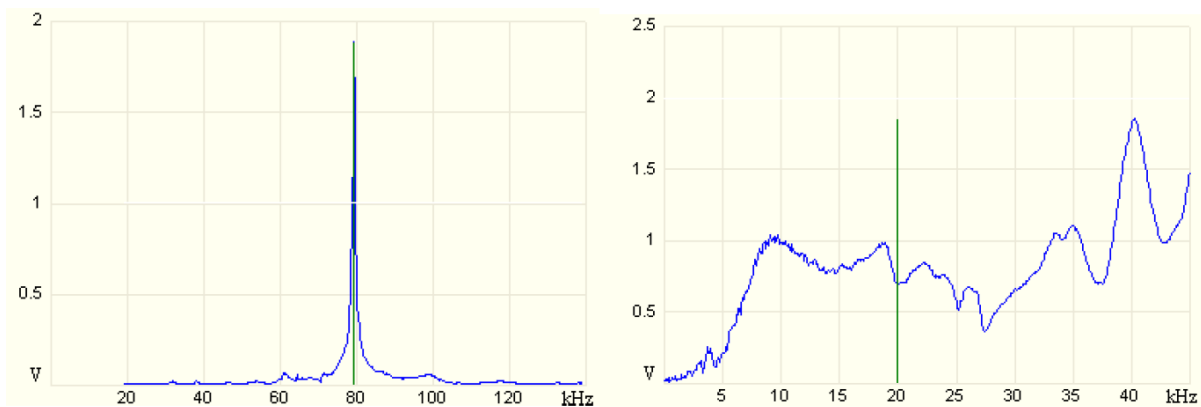


Fig. 21: Resonance curves of a cantilever in air (left) and in liquid (right). [4]

AFM was conducted on a commercial Dimension 3100 AFM equipped with a Hybrid X-Y-Z closed loop scan head and a Nanoscope IVa controller (Bruker AXS, Santa Barbara, USA) at the Institute for Electron Microscopy and Nanoanalysis.

## 3.2 X-ray diffractometry

X-ray diffractometry (XRD) reveals the atomic structure of the material investigated. Incoming X-rays are diffracted by the atoms and interfere constructively only, when Bragg's law:

$$2d \sin \theta = \lambda, \quad (2)$$

where  $d$  is the spacing between the atomic planes,  $\theta$  the angle of the incident beam, and  $\lambda$  the wavelength of the radiation, is fulfilled. The peaks in the resulting spectra are characteristic for each material and allow access to a multitude of parameters of the crystalline structure. [25]

For this thesis the distinction between the polymorphic cellulose structures is vital, especially between cellulose I and cellulose II. Fig. 22 shows the spectra of cellulose I and cellulose II. The sharp main peak of cellulose I occurs at  $2\theta = 22.7^\circ$  (representing the 002 reflex). The side lobes come from the 101 and  $10\bar{1}$  reflexes and are located around  $2\theta = 15^\circ$ . In the cellulose II spectrum the  $10\bar{1}$  is shifted to  $20^\circ$ , the 101 reflex to  $12^\circ$ . [26]

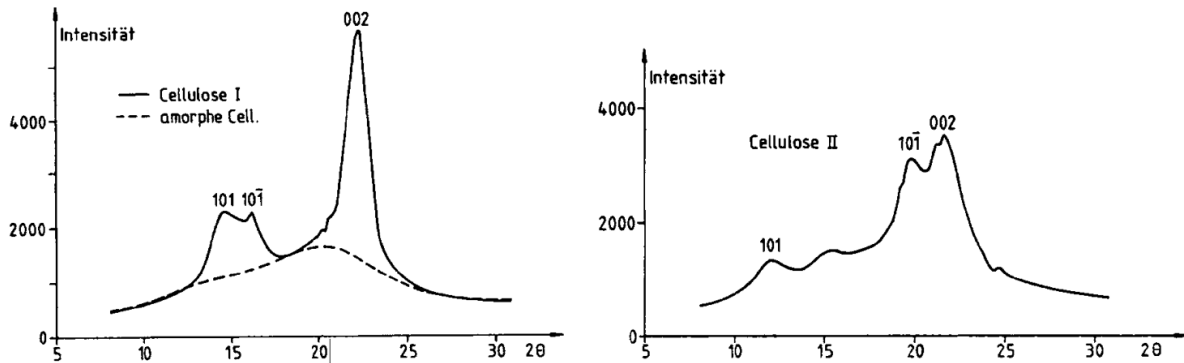


Fig. 22: XRD spectra of cellulose I (left, including amorphous cellulose) and cellulose II (right). [26]

*X-Ray Analysis was conducted on a Siemens D 5005 X-Ray diffractometer (CuK $\alpha$  1 radiation; Siemens, Munich, Germany) by Thomas Ganner at the Institute for Electron Microscopy and Nanoanalysis.*

### 3.3 Raman spectroscopy

In Raman spectroscopy monochromatic light excites electrons in the investigated material into a virtual state. Raman scattering can be observed when the electrons relax from these virtual states into states differing from their initial states; the emitted radiation can either come from Stokes (electrons relaxing into higher energy states) or Anti-Stokes (relaxing into states with lower energy) scattering. The resulting intensity spectra depict the shifts in the wavelength of the incoming light and give detailed information about the energy levels of the investigated material; thus, Raman spectroscopy can be used to characterize the material, its binding properties, molecular structure and much more. [27]

Conducting Raman spectroscopy on cellulose samples offers the possibility to investigate the crystalline structure of cellulose and its degree of crystallinity [28, 29]. These measurements can substantiate results derived from XRD and vice versa.

*Raman spectroscopy was performed on a LabRAM HR Raman (Horiba Ltd., Tokyo, Japan) by Boril Chernev at the Institute for Electron Microscopy and Nanoanalysis.*

### 3.4 Transmission electron microscopy

The resolution power of a light microscope (LIM) is limited by the wavelength of the visible light. Thus it is a logical step to use radiation with a smaller wavelength to increase the resolution power. The wavelength of electrons with an energy of 100 keV is about  $10^5$  times smaller than the wavelength of visible light.

The main components of a transmission electron microscope (TEM) are similar to those of a LIM. Electrons are emitted from a source (thermal or field emission) and electromagnetic lenses focus the electron beam on the sample where the electrons interact with the sample. In TEM one is interested in the transmitted electrons which can form the real image of the sample or the diffraction pattern induced by the electrons. Generally, inelastically scattered electrons are used for material analysis and electrons from elastic interactions give structural information. [30] In combination with spectroscopic instruments for electron energy loss spectroscopy (EELS) and energy dispersive X-ray (EDX) spectroscopy the TEM is a powerful, high-resolution analytical instrument. However, interpretation of the results obtained and sample preparation for TEM are highly sophisticated processes requiring a lot of experience of the operator. Moreover, the samples have to withstand the exposure to the electron beam which can particularly damage biological materials.

*TEM investigations were performed on a Tecnai F20 (FEI, Hillsboro, Oregon, USA) by Johanna Kraxner at the Institute for Electron Microscopy and Nanoanalysis.*

## 3.5 Scanning electron microscopy & EDX

In scanning electron microscopy (SEM) the sample is scanned by an electron beam point by point. The area hit by the beam emits secondary electrons that reach a detector above the sample. The electrical signal induced in the detector is amplified and displayed. SEM is suitable for massive samples in particular, offering analysis of 3D structures in high resolution with great sharpness. [30] For the examination in SEM the sample has to be electrically conductive and has to withstand high vacuum, as the SEM can only be operated in vacuum; that can be seen as a drawback of this method.

The incident electrons are able to knock out electrons from inner shells of the sample. The holes are then filled by electrons from higher energy levels and the excessive energy is emitted as a characteristic X-ray. Detecting those X-rays with a suitable detector makes it possible to analyse the material composition of the sample. Modern SEM often features such an energy dispersive x-ray (EDX) spectroscopy set-up.

*Scanning electron microscopy was performed on a Gemini DSM 982 (LEO, Oberkochen, Germany) and a Quanta 200 Environmental-SEM (FEI, Hillsboro, Oregon, USA), EDX analysis was performed on the Quanta 200 by Thomas Ganner at the Institute for Electron Microscopy and Nanoanalysis.*

## 4 Sample preparation

The requirements for the cellulose samples used to observe the enzymatic degradation are predominantly defined by AFM. Due to the limit in height adjustment of the AFM (around 7  $\mu\text{m}$  for the AFM used in the investigations in this thesis) the samples have to be very flat. That leads to a positive side effect, since alterations on flat samples can be observed more easily than on rough surfaces. Apart from being flat the samples have to be reproducible with respect to their topological and morphological features and their resemblance to nature (i.e. consisting of amorphous and crystalline structures).

The samples that have been used so far by J. Dohr [2], T. Ganner [3] and T. Aschl [4] fulfil the requirements and have turned out to be suitable in numerous experiments. However, the production of the so-called FSEC (fractional solvent exchange cellulose) samples is a tedious process, leaving no possibilities for quick testing substrates with well-defined properties. In this thesis this is tried to be changed by introducing spin cast cellulose (SCC) samples, which can be prepared fast and lead to well-tuned samples that may be used for measurements focusing on the quantitative effect of enzymatic degradation. The amorphous features in the SCC samples are represented by trimethylsilyl cellulose (TMSC) and the crystalline structures by nano-crystalline cellulose (NCC), which have the same width as natural cellulose crystals but are much shorter [1]. Also the FSEC samples are developed in this respect so that they can serve as reliable and well-tested substrates in quantitative measurements as well.

This chapter briefly describes the preparation methods of the various types of samples.

### 4.1 Ultramicrotomy

Ultramicrotomy is a sample preparation method widely used in electron microscopy to obtain ultra-thin slices (down to 10 nm) and ultra-flat cuts (important for AFM investigations). For this purpose the sample is bedded in epoxy. The main components of the instrument are a feed mechanism, a sample holder and a knife holder. Depending on the type of the ultramicrotome the sample is either moved towards the knife or the knife is moved towards the sample in pre-set steps controlled by the feed mechanism. With each step an ultra-thin slice is removed from the sample leaving behind an ultra-thin surface cut. For this high-precision process it is vital that vibrations are avoided. The cutting is observed by a microscope. Glass or diamond knives are used in ultramicrotomy, which can be fixed in a trench to allow cuts in liquid. [31]

*The ultramicrotome (Leica EM UCS-NT, Wetzlar, Germany) used for sample preparation in this work can be seen in Fig. 23. The cuts were performed by Claudia Mayrhofer and Thomas Ganner at the Institute for Electron Microscopy and Nanoanalysis.*



**Fig. 23:** Leica ultramicrotome. [32]

## 4.2 FSEC

The preparation of the fractional solvent exchange cellulose (FSEC) samples is based on intensive studies conducted by J. Dohr [2], T. Ganner [3] and T. Aschl [4].

Microcrystalline Avicel PH101 (Avicel) is dissolved with an ionic liquid (1-N-butyl-3-methylimidazolium chloride BMIMCl). Ionic liquids are molten salts and one of the few environmental friendly solvents capable of solving cellulose. The high chloride concentration and activity in BMIMCl is responsible for breaking the hydrogen bonds in cellulose [33, 34]. Various cellulose concentrations up to 15 wt. % have been tried and profoundly studied by T. Aschl [4]. During the mixing procedure the solution is heated up to 100 °C for 24 hours. The resulting viscous and clear gel is dried between glass plates separated by glass spacers to guarantee homogenous thickness of the dried samples (see Fig. 24). This process takes one week. To remove the ionic liquid still present in the dried samples, a fractional solvent exchange is performed by exposing the samples to increasing concentrations of ethanol in multiple steps. The samples are cut into small flakes (see Fig. 24) and embedded in epoxy. Now the samples are ready for cutting by ultramicrotomy (see Fig. 25) to get flat surfaces for AFM investigations.



**Fig. 24:** Drying of the gel between glass slides (left) and resulting stiff flakes after the fractional solvent exchange (right). [3]

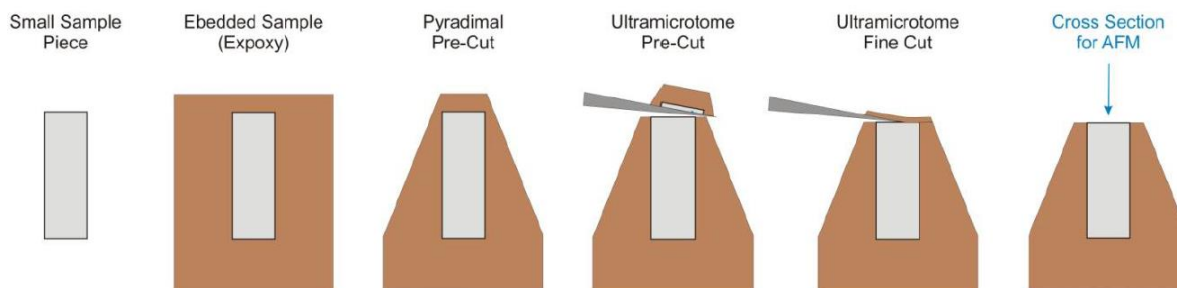


**Fig. 25:** Depiction of the cutting process of an embedded FSEC sample by ultramicrotomy. [2]

The procedure explained provides so-called FSEC1 samples. However, the preparation method has been adapted in several ways. One of these adaptations leads to samples denoted as FSEC2 samples in this thesis. In the FSEC2 samples, Avicel flakes are added after the mixing process to better control the sample properties by incorporated well-defined crystalline features. These Avicel residues are used as surface markers for quantitative analysis of the enzymatic degradation process. The tests conducted with the FSEC2 samples are summarized in chapter 6. Further developments lead to the introduction of FSEC3 samples with an optimized mixing process. Several properties of these three sample types are compared in chapter 6.1. Degradation experiments are conducted with FSEC1 and FSEC2 samples in this thesis.

*The FSEC1 and FSEC2 samples used for the investigations in this thesis were prepared by Thomas Ganner; the cuts by ultramicrotomy were conducted by Claudia Mayrhofer and Thomas Ganner.*

## 4.3 Spin casting

Spin casting is a convenient method to obtain very flat and homogenous single- or multi-layered samples. The sample solution is coated onto a suitable substrate carrier. During the rapid rotation the solvent evaporates and the material is distributed by centrifugal forces. The process provides highly reproducible samples. In cellulose partial alignment of the fibres due to the effective shear forces can be observed. [35]

The spin casting process is adopted to introduce a new type of cellulose substrate, the spin cast cellulose (SCC). This is a combination of amorphous TMSC and nano-crystalline (NCC) features.

## 4.4 Spin cast cellulose – TMSC

The preparation of the trimethylsilyl cellulose samples is based on the procedure explained by Kontturi et al. [36]. The trimethylsilyl cellulose from Avicel is dissolved in Xylol and sonicated for several minutes, until the cellulose is completely dissolved, resulting in a clear, slightly viscous liquid (concentrations: 5 g of TMSC per liter solvent, 10 g/l and 15 g/l). This solution is spin coated with spinning rates of either 4300, 5300 or 6300 rpm on the substrate carrier, a 1 cm × 1 cm silicon wafer. The conversion of TMSC to cellulose is done by acid hydrolysis (4 min exposure of the sample in a vessel containing 10 % HCl under light vacuum conditions). The sample is then ready for investigation (see Fig. 26). This reveals the big advantage of the spin cast samples; these samples are prepared very quickly within approx. 2 hours!

Multiple layers can be spin casted on the Si wafer providing thicker films for XRD or long-time AFM measurements.

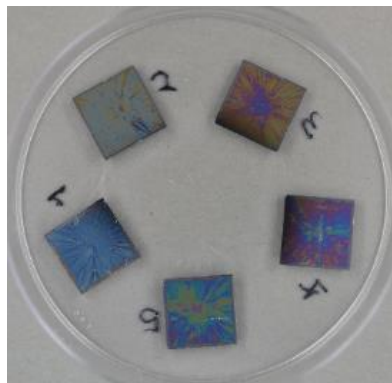


Fig. 26: TMSC samples with 1 to 5 layers spin coated on the Si wafer. [32]

## 4.5 Spin cast cellulose – NCC

The preparation of the nano-crystalline suspension is based on the strategy by Edgar et al. [37]. The filter paper approach is chosen, where cotton fibres from Whatman No. 1 filter paper serve as source of cellulose. 40 g of filter paper are grounded in a mill (so fine that they pass a 1 mm mesh). This is followed by hydrolysis of the cellulose in 700 ml of 64 wt. % sulphuric acid at 45 °C for 45 min. The solution is then 10-fold diluted to stop the reaction immediately. Further dilution by distilled water and several cycles of centrifuging brings the pH value to a value greater than 1. The solution is filtered. Pre-filtering is performed with a “Blauband Nr. 598<sup>3</sup>” filter, which has a size of 2 µm to 3 µm, followed by filtering with a syringe top (Miniart 16555, 0.45 µm membrane). After pre-filtering the solution is still

milky, the 0.45  $\mu\text{m}$  filtering leads to a crystal clear solution. The filtering process is accomplished with a membrane  $< 0.2 \mu\text{m}$ . The solution is concentrated by heating resulting in a very viscous gel. Further treatment for enzymatic degradation experiments with NCC and TMSC/NCC samples is described in the chapters 6.3.2.4 and 6.3.3.1.

## 5 Strategy overview

The enzymatic degradation experiments conducted in this thesis promote the development of the artificial cellulose substrate. A graphical overview of the substrate development in this thesis is illustrated in Fig. 27. Starting from the need for better control over the embedding of crystalline features in the well-studied FSEC1 samples, FSEC2 samples are introduced and their properties are characterized by light microscopy, X-ray diffraction, Raman spectroscopy, and atomic force microscopy. In the experimental series to study the influence of GH61 on the cellulases (CBH1, CBH2, EG1, and the supernatant SVG) the FSEC2 samples turn out to be inappropriate for quantitative measurements which are required to detect the assumed activity increase caused by GH61. Hence, a new substrate suitable for such investigations had to be found. On the one hand improved FSEC3 samples are developed. On the other hand the spin casting preparation process offers highly reproducible [38] and quickly prepared samples with control over the properties of the artificial samples. The amorphous and crystalline features are represented separately by TMSC and NCC. These types of samples are intensively characterized and tested and finally lead to the introduction of a new, very promising type of substrate, the combined TMSC/NCC samples.

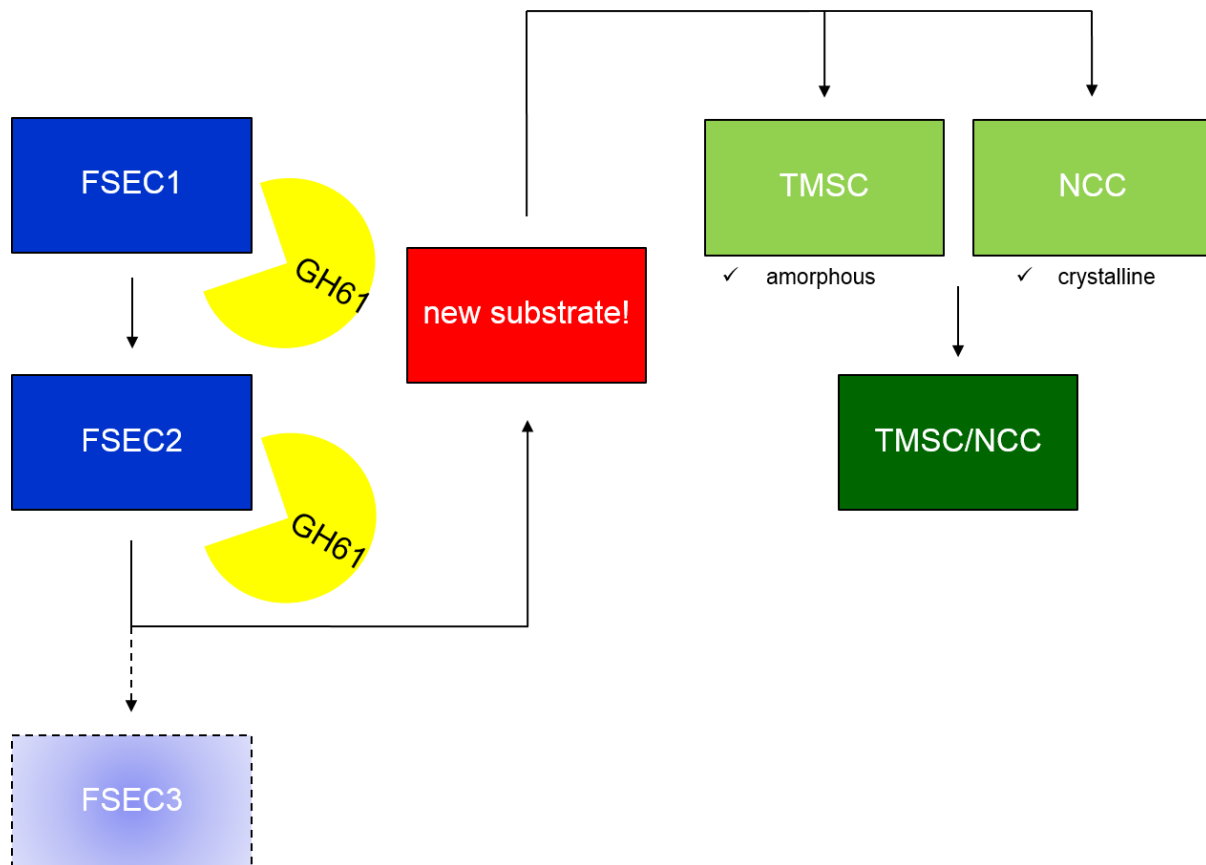


Fig. 27: Graphical overview of the substrate development in this thesis.

## 6 Experiments

This thesis focuses on the improvements of the artificial cellulose substrates used for enzymatic degradation experiments and on studying the influences of the enzyme GH61 on the effects of the cellulases CBH1, CBH2, EG1, and its supernatant SVG. Most of the experimental work consists of atomic force microscopy (AFM) investigations of enzymatic degradation; the experiments discussed in this thesis are listed in Table 3. The properties of the developed samples are examined by light microscopy (LIM), X-ray diffraction (XRD), Raman spectroscopy, scanning electron microscopy (SEM), energy dispersive X-ray spectroscopy (EDX), transmission electron microscopy (TEM), and atomic force microscopy (AFM).

Newly introduced cellulose samples should offer the possibility to adjust the properties of the samples (especially content and size of the crystalline features) and enable quantitative measurements of the degradation process via enzymes; this is tested in the GH61 experiments with the FSEC2 samples as well as with the SCC samples.

**Table 3: Overview of AFM enzymatic degradation experiments**

| sample   | enzyme    | amount/ $\mu$ l | comments   |
|----------|-----------|-----------------|--|
| FSEC1    | SVG       | 70              | degradation: $0.8 \pm 0.3$ nm/min                    |
| FSEC1    | GH61/SVG  | 10/70           | degradation: $1.4 \pm 0.2$ nm/min                    |
| FSEC2    | EG1       | 200             | degradation: $0.4 \pm 0.2$ nm/min                    |
| FSEC1    | GH61/EG1  | 10/150          | degradation: $0.5 \pm 0.1$ nm/min                    |
| FSEC2    | CBH2      | 272             | degradation: $0.6 \pm 0.2$ nm/min                    |
| FSEC2    | GH61/CBH2 | 10/136          | degradation: $1.3 \pm 0.2$ nm/min                    |
| FSEC2    | CBH1      | 250             | degradation $\geq 0.6$ nm/min                        |
| FSEC2    | GH61/CBH1 | 8/250           | GH61 activity, tip influence, minor degradation      |
| TMSC     | SVG       | 100             | degradation observable                               |
| TMSC     | CBH2      | 62.5            | degradation observable                               |
| NCC      | SVG       | 250             | slight effects on (single!) crystallites             |
| NCC      | CBH1      | 250             | minor degradation observable ( $\approx 0.1$ nm/min) |
| TMSC/NCC | SVG       | 250             | degradation velocities depend on structure           |
| TMSC/NCC | CBH2/CBH1 | 300/400         | synergism observable                                 |

### AFM experimental procedure in liquid environments

The majority of experiments conducted in this thesis are AFM investigations of enzymatic degradation in liquid environments. The execution of the experiments is based on the knowledge from intensive previous AFM studies in liquid environments by J. Dohr [2], T. Ganner [3] and T. Aschl [4]. A detailed description of liquid AFM can be found in T. Ganner's master thesis [3]. Here the experimental procedure of these experiments is just briefly explained. Alterations of this procedure are mentioned in the corresponding sections.

For experiments on fractional-solvent-exchange-cellulose (FSEC) substrates, the samples stay immersed in buffer solution (sodium phosphate buffer,  $\text{NaH}_2\text{PO}_4$ ) after ultramicrotomy cut until investigation. The samples are placed in the AFM liquid cell which is filled up by the buffer solution immediately to prevent drying of the substrate. The tips used were Olympus OMCL-RC800PSA as they turned out to provide highest stability and sensitivity during operation in liquids [3]. The tips are mounted in a special holder suitable for investigations in liquid. After a first quick adjustment of the AFM in dry environments the cantilever is dipped into the liquid cell and the adjustment is repeated in

liquid. First AFM overview images (10  $\mu\text{m}$  to 40  $\mu\text{m}$  scan range) are recorded to find suitable Avicel residues which serve as a reference marker for the degradation analysis as they are degraded very slowly by the enzymes [3]. All experiments are conducted at room temperature (20  $^{\circ}\text{C}$ ). The enzymes are added directly into the liquid cell by micropipettes and the sample is exposed to the enzymes for at least 4 hours. During exposure consecutive AFM images are recorded with different scan sizes to provide both overview and detail information.

Short note on the amount of enzymes used in the degradation experiments: 250  $\mu\text{l}$  of enzymes (corresponding to 50  $\mu\text{g}$  enzymes per mg substrate) is already a large amount to add to the liquid cell (see Table 3 for the amounts applied). To guarantee good images the liquid cell is completely filled with buffer solution. Adding a large amount of liquid to the system can result in image instabilities and serious damage of the scan head, thus it is recommended to withdraw some of the buffer before slowly adding the enzymes. The liquid cell can be refilled with buffer solution after applying the enzymes.

The procedure remains the same for experiments with spin-cast-cellulose (SCC) samples. They are previously carefully scratched with tweezers so that the wafer surface can be used as a reference plane and are immersed in buffer shortly before the investigations to allow swelling of the layers. Images are taken at the edge of the cellulose layer.

AFM-imaging is done on a Dimension 3100 (Digital Instruments, VEECO) with a Hybrid X-Y-Z closed loop scan head and a Nanoscope IVa controller. The liquid cell is an in-house construction developed by T. Ganner [3].

The degradation and roughness analysis is performed with the NanoScope Analysis 1.40 by Bruker. For quantitative degradation measurements to obtain degradation velocities  $v_d$ , the step tool in the analysis software is used. The height differences between a surface marker (they stay almost unaffected by the enzymatic attack) and a clearly degraded region is measured during the course of the experiment. Degradation is approximated by a linear model unless otherwise stated, leading to a value for the degradation velocity. This procedure is repeated on several areas on the sample. The average values serve as mean degradation velocity of the whole system. For roughness analyses,  $R_q$  values are used which represents the root mean square average of height deviations taken from the mean image data plane.

## 6.1 Further developments of FSEC samples

The preparation of FSEC samples has been optimized since their introduction by J. Dohr [2]. The samples resulting from the procedure that closely follows the protocol when the FSEC samples were first introduced (see chapter 4.2), are denoted as FSEC1 samples. The investigations by T. Ganner and T. Aschl were also conducted on these FSEC1 samples [3, 4].

The need for samples with tunable properties, especially the controlled embedding of Avicel residue crystals led to the introduction of FSEC2 samples. Extra Avicel crystals are added to the already solved mixture. The additional Avicel flakes should provide crystals suitable for reference purposes in the enzymatic degradation AFM experiments. Those Avicel residues are already known from the FSEC1 samples, the FSEC2 samples however should provide the possibility to influence the properties of the substrate more precisely.

The newly introduced FSEC2 samples are analysed by LIMM, XRD, and Raman spectroscopy. The utilisability is tested by performing a series of AFM experiments with known cellulases in combination with the exciting GH61 enzyme. These experiments show that the FSEC2 samples are not appropriate

for the enzymatic degradation purposes as almost no crystalline residues which should serve as surface markers for quantitative measurements can be found. This fact leads to the introduction of novel FSEC3 samples and the introduction of very different SCC substrates (see chapter 6.3). Several properties of the three types of FSEC samples are compared throughout this chapter.

### 6.1.1 LIMI of FSEC

Fig. 28 presents light microscopy images of FSEC1, FSEC2, and FSEC3 samples. All three samples show both amorphous and crystalline features. In each image one crystalline Avicel residue is marked by a red frame. These areas are examined in more detail by Raman spectroscopy together with the surrounding amorphous regions. Already in LIMI images differences in the morphology of the amorphous matrix of the three samples can be noticed (Fig. 28). The surface of FSEC1 is rather rough with a lot of scattered crystalline inclusions. The amorphous matrix of FSEC2 is smoother, the crystalline features are clearly defined. The FSEC3 surface shows the smoothest amorphous matrix of the FSEC samples, also here the crystalline residues are clearly defined. These variances can be traced back to the solution process of Avicel in the ionic liquid. The FSEC1 surface displays a lot of undissolved crystalline features. In FSEC2 the solution appears to be enhanced and the FSEC3 samples a very smooth surface with isolated Avicel residues. These differences can be perceived by comparing the red boxes of each FSEC sample in Fig. 28. Detailed investigations by XRD, Raman spectroscopy and AFM will give deeper insight later.



**Fig. 28:** LIMI images of FSEC1 (left), FSEC2 (middle) and FSEC3 (right) samples. The red squares indicate the area for the subsequent characterisation experiments via Raman spectroscopy.

### 6.1.2 XRD of FSEC

The main purpose of XRD investigations of FSEC samples is to see differences in the crystalline structures due to the preparation process of the different samples on an integral length scale. The XRD spectra of FSEC1, FSEC2, FSEC3 and Avicel can be seen in Fig. 29. The curves are normalized to the highest peak and smoothed via FFT filters along 15 points. Avicel consists of cellulose I with the main peak at  $2\theta = 22.7^\circ$  and side peaks at  $15^\circ$  (see also Fig. 22 for cellulose I and cellulose II reference spectra); the Avicel spectrum (black) serves as a highly crystalline reference to evaluate the solubility of Avicel in the samples by looking at the shifts of the main peaks. Generally, intense sharp peaks indicate high crystallinity, whereas wider peaks point to amorphous, hence unordered cellulose. The FSEC1 (blue) main peak is slightly shifted to higher angles by about  $0.3^\circ$  indicating unsolved Avicel in the sample. The small side lobe at approx.  $20^\circ$  represents the amorphous matrix of FSEC1. The double-peak of FSEC2 (red) implies incorporation of much Avicel in the cellulose II matrix. The shift of the FSEC3 (olive) peak to lower angles denotes good solution of the Avicel within the sample, which contains a lot of well-solved cellulose II (see [4] for a detailed description). Particularly, the differences

between FSEC1 and FSEC3 which can already be seen in the LIM images (Fig. 28) are confirmed by the results of the XRD investigations. The decrease of crystallinity is unambiguously proven by the shift to lower angles and the broadening of the FSEC3 peak in comparison to the FSEC1 peak. The results of XRD confirm that it is possible to alter the properties of the samples by varying the mixing method during preparation which was the initial intention.

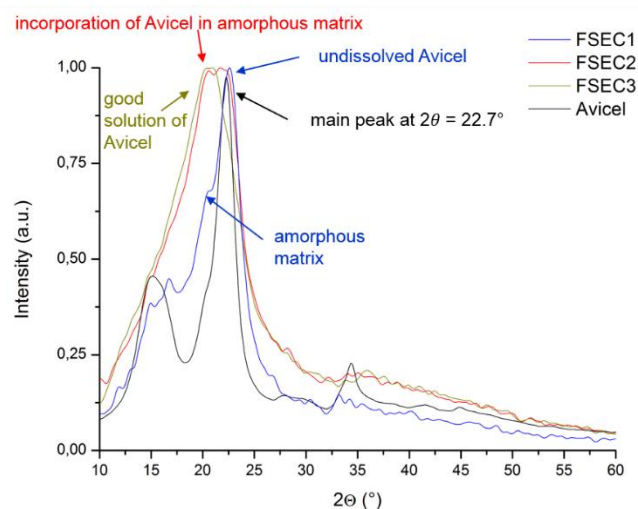
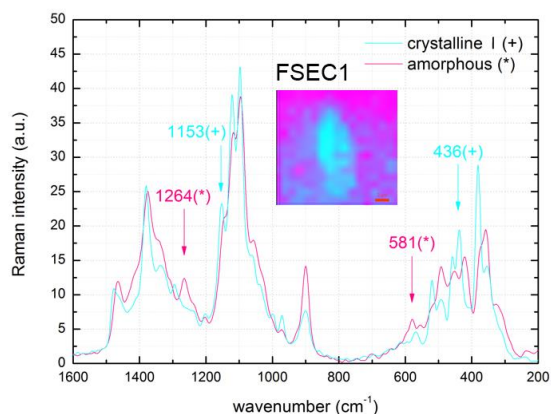


Fig. 29: XRD spectra of FSEC1 (blue), FSEC2 (red), FSEC3 (olive) and Avicel (black).

### 6.1.3 Raman spectroscopy of FSEC

Raman spectra of FSEC1, FSEC2 and FSEC3 samples are shown in Fig. 30, Fig. 31, and Fig. 32. The curves are normalized and FFT smoothed (3 points). Signals from amorphous and crystalline regions are detected and used for mapping (see inlets in the spectra) of the marked regions in the LIM images (Fig. 28). The inlets represent the morphology of the FSEC samples clearly: crystalline features (cyan) are surrounded by a matrix of amorphous cellulose (pink). The characteristic peaks of amorphous cellulose at  $1264\text{ cm}^{-1}$  and  $581\text{ cm}^{-1}$  (marked by \*) can be assigned in the spectra of the amorphous matrix (drawn in pink) of the FSEC samples. The crystalline spectra (drawn in cyan) correspond to the structure of cellulose I with its characteristic peaks at  $1151\text{ cm}^{-1}$  and  $436\text{ cm}^{-1}$  (marked by +). This confirms that the Avicel residues consist of cellulose I and can be found in all three types of FSEC samples where they are embedded in an amorphous matrix.



**Fig. 30:** Raman spectra of a FSEC1 sample. The insert shows a mapping of the marked region in the LIMI images in Fig. 28. The cyan curve represents the crystalline spectrum with its characteristic peaks (marked by +). The pink curve shows the amorphous spectrum with its characteristic peaks (marked by \*).

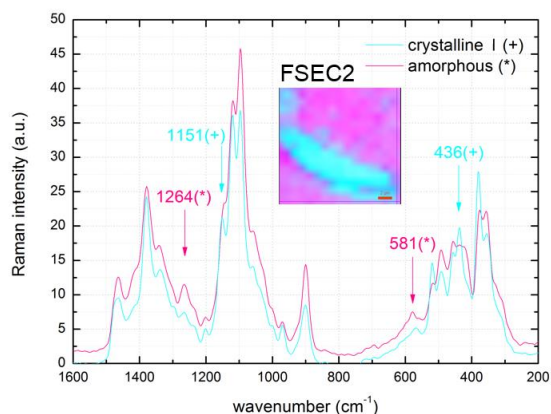


**Fig. 31:** Raman spectra of a FSEC2 sample. The insert shows a mapping of the marked region in the LIMI images in Fig. 28. The cyan curve represents the crystalline spectrum with its characteristic peaks (marked by +). The pink curve shows the amorphous spectrum with its characteristic peaks (marked by \*).

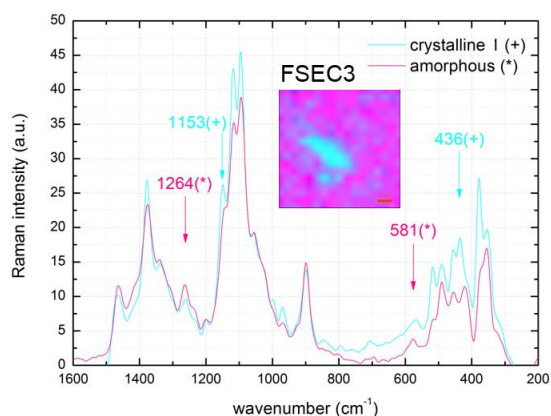


**Fig. 32:** Raman spectra of a FSEC3 sample. The insert shows a mapping of the marked region in the LIMI images in Fig. 28. The cyan curve represents the crystalline spectrum with its characteristic peaks (marked by +). The pink curve shows the amorphous spectrum with its characteristic peaks (marked by \*).

### 6.1.4 AFM of FSEC

LIMI, XRD and Raman investigations showed that the FSEC2 samples are an improvement of the FSEC1 samples with respect to the solution of Avicel within the amorphous matrix. Besides, the FSEC2 samples exhibit the desired Avicel cellulose I residues. As a consequence the FSEC2 samples are used in a series of AFM experiments in liquid environments to examine the influence of the interesting GH61 enzyme on cellulose and on the cellulases CBH1, CBH2, and EG1 to test their suitability for enzymatic degradation experiments (see chapter 6.2).

AFM phase images of FSEC1, FSEC2, and FSEC3 samples are compared in Fig. 33. It turns out that the desired Avicel residues can only be found in the FSEC1 and FSEC3 samples (marked by blue frames) but not in the FSEC2 as actually expected.

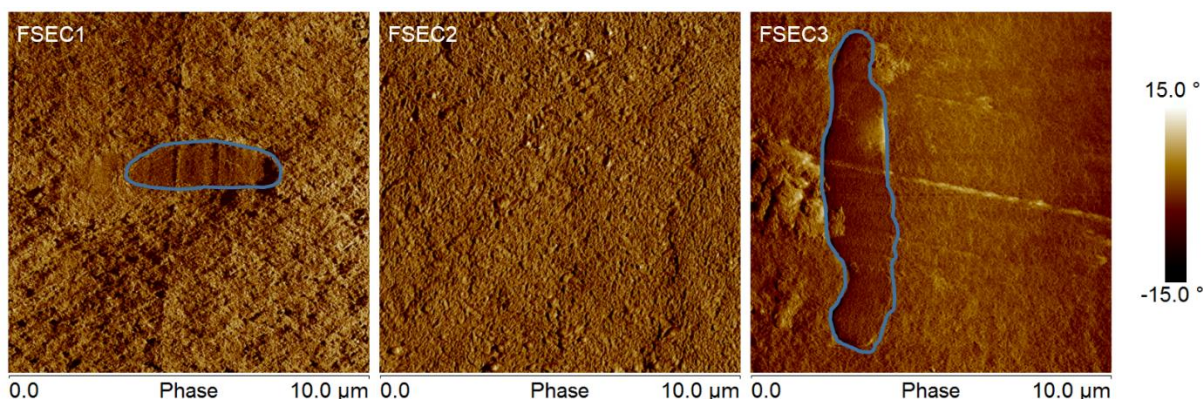


Fig. 33: 10  $\mu\text{m}$  AFM phase images of a FSEC1 (left), FSEC2 (middle), and FSEC3 (right) sample. The blue frames mark Avicel residues in the FSEC1 and FSEC3 samples. Such residues can barely be found in the FSEC2 samples.

Detailed AFM investigations of FSEC2 samples in liquid provide a variety of AFM images which can be found in the next section (chapter 6.2) and reveal that the structure is very amorphous with few distinct crystalline features (see Fig. 48 and Fig. 51 in chapter 6.2.4 for 10  $\mu\text{m}$  overview images). The  $R_q$  values of the amorphous regions are comparable to those of the FSEC1 samples ( $R_q \approx 10 - 30 \text{ nm}$ ); however, the new FSEC2 samples show almost no crystalline residues, which can be used as surface markers, even though extra Avicel flakes are added. During ultramicrotomy preparation these Avicel flakes tend to be torn out of the rather soft surface. This fact complicates the cutting of the sample and makes it on the one hand difficult to obtain well-prepared samples. On the other hand performing quantitative measurements of enzymatic degradation becomes very challenging due to the missing crystalline features acting as reference markers. Thus the new type of sample does neither facilitate the analysis nor allow the preparation of samples with well-defined properties.

When comparing the FSEC2 samples used for the experiments with GH61 in chapter 6.2, it seems that the surface textures of the samples are not as reproducible as for FSEC1 samples. In FSEC1 and in particular in FSEC3 (see Fig. 33) samples Avicel residues can easily be found. See and compare Fig. 34 to Fig. 51 in chapter 6.2 to get a good overview of the morphological and topographical sample properties of FSEC2.

Moreover, influence of the AFM tip can be observed after several hours of measurement on the FSEC2 substrate (see blue boxes in Fig. 48 and Fig. 51 in chapter 6.2.4) even though the investigations are conducted in non-contact mode (tapping) in the attractive regime. The substrate is very soft after several hours of measurement. To some extent the softening of the samples can be traced back to the influence of the GH61 enzyme, but it is clearly visible that only in the area of measurement the gaps are widened. Regions where the AFM tip is not present are evidently less affected. These tip influences have never been observed in AFM measurements (both with and without GH61) on FSEC1 samples.

AFM investigations of FSEC2 show that this sample type is not suitable for the quantitative and structure dependent (detailed analysis of degradation of crystalline and amorphous regions) analysis of enzymatic degradation experiments.

### 6.1.5 Summary FSEC

Investigating the properties of the newly introduced FSEC2 samples by LIMM, XRD and Raman spectroscopy show no major differences to the well-tested FSEC1 samples. However, when conducting AFM enzymatic degradation experiments in liquid environments with these samples it turns out, that the FSEC2 samples do not serve the purpose of facilitating the quantitative analysis and the well-defined tuning of the sample properties. The FSEC2 surfaces lack in suitable reference markers, even though additional Avicel flakes should offer more residues. The flakes tend to stick together and are thus torn out of the surface during ultramicrotomy preparation. Nevertheless, FSEC2 samples provide exciting insights into the activity of the GH61 enzyme (see chapter 6.2).

Hence, it follows that a new way of tuning the samples has to be found; that is why the spin cast cellulose (SCC) samples were further developed as discussed in chapter 6.3. The spin casted samples are highly reproducible and represent the required crystalline features embedded in an amorphous matrix on a smaller scale than the FSEC samples. Nano-crystalline cellulose whiskers will serve as crystalline structures.

Still, the unsatisfactory properties of the FSEC2 samples lead to the introduction of a new type of FSEC samples. The mixing procedure of the FSEC3 samples is improved resulting in substrates with well-defined FSEC properties.

## 6.2 GH61 experiments

A series of degradation experiments is performed to investigate the behaviour of the exciting GH61 enzyme when applied on cellulose (FSEC1 and FSEC2 samples; see Table 3 for an overview). Furthermore its influence on cellulases such as CBH1, CBH2, EG1, and its supernatant (**SVG**, see also chapter 2.2.4) is studied. For this purpose reference experiments with the single cellulases are compared to combined investigations with GH61. GH61 has been reported to accelerate the enzymatic hydrolysis reaction by cleaving the cellulose chains without extracting them from their crystalline matrix; thus offering more accessible chain ends (see chapter 2.2.5) and speeding up the degradation process [16, 17, 18, 19]. This acceleration is tried to be observed by conducting enzymatic degradation experiments with a focus on the quantitative aspect of degradation. Moreover, the FSEC2 samples are tested in this series of investigations.

### Notes on the experimental procedure

The AFM experiments in liquid environments all follow the same procedure, which is explained in the introduction of chapter 6.

In the cellulase reference experiments the enzymes are applied for 4 hours. In the combined GH61-cellulase experiments the samples are first exposed to GH61 for 4 hours followed by at least 4 more hours of exposure to the correspondent cellulase. The concentration of the cellulases is chosen to be rather low as it is known that GH61 is quite sensitive to overconcentration of cellulases. All enzymatic mixtures include 15  $\mu$ l of  $\beta$ -glucosidase (**BGL**), which turns the cellobiose into glucose [1]. This supports the efficient degradation as cellobiose impedes the cellulases [14].

*All FSEC samples were prepared by Thomas Ganner; ultramicrotomy cuts were performed by Claudia Mayrhofer and Thomas Ganner at the Institute for Electron Microscopy and Nanoanalysis. All enzyme and buffer solutions were prepared by Manuel Eibinger from the Institute of Biotechnology and Biochemical Engineering (headed by Prof. Dr. Bernd Nidetzky). AFM-imaging was conducted on a Dimension 3100 (Digital Instruments, VEECO) with a Hybrid X-Y-Z closed loop scan head and a Nanoscope IVa controller at the Institute for Electron Microscopy and Nanoanalysis.*

### 6.2.1 Supernatant on FSEC1

The used SVG supernatant consists of CBH1, CBH2, EG1, and BGL and is expected to degrade both crystalline and amorphous regions due to the exo- and endo-glucanases in the mixture. The activity is expected to be higher than in the single cellulase experiments as a result of the synergistic effects in the supernatant. See Table 3 in the introduction of chapter 6 and Fig. 52 in section 6.2.5 for a comparison of the experiments.

#### SVG reference experiment on FSEC1

Before and after exposure 10  $\mu$ m height images can be seen in Fig. 34. After 5 hours of exposure to the supernatant the surface has clearly changed, degradation is well visible. The crystalline residue (marked by blue frames in Fig. 34) stays largely unchanged during exposure. Hence, quantitative analysis of the degradation process is possible as this residue serves as absolute surface marker for the changes in height. The amorphous matrix surrounding the crystalline residue is heavily degraded. During the degradation process, embedded crystalline features are excavated and degraded as well. The degradation

of the amorphous matrix and the excavation of internal crystalline features can also be seen in Fig. 35 which shows a 3D-detail of the crystalline residue (marked by blue frames) before and after exposure to SVG for 5 hours. The overall structure of this reference zone remains largely unaffected by SVG. The blue arrows in Fig. 35 mark grooves caused by ultramicrotomy. The green arrows indicate excavated crystalline features. Thorough height degradation and roughness analysis leads to an overall degradation velocity of  $v_{d,SVG} = 0.8 \pm 0.3 \text{ nm/min}$  and the  $R_q$  value in the  $10 \mu\text{m}$  overview images increases from 39 nm to 107 nm. The values obtained in this experiment will be compared to the results from the GH61/SVG experiment in the following section.

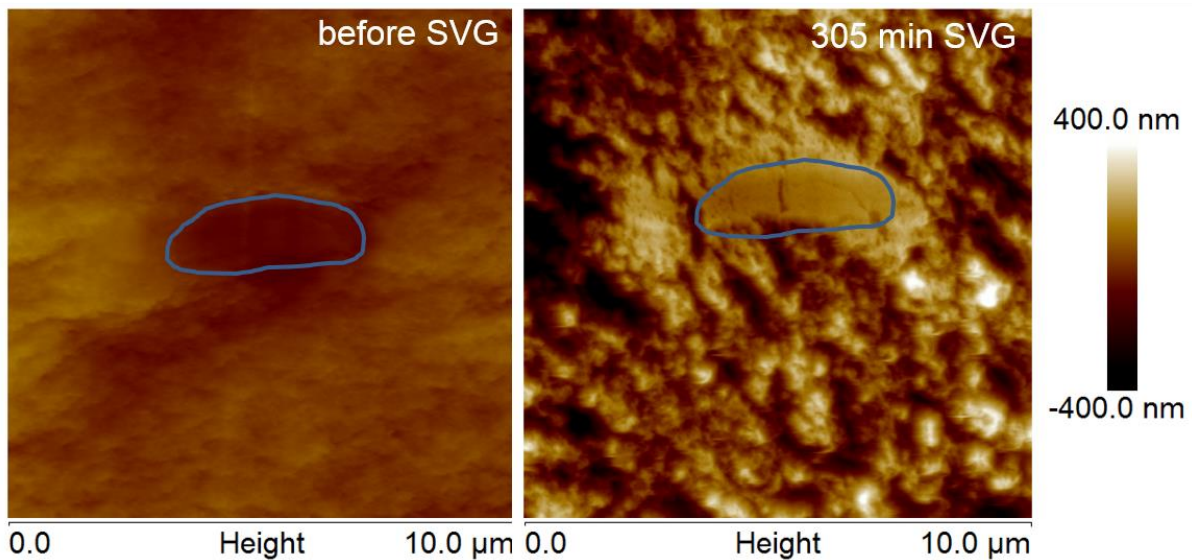


Fig. 34: Before (left) and after (right) exposure  $10 \mu\text{m}$  height images of a FSEC1 sample. SVG is applied for 5 hours. The blue frames mark the crystalline reference residue.

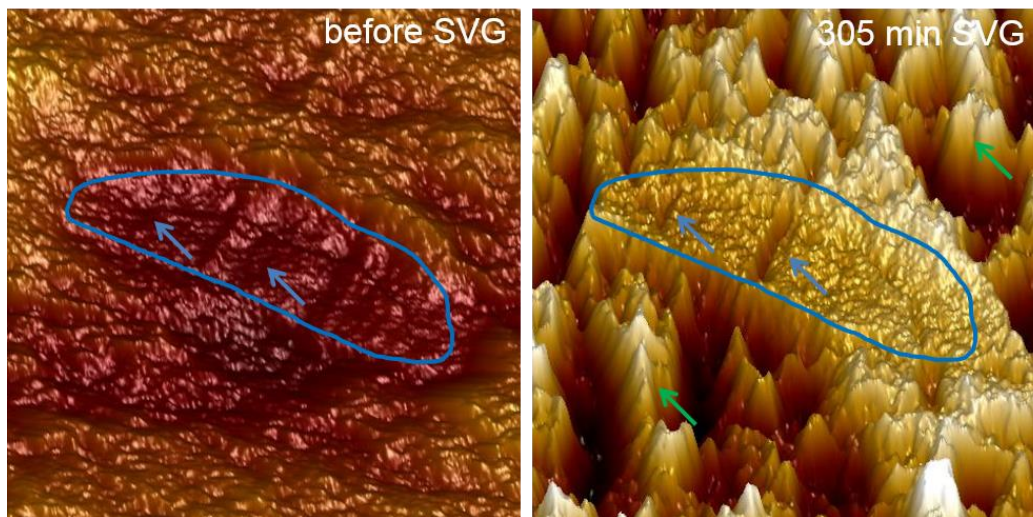
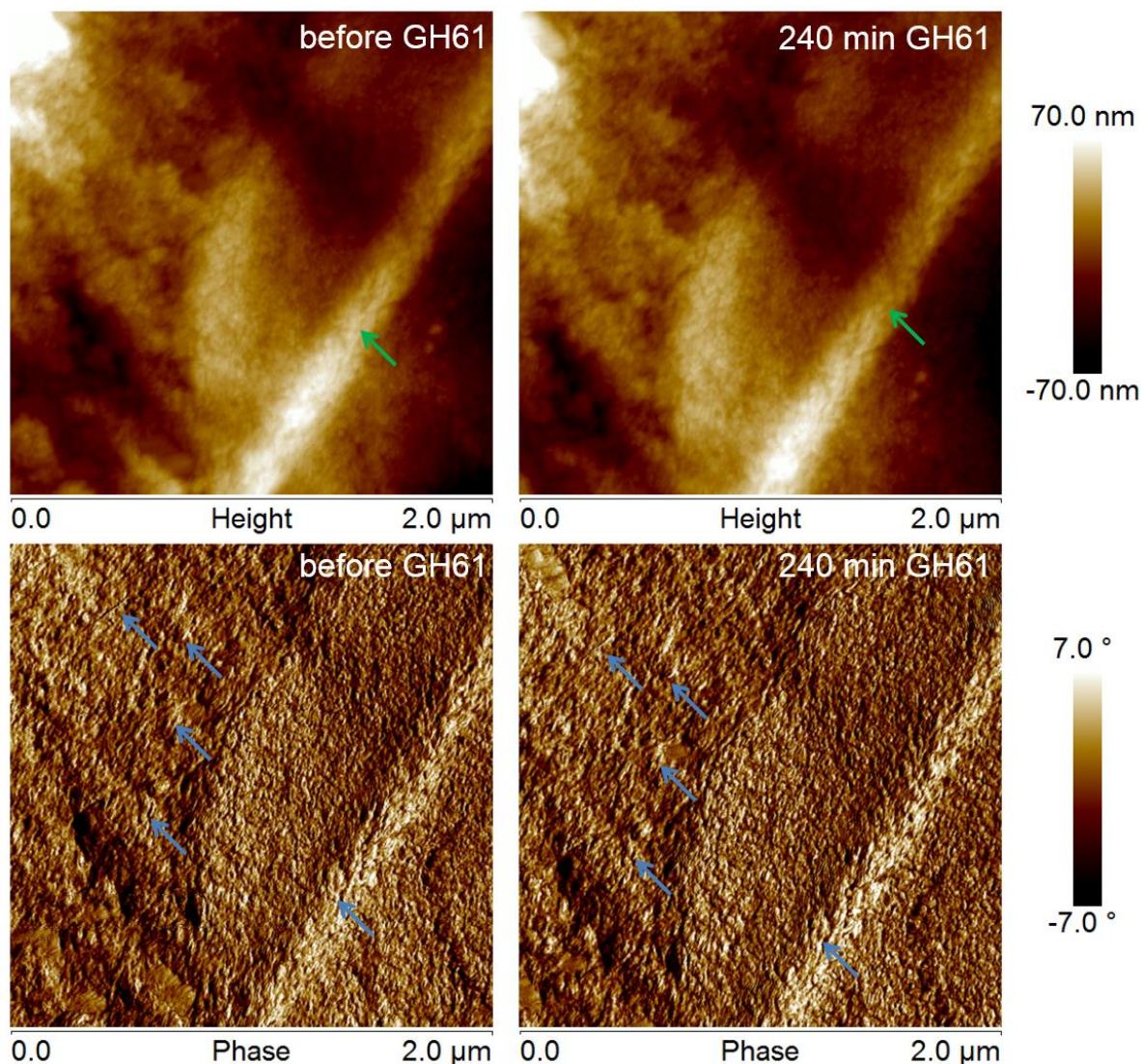


Fig. 35: 3D-height details of the crystalline residue in Fig. 34. The residue is marked by a blue frame in the images before (left) and after (right) exposure to SVG. The blue arrows point at grooves caused by ultramicrotomy; the green arrows indicate internal crystalline features that are excavated.

### GH61/SVG experiment on FSEC1

Fig. 36 shows before-after  $2 \mu\text{m}$  height and phase images of the GH61 exposure; comparing the height images (upper row) before and after 4 hours of exposure reveals that GH61 has practically no effect on

the FSEC1 sample, neither on the residue in the right half of the selected area (green arrows point at the groove caused by ultramicrotomy that goes right through the residue) nor on the surrounding cellulose matrix. This fact is substantiated by the phase images (lower row), as no changes in the structure can be found, not even by very thorough height degradation and roughness analysis. In the phase images blue arrows point at several of the crystalline fibres that remain unaffected by GH61.



**Fig. 36:** Before (left) and after (right) exposure 2 μm height (top) and phase (bottom) images of a FSEC1 sample. GH61 is applied for 4 hours. The green arrows indicate the groove caused by ultramicrotomy that goes right through the residue. The blue arrows in the phase images mark several of the crystalline fibres that are unaffected by the enzymes.

These investigations are repeated after adding the SVG supernatant consisting of CBH1, CBH2, EG, and BGL. Like in the SVG reference experiment the matrix surrounding the crystalline residue is clearly degraded, internal crystalline features are excavated. Interesting results are obtained from degradation analysis: GH61 boosts the degradation velocity of SVG, which now reaches  $v_{d,GH61+SVG} = 1.4 \pm 0.2 \text{ nm/min}$  compared to  $v_{d,SVG} = 0.8 \pm 0.3 \text{ nm/min}$  for SVG without GH61! See Fig. 52 in section 6.2.5 for a comparison of the degradation velocities  $v_d$  of the GH61 experimental series. The  $R_q$  values of the 10 μm overview in Fig. 37 before and after SVG exposure increase from 35 nm to 53 nm and do not change as heavily as in the SVG reference experiment (39 nm to 107 nm). This indicates a much more homogenous degradation of SVG after prior exposure to GH61.

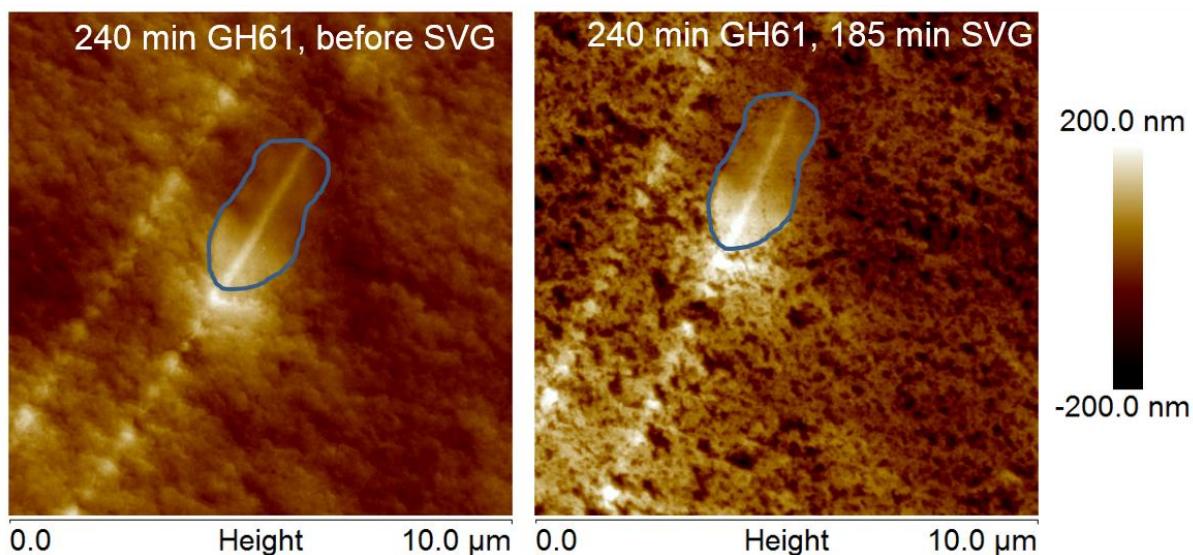


Fig. 37: Before (left) and after (right) exposure 10  $\mu\text{m}$  height images of a FSEC1 sample. After 4 hours of GH61 SVG is applied for 3 hours. The blue frames mark the crystalline reference residue.

## 6.2.2 EG1 on FSEC1 and FSEC2

EG1 is an endo-glucanase known to be active on amorphous cellulose (see also chapter 2.2.3). Hence amorphous structures on the cellulose sample's surface are expected to be degraded and crystalline features to be revealed.

### EG1 reference experiment on FSEC2

Fig. 38 depicts 2.5  $\mu\text{m}$  3D height images before and after EG1 exposure on a FSEC2 sample. Apart from the residue in the left part of the image before applying the enzymes the sample is very smooth, making the quantitative measurement of degradation rather cumbersome. The alleged residue disappears during the course of the experiment, most likely the tip moved the feature that sticks out of the rather amorphous surface. As a result of this severe change in image topology no clear conclusion can be drawn from roughness analysis.

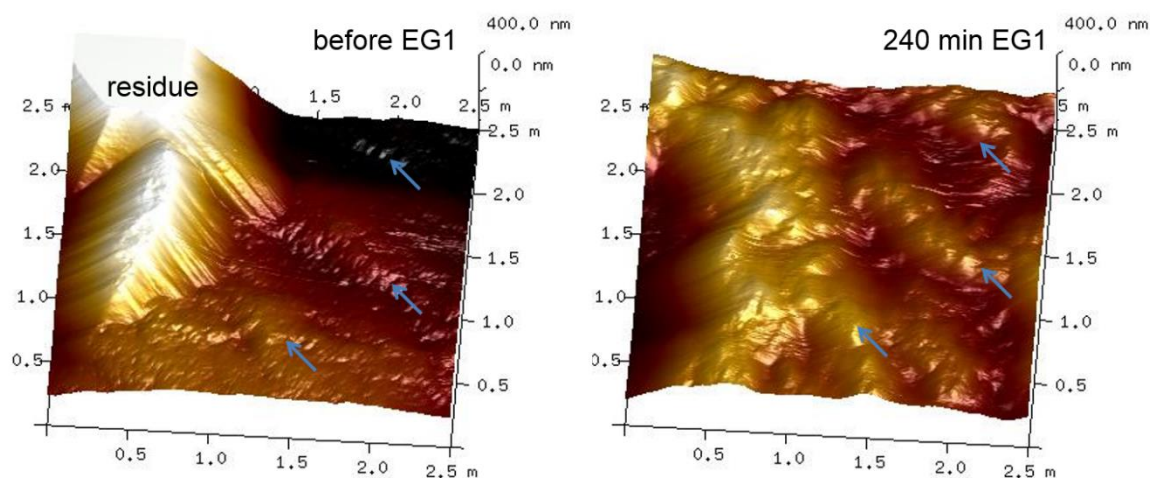


Fig. 38: Before (left) and after (right) exposure 2.5  $\mu\text{m}$  3D height images of a FSEC2 sample. EG1 is applied for 4 hours. The blue arrows mark regions of higher crystallinity than the amorphous matrix which are excavated by EG1.

Nevertheless degradation of amorphous regions is clearly visible and can be estimated by  $v_{d,EG1} = 0.4 \pm 0.2 \text{ nm/min}$ . However, no distinct crystalline features as known from FSEC1 samples are excavated by EG1. Only regions with assumed higher crystallinity can be recognized in the image after 240 min of EG1 exposure (right image in Fig. 38). Moreover, information via height images is slightly reduced which could refer to conglomeration of material on the tip and swelling of the sample. This reduction can also be seen in Fig. 39 which displays a sequence of height images during EG1 exposure. The features become more indistinct during the course of exposure. Blue arrows in Fig. 39 point at amorphous regions that are degraded by EG1, several gaps evolve during exposure and widen up. Green arrows indicate the above mentioned regions of higher crystallinity that are excavated. All these findings give first hints of the difficult handling of FSEC2 samples in enzymatic degradation experiments.

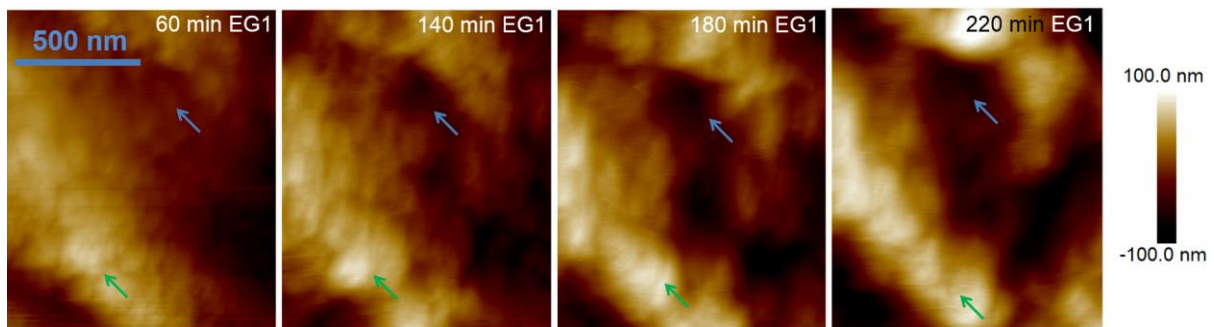
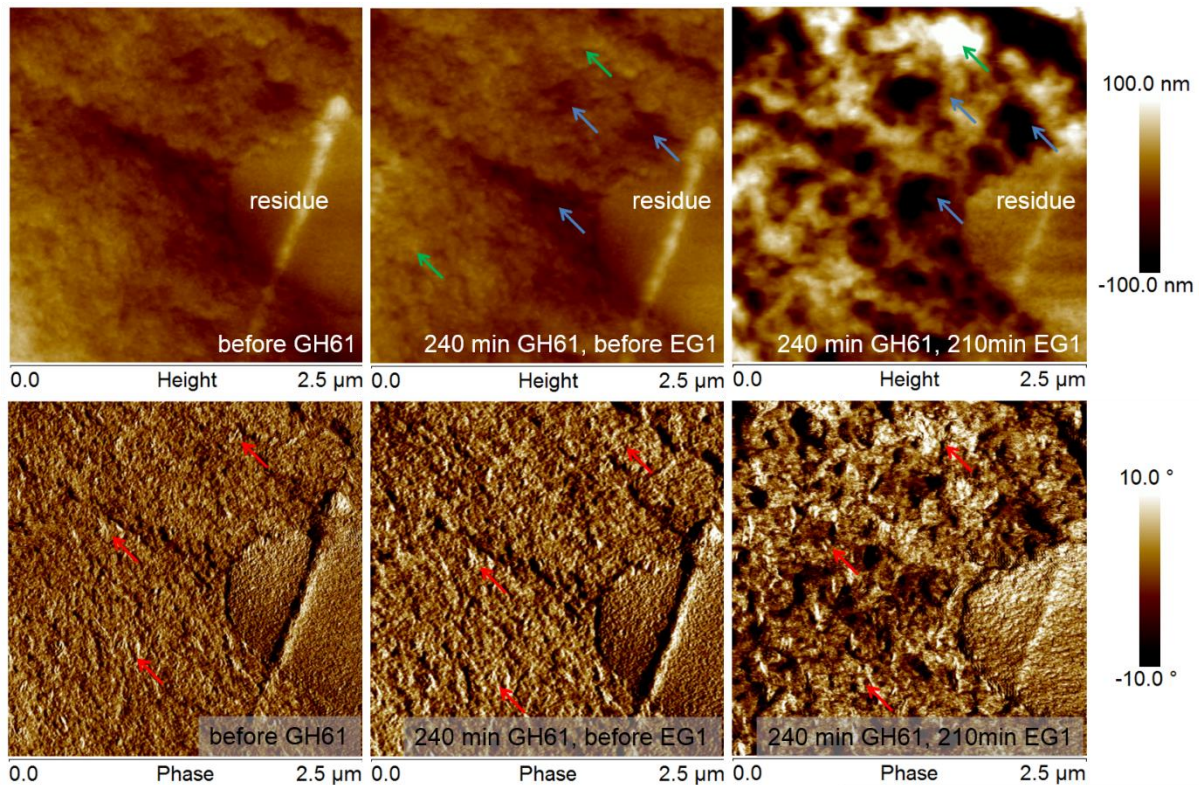


Fig. 39: Sequence of height images during EG1 exposure. The scale bar is 500 nm. Blue arrows point at amorphous regions that are degraded by EG1. Green arrows indicate regions with higher crystallinity that are excavated.

### GH61/EG1 experiment on FSEC1

Several attempts on FSEC2 samples display the degradation by EG1 unmistakably; however they lead to no reliable results when analysing the degradation quantitatively. The used FSEC2 samples are too smooth and show no crystalline features that could be used as surface markers or to identify potential effects of GH61. Thus one of the well-tested FSEC1 samples is used for the combined GH61/EG1 experiment. A sequence of height (upper row) and phase (bottom row)  $2.5 \mu\text{m}$  images of the GH61 and EG1 exposure can be seen in Fig. 40. The crystalline residue is clearly visible. Applying GH61 to the FSEC1 sample shows again no effects; this is also observed with the FSEC1 sample in the GH61/SVG experiment. No changes can be seen in the height images; the phase images depict slight soaking, but the structure stays the same. Undoubtedly, the sample is degraded during subsequent exposure to EG1. Continuous observation of the phase signal in particular evince, that the crystalline fibres are excavated by the enzymes, which are known to act predominantly on amorphous cellulose [14, 15]. Blue arrows in the height images mark amorphous regions that are degraded. Green arrows point at excavated crystalline features (by EG1). The red arrows in the phase images indicate crystalline features that stay unaffected by GH61 and excavated by EG1. The measurements result in a degradation velocity of  $v_{d,GH61+EG1} = 0.5 \pm 0.1 \text{ nm/min}$ . This corresponds to a small yet substantial increase of  $0.1 \text{ nm/min}$  compared to the EG1 reference experiment ( $v_{d,EG1} = 0.4 \pm 0.2 \text{ nm/min}$ ; see Fig. 52 in section 6.2.5 for a comparison of the degradation velocities  $v_d$  of the GH61 experimental series). These findings could be confirmed by roughness analysis. The  $R_q$  value before and after GH61 is stable around  $17 \text{ nm}$  and increases to  $48 \text{ nm}$  after EG1 exposure.



**Fig. 40:** Sequence of 2.5  $\mu\text{m}$  height (top) and phase (bottom) images of a FSEC1 sample. The left images are taken before exposure to GH61, the images in the middle show the sample after 4 hours of GH61 and right before exposure to EG1. The right images point to amorphous regions. Blue arrows in the height images illustrate the situation after 3.5 hours of EG1 exposure. The residue is marked. Blue arrows in the height images point to amorphous regions. Green arrows indicate crystalline structures that are excavated by EG1. In the phase images the red arrows mark crystalline features that are not affected by GH61 and excavated by EG1.

### 6.2.3 CBH2 on FSEC2

CBH2 is an exo-glucanase which works on crystalline structures but has also been observed to be active on amorphous cellulose by T. Ganner [3, 15]. Thus the amorphous matrix of the FSEC2 sample is expected to be cleared away and crystalline features will be excavated which are then affected by CBH2 as well.

#### CBH2 reference experiment on FSEC2

A very homogenous, amorphous FSEC2 substrate serves as sample. After 290 minutes of exposure to CBH2 the roughness value  $R_q$  increases from 32 nm to 84 nm and features with higher crystallinity are excavated. This corresponds to the expected behaviour of the enzyme. Fig. 41 shows before-after 3D height images of the degradation process. The mean degradation velocity can be estimated by  $v_{d,CBH2} = 0.6 \pm 0.2 \text{ nm/min}$ . In the height images sequence in Fig. 42 the effect of CBH2 on the regions of assumed higher crystallinity can be seen. Certain features (marked by blue and green circles) are excavated during exposure and then degraded as well.

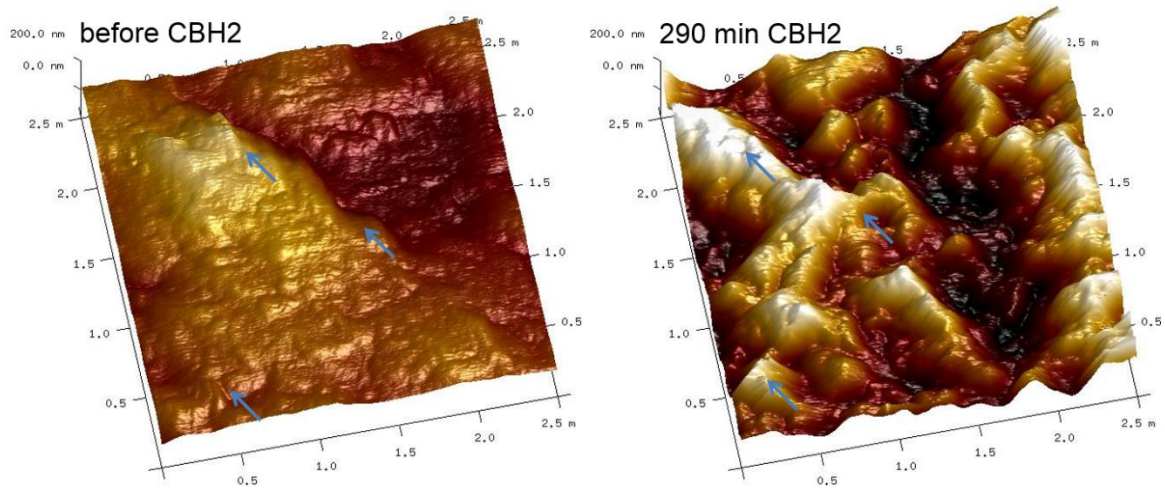


**Fig. 41:** Before (left) and after (right) exposure 2.5  $\mu\text{m}$  3D height images of a FSEC2 sample. CBH2 is applied for almost 5 hours. The blue arrows mark regions of higher crystallinity that are excavated by CBH2.

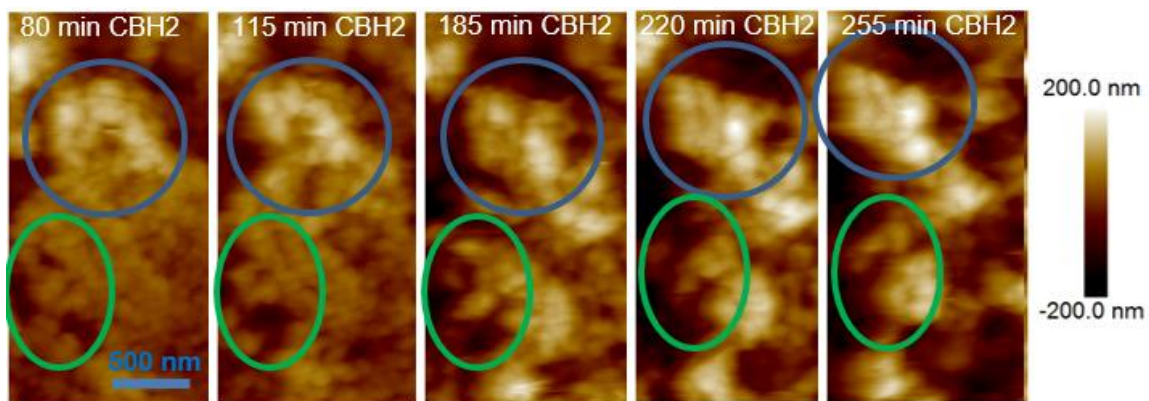


**Fig. 42:** Sequence of height images during CBH2 exposure. The scale bar is 500 nm. Blue and green circles mark regions of higher crystallinity that are excavated and degraded by CBH2.

### **GH61/CBH2 experiment on FSEC2**

The GH61/CBH2 experiment is also conducted on a FSEC2 sample, which this time shows some crystalline features. Fig. 43 shows before-after 2.5  $\mu\text{m}$  height and phase images of the GH61 exposure. During single GH61 exposure (to some extent tip induced) widening of existing gaps can be observed in the height images (marked by green arrows in Fig. 43) and slight alteration of some crystalline features in the phase images (marked by blue and red arrows in Fig. 43) can be seen as well. Tip influence cannot be excluded but is definitely smaller than e.g. in the GH61/CBH1 experiments (see chapter 6.2.4). Due to tip-induced changes in topology roughness analysis provides no clear results (same for the EG1 reference experiment in chapter 6.2.2). Undeniably, the substrate is degenerated during the course of exposure to CBH2 (see Fig. 44). The degradation velocity averages  $v_{d, \text{GH61+CBH2}} = 1.3 \pm 0.2 \text{ nm/min}$ . In comparison to the CBH2 reference experiment ( $v_{d, \text{CBH2}} = 0.6 \pm 0.2 \text{ nm/min}$ ) this corresponds to a doubling of the degradation velocity (see Fig. 52 in section 6.2.5 for a comparison of the degradation velocities  $v_d$  of the GH61 experimental series). GH61

enhanced the efficiency of degradation in this experiment as well! The behaviour of degradation of CBH2 is not changed by GH61. Also in the GH61/CBH2 experiment degradation of amorphous regions reveals regions of higher crystallinity, which are then degraded as well. This behaviour is well represented by the height image sequence in Fig. 42 in the CBH2 reference experiment, the similar effects observed in the GH61/CBH2 experiment are not shown here.

Still, the FSEC2 samples do not feature the expected well-defined crystalline properties, which would allow uncomplicated structural and quantitative analysis of the degradation process.

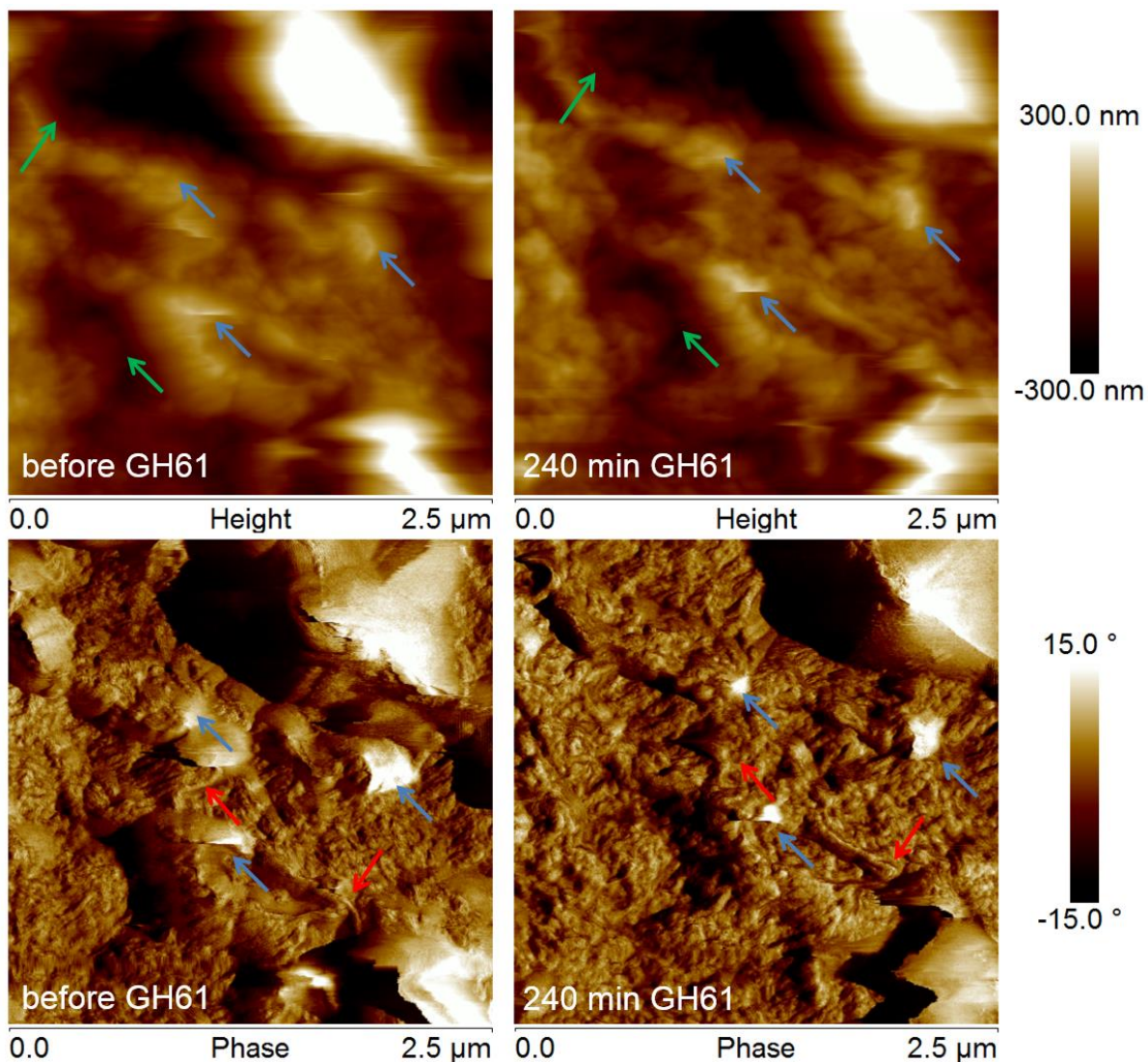


**Fig. 43:** Before (left) and after (right) exposure 2  $\mu\text{m}$  height (top) and phase (bottom) images of a FSEC2 sample. GH61 is applied for 4 hours. Green arrows in the height images indicate widening of already existing gaps. The blue arrows in the height and the phase images indicate assumed crystalline regions that are affected by GH61. The green arrows in the phase images mark additional crystalline features that are altered.

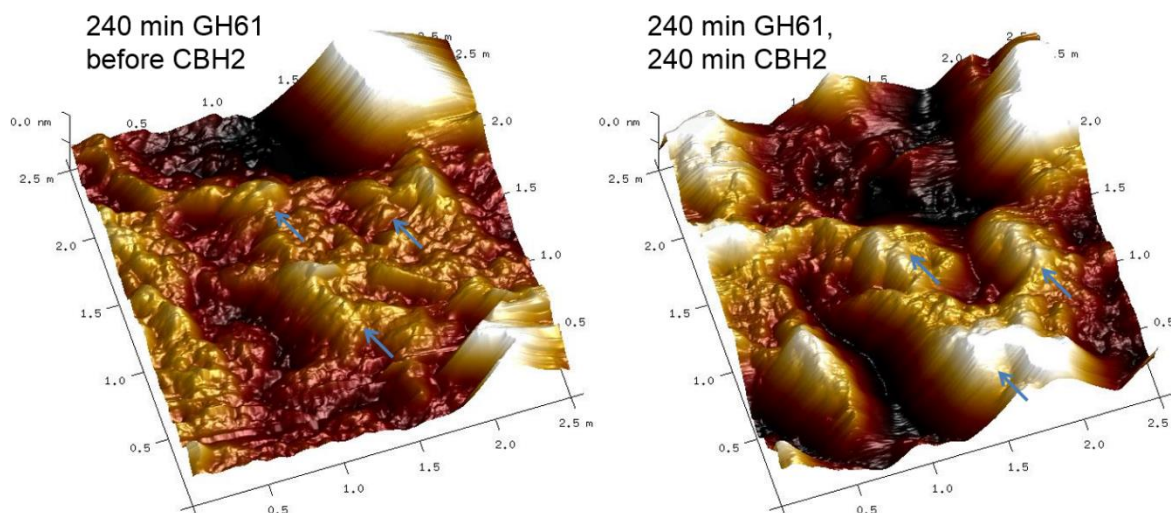


**Fig. 44:** Before (left) and after (right) CBH2 exposure 2.5  $\mu\text{m}$  3D height images of a FSEC2 sample. After 4 hours of GH61, CBH2 is applied for 4 hours. The blue arrows mark regions of higher crystallinity that are excavated by CBH2.

## 6.2.4 CBH1 on FSEC2

CBH1 is an exo-glucanase, which attacks crystalline structures of cellulose. Exposing FSEC2 samples to this cellulase is expected to reveal if there are crystalline features embedded in the amorphous matrix that can be degraded by CBH1.

### CBH1 reference experiment on FSEC2

A very smooth, amorphous FSEC2 substrate serves as sample. Fig. 45 shows 1.5  $\mu\text{m}$  height images before and after the degradation process. Excavation of crystalline features cannot be observed in contrast to the effects of CBH2 (and GH61/CBH2, see chapter 6.2.3) on the FSEC2 samples. Still, degradation can be detected. The blue arrows in Fig. 45 mark gaps that are widened during exposure to CBH1. Apparently, the sample offers crystalline features hidden in the amorphous matrix which are accessible for CBH1. The phase images are too indefinite to give clear insights into the degradation process in detail and are thus not shown here. Once more this indicates the complicated handling of FSEC2 samples in enzymatic degradation experiments, as they do not show distinct crystalline features. Nevertheless, roughness analysis can be conducted and provides an increase from  $R_q = 13 \text{ nm}$  to  $28 \text{ nm}$  after 190 minutes of exposure to CBH1. This slight change indicates that the degradation is very homogeneous. The minimal degradation velocity can be estimated by  $v_{d,CBH1} = 0.6 \text{ nm/min}$ .

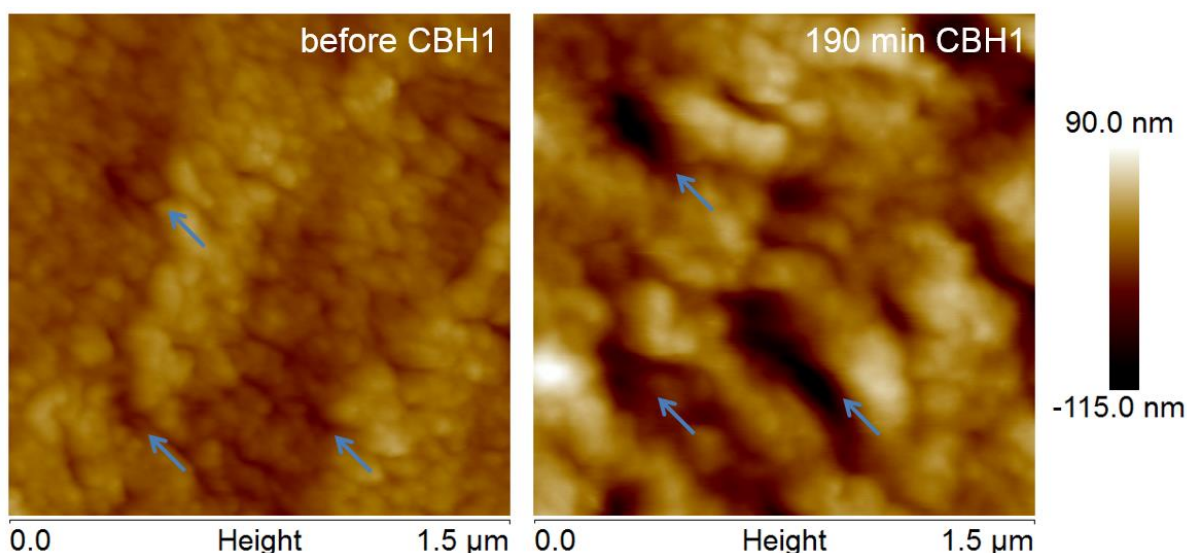
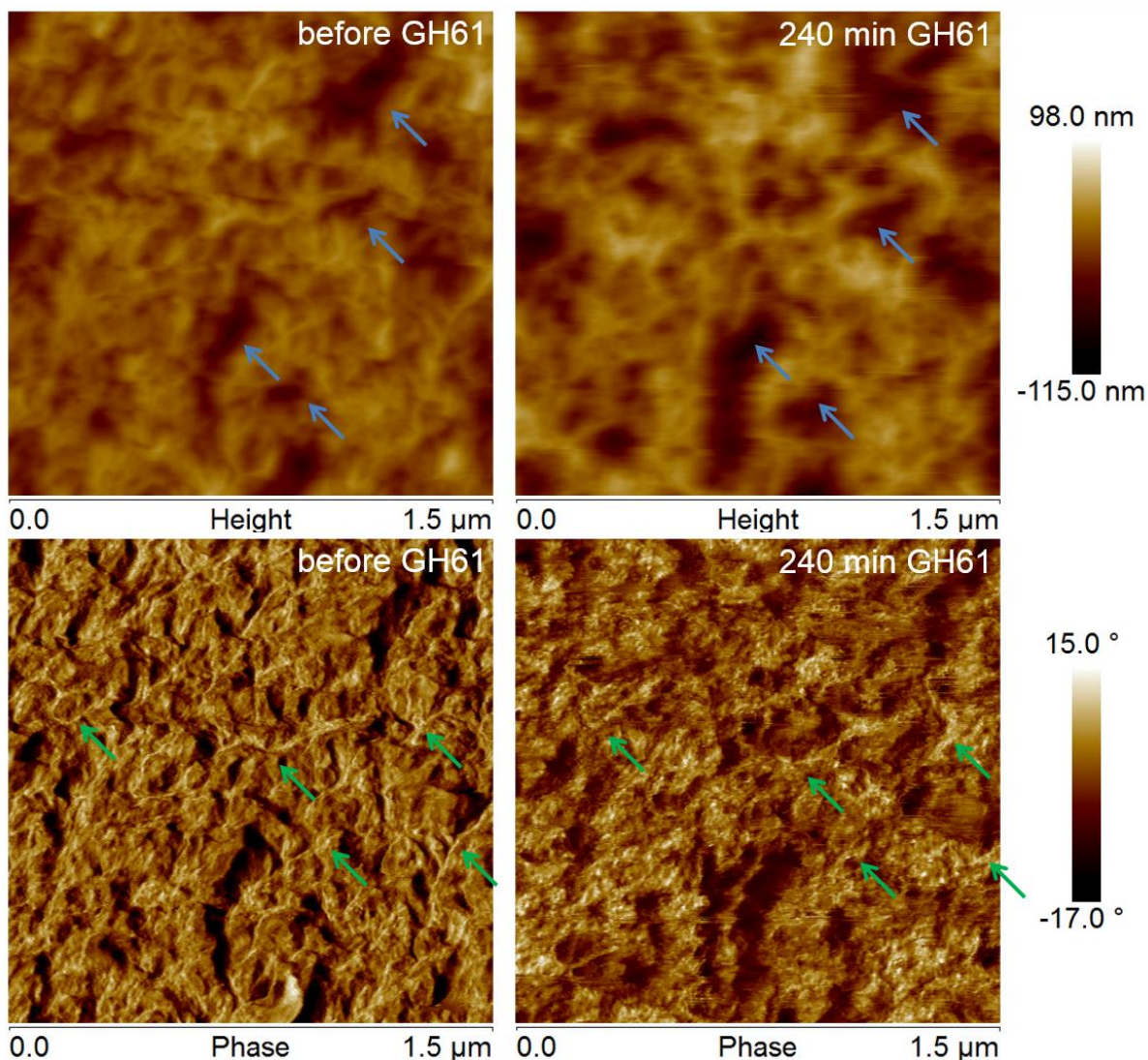


Fig. 45: Before (left) and after (right) exposure 1.5  $\mu\text{m}$  height images of a FSEC2 sample. CBH1 is applied for more than 3 hours. The blue arrows mark gaps that are widened during exposure to CBH1.

#### **GH61/CBH1 experiments on FSEC2**

As exposing a smooth FSEC2 sample to CBH1, which is known to be active predominantly on crystalline features, shows clear signs of degradation, the internal structure seems to offer sufficient points of contact for CBH1. Therefore the GH61/CBH1 combined experiments are also performed with the new FSEC2 substrate. The still very homogenous and highly amorphous FSEC2 samples make conditions for the AFM investigations very difficult. However, some interesting observations are obtained. GH61 seems to have a slight influence on this type of substrate. Fig. 46 shows before-after 1.5  $\mu\text{m}$  height and phase images of the GH61 exposure. A (to some extent influenced by the tip!) widening of the already existing gaps can be detected in the height images (marked by the blue arrows in Fig. 46) and the enzyme affects the few crystalline features during the single GH61 exposure as can be seen in the phase images (marked by green arrows in Fig. 46). Even though influences by the AFM tip (see Fig. 48, further explanation below) cannot be neglected in this experiment the effects of GH61 are nonetheless significant.



**Fig. 46:** Before (left) and after (right) exposure 1.5  $\mu\text{m}$  height (top) and phase (bottom) images of a FSEC2 sample. GH61 is applied for 4 hours. Blue arrows in the height images indicate widening of already existing gaps. The green arrows in the phase images indicate crystalline features that are affected by GH61.

Subsequent exposure to CBH1 can only be investigated qualitatively as there is no suitable crystalline marker available in this substrate. Fig. 47 displays before-after 2.5  $\mu\text{m}$  height images of the exposure to CBH1. No signs of degradation can be detected. Still, CBH1 shows slight influence on the substrate. By comparing several same spots in the images before and after exposure (marked by blue arrows) the features become more indistinct during enzymatic attack. This could again be contributed to conglomeration of material on the tip (like in the EG1 reference experiment). The phase images provide no additional information about the alteration, they are too indefinite and are thus not shown here.

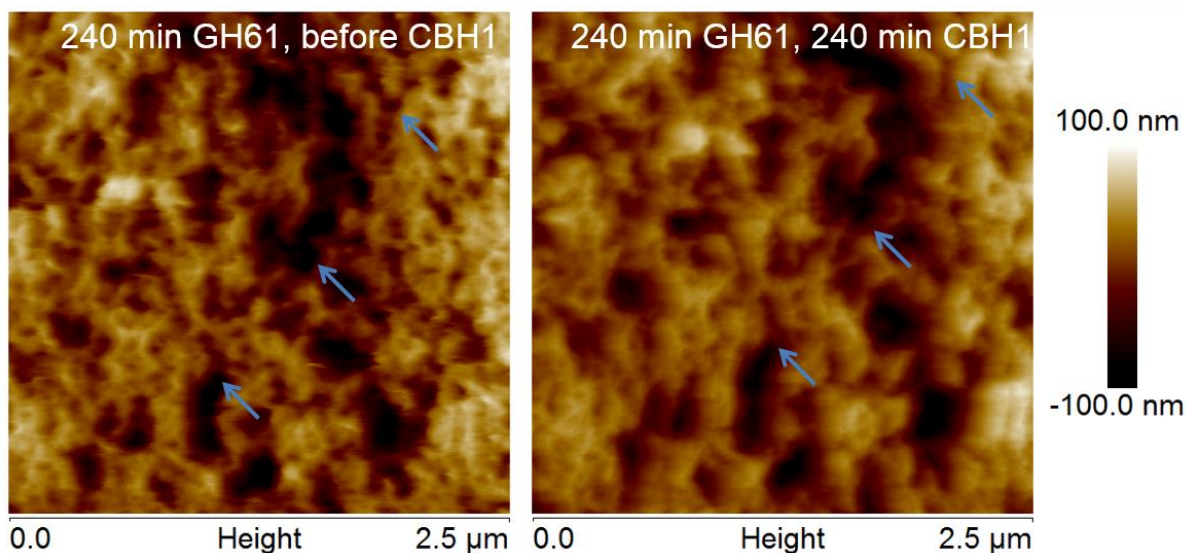


Fig. 47: Before (left) and after (right) CBH1 exposure 2.5  $\mu\text{m}$  height images of a FSEC2 sample. After 4 hours of GH61 CBH1 is applied for 4 hours. The blue arrows mark same spots.

Having a look at the surroundings of the areas of observation during enzymatic exposure gives insights into the influence of the tip on the FSEC2 sample. Fig. 48 shows 10  $\mu\text{m}$  height overview images of the used FSEC2 sample in this GH61/CBH1 experiment before exposure to GH61 and CBH1 and after a total of 8 hours of exposure. The areas of observation of the 2.5  $\mu\text{m}$  detail images that are taken consecutively over 8 hours are marked by blue frames. Comparing these areas to the surroundings shows that the widening of already existing gaps occurs predominantly in these regions. This strongly indicates tip influences on the smooth FSEC2 sample.

Moreover, these images represent the very smooth surfaces of the FSEC2 samples without the desired crystalline residues. This fact complicates the quantitative measurements of degradation, as mentioned in chapter 6.1.4.

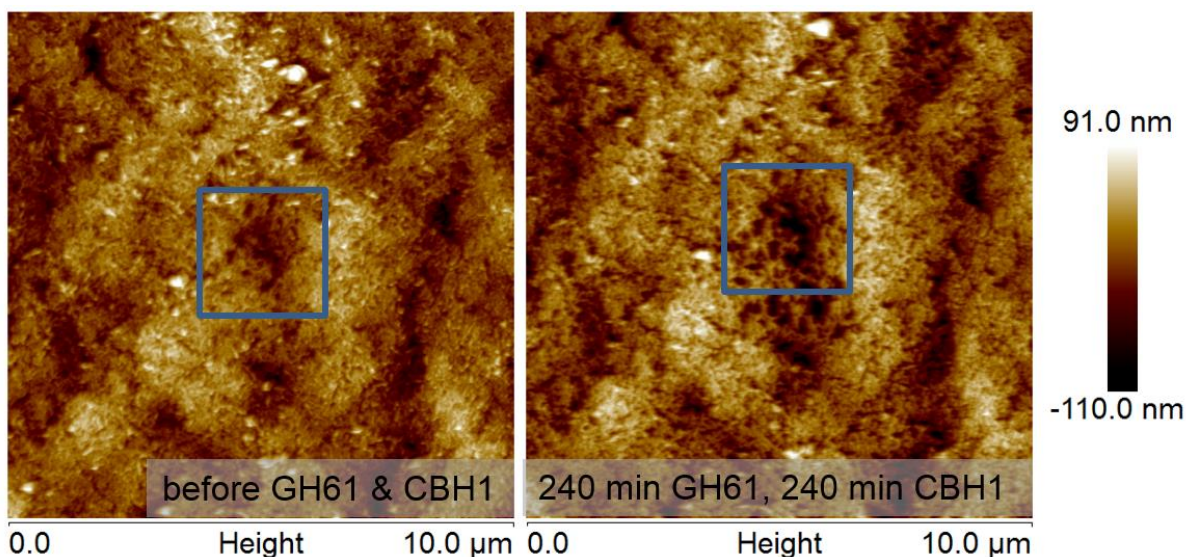
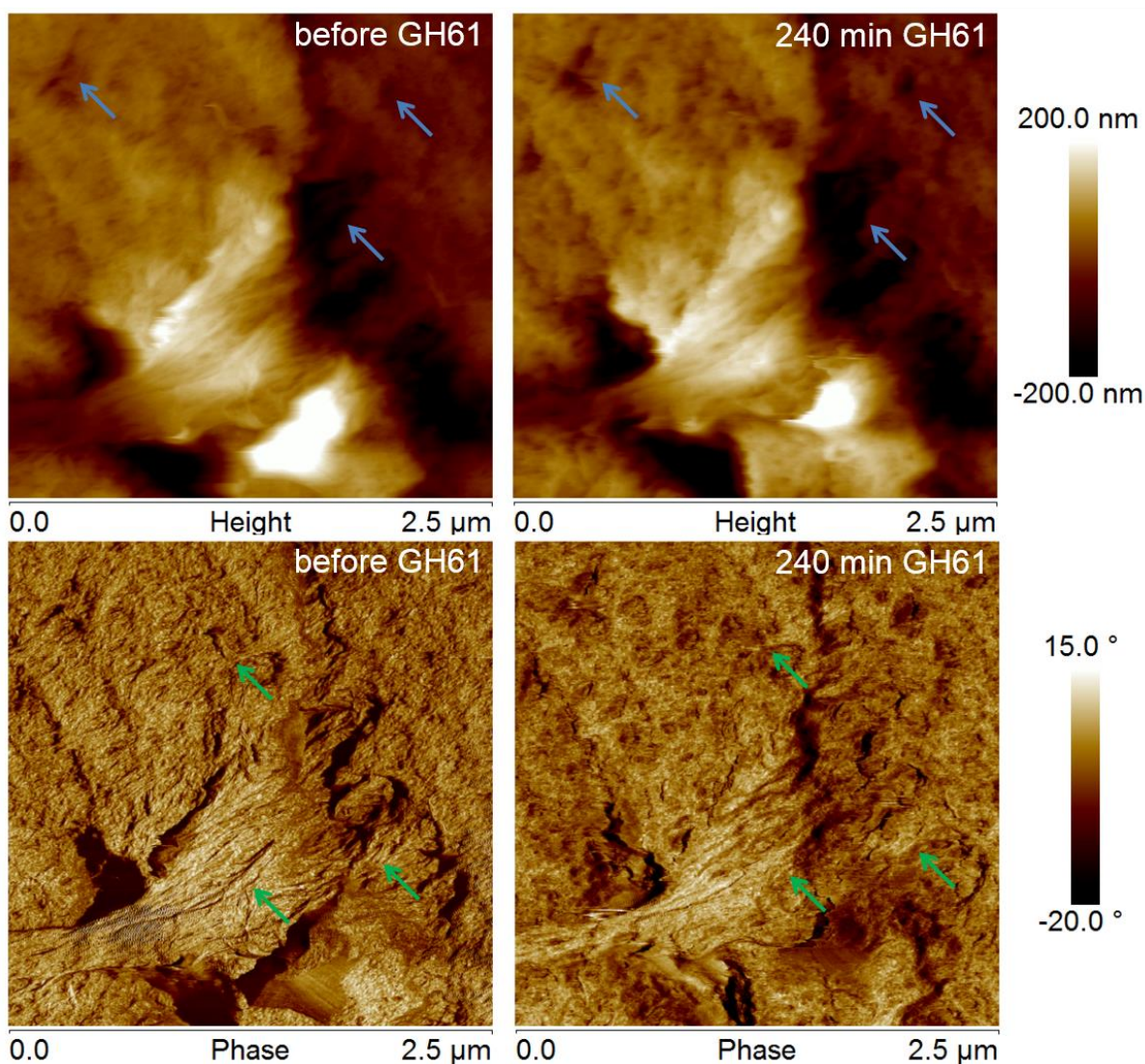


Fig. 48: Before (left) and after (right) exposure 10  $\mu\text{m}$  overview height images of a FSEC2 sample. GH61 and CBH1 are applied for 4 hours, respectively. The blue frames mark the area of the 2.5  $\mu\text{m}$  images that are taken consecutively during enzymatic exposure.

As no quantitative description of the effects of the GH61/CBH1 exposure can be obtained, an additional GH61/CBH1 experiment on another homogenous FSEC2 substrate is conducted. However, also this investigation yields similar results. Fig. 49 shows before-after 2.5  $\mu\text{m}$  height (upper row) and phase (bottom row) images of the GH61 exposure. GH61 seems to have a slight influence on this type of substrate again. A widening of already existing minor gaps can be recorded (marked by blue arrows) in the height images; certain crystalline fibres are affected as well (marked by the green arrows in the phase images in Fig. 49). Once more tip influence on the amorphous sample cannot be ignored. These circumstances are displayed in 10  $\mu\text{m}$  overview phase images in Fig. 51. The areas of observation of the 2.5  $\mu\text{m}$  detail images that are taken consecutively over 8 hours are marked by blue frames. As in the previous GH61/CBH1 experiment the widening of already existing gaps predominantly occurs in these regions. Again this indicates substantial tip influence on the FSEC2 sample.



**Fig. 49:** Before (left) and after (right) exposure 2.5  $\mu\text{m}$  height (top) and phase (bottom) images of a FSEC2 sample. GH61 is applied for 4 hours. Blue arrows in the height images indicate widening of already existing gaps. The green arrows in the phase images indicate crystalline features that are affected by GH61.

In this experiment degradation by CBH1 can be observed. Fig. 50 displays before-after 2.5  $\mu\text{m}$  height images of the exposure to CBH1. Blue arrows point to gaps that are widened by CBH1. As in the other (GH61)/CBH1 experiments conducted on FSEC2 samples, degradation of crystalline features cannot be observed directly. CBH1 rather attacks features that cannot be clearly seen on the amorphous FSEC2

surface. The alleged crystalline area (marked by a green circle in Fig. 50) is severely altered during CBH1 exposure; however, this cannot be explicitly attributed to enzymatic attack but also to tip influences (see also Fig. 51). Parts of the crystalline features are removed by the tip and probably conglomerate on the tip. This manifests in the image after 4 hours of CBH1 (right image in Fig. 50), where the overall surface has become more indistinct in comparison to the situation before CBH1 exposure. Despite all these aggravating circumstances, quantitative analysis of degradation can be conducted. The degradation velocity is estimated by  $v_d \approx 0.2$  nm/min, which is substantially lower than in the CBH1 reference experiment.

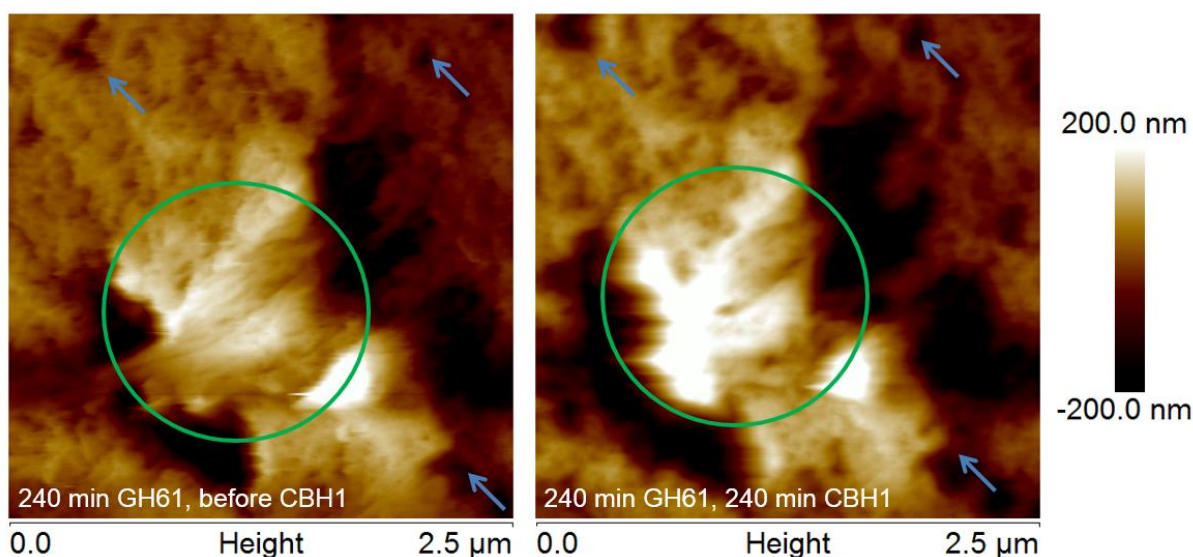


Fig. 50: Before (left) and after (right) CBH1 exposure 2.5  $\mu\text{m}$  height images of a FSEC2 sample. After 4 hours of GH61 CBH1 is applied for 4 hours. The blue arrows mark gaps that are widened during exposure to CBH1. The green circles indicate crystalline areas.

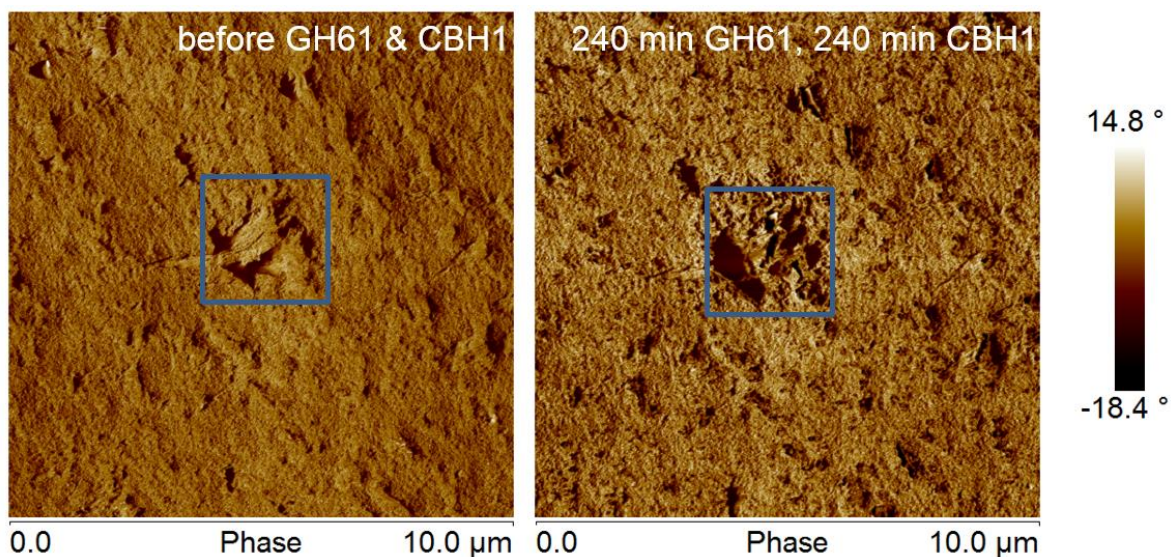


Fig. 51: Before (left) and after (right) exposure 10  $\mu\text{m}$  overview phase images of a FSEC2 sample. GH61 and CBH1 are applied for 4 hours, respectively. The blue frames mark the area of the 2.5  $\mu\text{m}$  images that are taken consecutively during enzymatic exposure.

Comparing these 2 GH61/CBH1 experiments to the CBH1 reference experiment give no clear insight into the effect of GH61 on CBH1. CBH1 is known to be active on crystalline features; generally, the FSEC2 samples used in the experiments show almost no crystalline areas attackable of CBH1 on the surface. In some cases, there have to be enough crystalline features accessible for CBH1 as degradation

of these very smooth samples can be recorded (see CBH1 reference experiment). Yet, the composition of the FSEC2 samples seems to vary from sample to sample, leading to unsatisfyingly incomparable results. Thus, the reproducibility of the FSEC2 samples has to be doubted. Moreover, the exposure to GH61 seems to soften the already amorphous samples even more. The influence of the AFM tip on these very smooth samples can also not be neglected. All these factors impede the activity of CBH1 in combination with GH61.

### 6.2.5 Summary GH61 experiments of FSEC1 and FSEC2

The experiments to investigate the influence of GH61 on the cellulases SVG, EG1, CBH2, and CBH1 are partly conducted on already well-tested FSEC1 samples and newly introduced FSEC2 samples. Additional Avicel flakes in the FSEC2 samples should ensure a variety of well-defined crystalline residues suitable for quantitative investigations of the degradation process. However, the new samples are very homogenous and highly amorphous with only very few crystalline structures. This makes it often difficult to find suitable markers on the surface which are used as reference for the quantitative measurements. Moreover, structure dependent analysis of degradation of crystalline and amorphous regions within the improved FSEC2 samples is not possible. These problems are faced especially in the case of the CBH1 experiments, as no clear results can be obtained. Nevertheless, the CBH1 experiments reveal, that the influence of the AFM tip on these smooth FSEC2 samples cannot be neglected and that GH61 seems to slightly affect this kind of samples. Widening of existing gaps can be observed in the height images as well as alterations of crystalline structures in the phase images. To some extent these effects can be attributed to the influence of the tip on the smooth FSEC2 samples. On the contrary, neither influences of GH61 nor of the tip can be detected during GH61 exposure, when applying it to FSEC1 samples, neither in the height nor in the phase images.

The GH61-cellulase and cellulase reference experiments with SVG, CBH2, and EG1 verify the expected behaviour, that GH61 boosts the activity of the mentioned cellulases [16, 17, 18, 19]. These boosts in activity are reflected in an increase of the degradation velocity when compared to those, where the samples are exposed to SVG, CBH2, and EG1 only. These results are shown in Table 4 and Fig. 52.

**Table 4: Comparison of degradation velocities  $v_d$  in the GH61-cellulase and cellulase reference experiments.**

| sample | enzyme    | $v_d$ (nm/min) |
|--------|-----------|----------------|
| FSEC1  | SVG       | $0.8 \pm 0.3$  |
| FSEC1  | GH61/SVG  | $1.4 \pm 0.2$  |
| FSEC2  | EG1       | $0.4 \pm 0.2$  |
| FSEC1  | GH61/EG1  | $0.5 \pm 0.1$  |
| FSEC2  | CBH2      | $0.6 \pm 0.2$  |
| FSEC2  | GH61/CBH2 | $1.3 \pm 0.2$  |

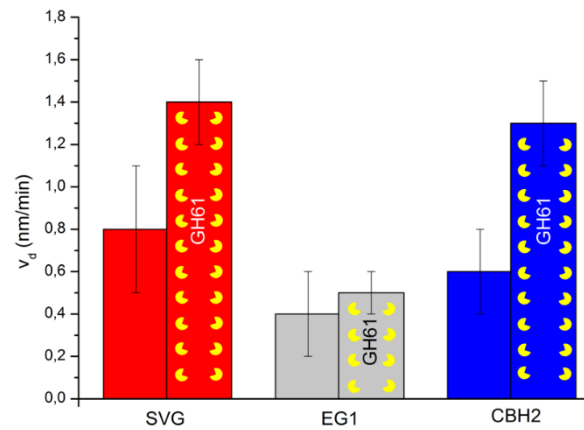


**Fig. 52:** Bar graph of the degradation velocities  $v_d$  of the supernatant SVG and the cellulases EG1 and CBH2 in comparison to the degradation velocities of the cellulases with prior exposure to GH61 (marked in yellow).

Even though it turned out, that the newly introduced FSEC2 samples are not suitable for quantitative purposes, the samples reveal that GH61 has a slight effect on very amorphous substrates. Subsequently, this induces tip influences on the sample, which aggravate the analysis of degradation in respect to quantitative estimations and structural changes. All these factors substantiate the need for reliable, reproducible samples that are suitable for detailed examination of the degradation process. Therefore, spin cast cellulose (SCC) samples are introduced and intensively tested in the following chapter.

## 6.3 Spin cast cellulose

Spin cast cellulose (SCC) provides highly reproducible [38] samples. Their production is less time-consuming and they can thus be perfectly used for testing tasks. To guarantee comparability to the experiments performed with FSEC samples and to reproduce natural circumstances optimally, the spin cast specimens must show both amorphous and crystalline properties. The amorphous structure is represented by trimethylsilyl cellulose (TMSC), whereas the crystalline features can be formed by nanocrystalline cellulose (NCC). The spin cast method offers the possibility to produce tunable substrates, since the film thickness of the amorphous matrix can be easily controlled by adjusting the solution's concentration and the spinning velocity. In the following sections both the amorphous and the crystalline specimens are examined in detail.

The characterization of TMSC includes XRD, Raman spectroscopy, LIM1, and AFM measurements. AFM measurements allow not only insights in the morphology in dependence on the preparation parameters but also in the thickness of the layers. Enzymatic degradation of TMSC is studied in detail by AFM by exposing the sample to SVG and CBH2.

The investigation of NCC consists of Raman spectroscopy, SEM, EDX, TEM, and AFM measurements. Conducted on NCC the AFM measurements reveal the morphology of the specimen and the enzymatic degradation by SVG and CBH1 is examined.

Combining the TMSC and NCC samples leads to a new promising type of cellulose samples which is tested in degradation experiments with SVG and CBH1/CBH2.

### 6.3.1 TMSC

#### 6.3.1.1 XRD of TMSC

The purpose of the XRD measurements is to prove that the TMSC samples mainly consist of amorphous cellulose. Since the usually used TMSC samples have a layer thickness of only 20 nm to 80 nm in dry environments and are thus easily passed by the X-rays without any interaction a TMSC sample with multiple spin casted layers is used. Fig. 53 depicts the XRD spectra of this layered TMSC sample (drawn in red). Spectra of purely crystalline Avicel (black) and of a rather amorphous FSEC sample (drawn in blue, Avicel content 4 %) serve as references. The curves are FFT smoothed (15 points) and normalized to the maximum peak. The main peak of TMSC is broadened and shifted to lower angles ( $2\theta = 20.1^\circ$  in comparison to  $2\theta = 22.7^\circ$  for Avicel). This indicates that the sample predominantly contains amorphous cellulose in contrast to the FSEC sample with its crystalline features (see also Fig. 29 in chapter 6.1.2 for XRD of FSEC samples).

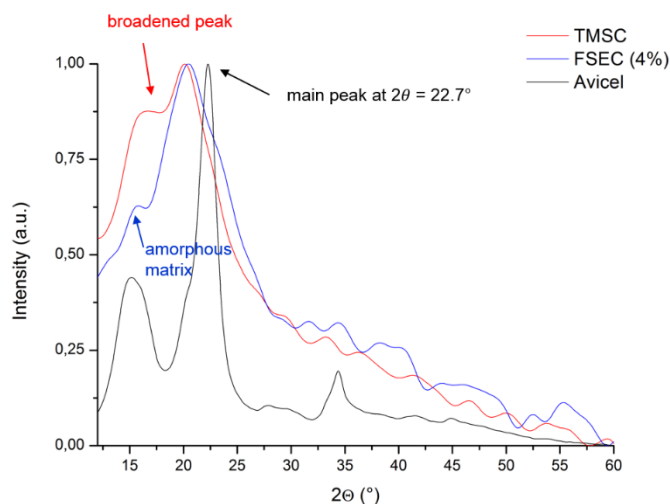


**Fig. 53:** XRD spectra of a TMSC (red) and a FSEC (blue) sample with the crystalline reference spectrum of Avicel (black).

### 6.3.1.2 Raman spectroscopy of TMSC

Raman spectroscopy of a TMSC sample is conducted to confirm the amorphous structure of the TMSC samples. In Fig. 54 Raman spectra of crystalline cellulose [39] and TMSC are compared. The curves are FFT smoothed (3 points) and normalized. The blue circles highlight the frequency ranges where the differences between crystalline and amorphous cellulose can easily be seen. The Raman lines of TMSC in the region of  $1000 - 800 \text{ cm}^{-1}$  and  $600 - 300 \text{ cm}^{-1}$  differ strongly from the crystalline reference spectrum indicating amorphous cellulose according to Schenzel et al. [28].

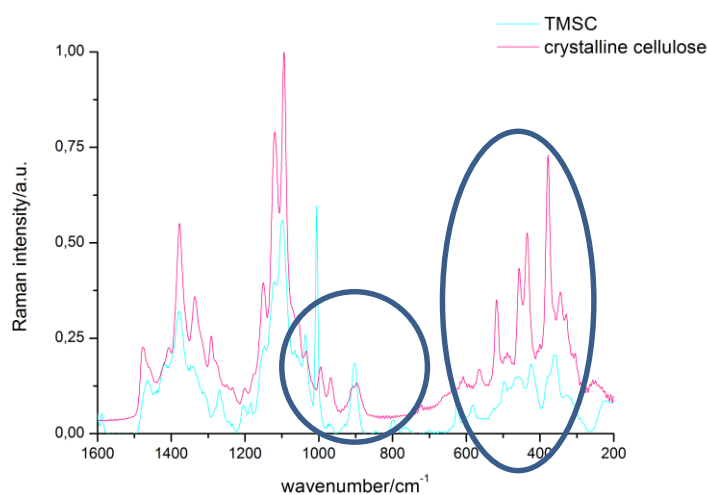


**Fig. 54:** Raman spectra of crystalline cellulose (pink) [39] and TMSC (cyan).

### 6.3.1.3 Thickness estimation of TMSC via LIM1

After the preparation of the TMSC films the colour of the films can be a qualitative indicator of the film thickness: films resulting from solutions of higher concentration (10 g/l, especially 15 g/l TMSC in Xylol) show an increasing tendency to blue surfaces. These results come from the effect of thin-film interference.

Similarly, one can distinguish between the different concentrations of the samples by the colour of the films by examining the different TMSC samples by light microscopy (LIMI). This gives a quick hint of the film thickness. Fig. 55 shows light microscopic images of three samples (concentrations: 5 g/l, 10 g/l, 15 g/l TMSC in Xylol; spinning speed: 5300 rpm), which are representative for the all other samples. The differences in the spinning speed cannot be seen via LIMI; however, the colour of the film represents the concentration: rather transparent for 5 g/l, dark yellow/orange for 10 g/l, and dark blue/brown for 15 g/l TMSC in Xylol.

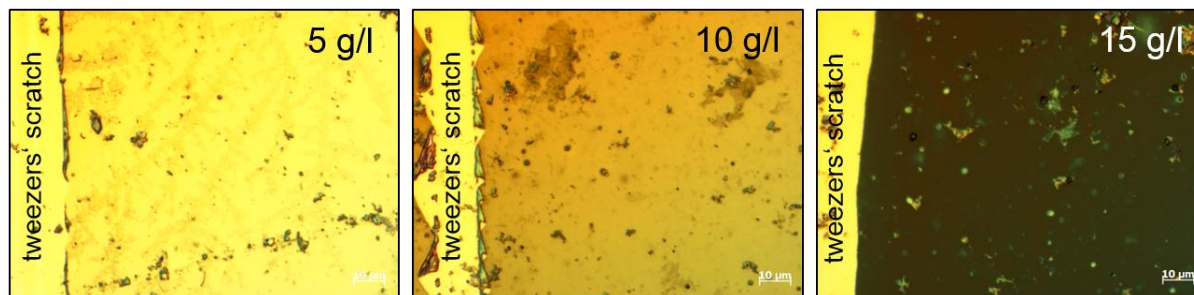


Fig. 55: Light microscopy images of 3 different TMSC samples with different concentrations of TMSC in Xylol. The samples are scratched with tweezers on the left. The scale bar is 10  $\mu\text{m}$ .

### 6.3.1.4 AFM of TMSC

#### Morphology depending on preparation parameters in dry and liquid environments

Detailed 1  $\mu\text{m}$  AFM images of the TMSC samples with differing preparation parameters (concentration of TMSC in Xylol: 5, 10, 15 g/l; spin rates: 4300, 5300, 6300 rpm) are taken and compared. The samples are extremely smooth with  $R_q$  values between 0.6 nm and 2 nm! No correlation between roughness and concentration/spin rate can be found. Fig. 56 represents the TMSC sample with highest resolution in dry environments; 1  $\mu\text{m}$  height and phase images of the sample with a TMSC concentration of 15 g/l and a spin rate of 6300 rpm are displayed. The morphologies of the other samples are similar. The rather high resolution of the image allows the analysis of the relation between the edges in the phase image and the height profile of the sample. Interesting results can be obtained by superimposing the height and phase profiles at certain spots. Fig. 57 shows the phase (top) and height (bottom) profiles at the positions of the red bars in Fig. 56. The blue boxes indicate congruence of the height and phase signals which suggest internal crystalline features in the TMSC samples. This congruence does not occur all over the sample, only certain spots of congruence can be found. The appearance of these vague crystalline parts could be attributed to incomplete dissolution of TMSC in the solvent or to the reformation of cellulose II crystals. Nevertheless, the samples are extremely flat and the amorphous, unordered character predominates.

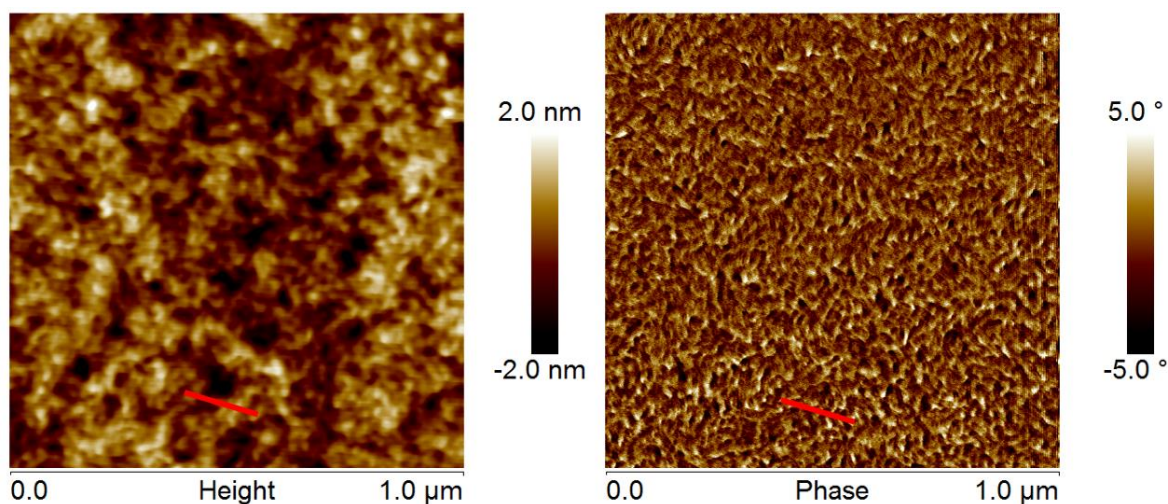


Fig. 56: 1  $\mu\text{m}$  height and phase AFM images of a TMSC sample (15 g/l, 6300 rpm) representing the morphology of the TMSC samples in dry environments. The red bar marks the region for the profiles in Fig. 57.

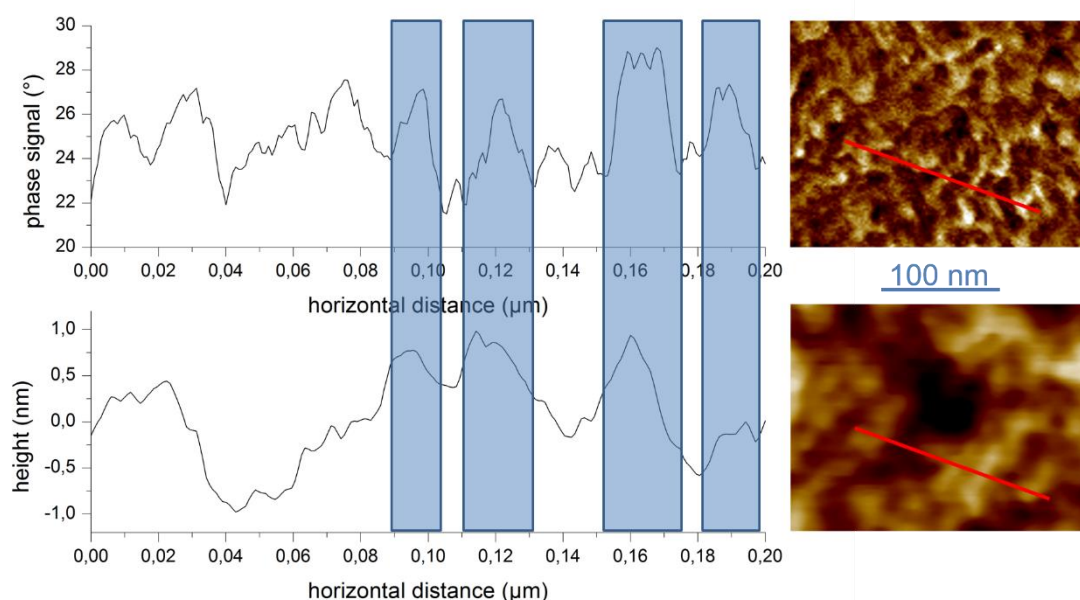
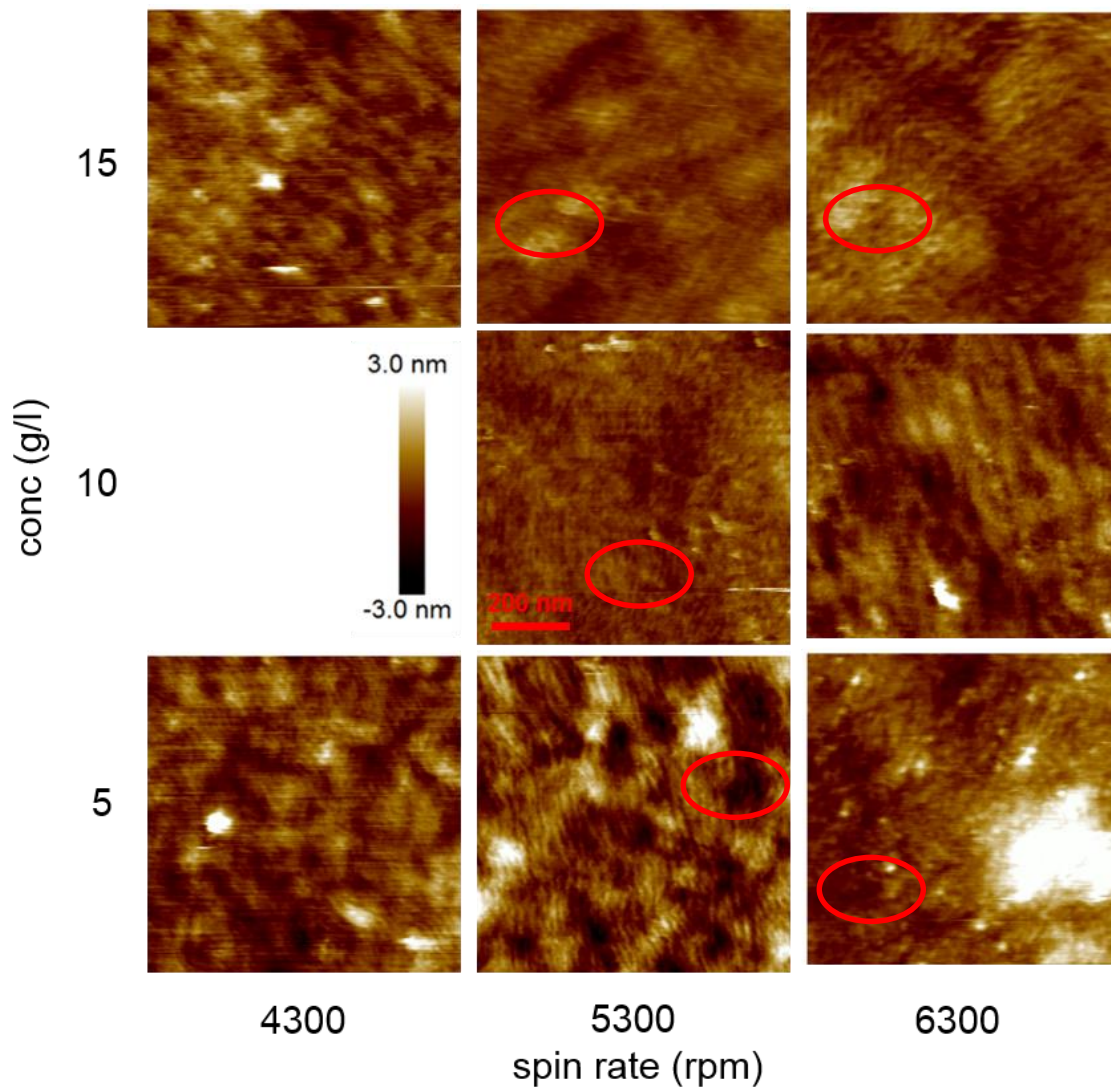


Fig. 57: Left: Phase (top) and height (bottom) profiles taken at the position marked by the red bar in the detail phase (top) and height (bottom) images on the right (also in Fig. 56). The blue boxes in the profiles indicate probable crystalline features. The scale bar for the phase and height images is 100 nm.

The analysis is repeated with the samples immersed in liquid (distilled water). Collections of height and phase images of the samples with varying preparation parameters are displayed in Fig. 58 and Fig. 59. Severe influence of the preparation parameters on the morphology of the samples cannot be detected. Due to the swelling the surfaces are even smoother than in dry environments, the  $R_q$  values lie between 0.4 and 1 nm. This fact indicates vertical swelling; it can be substantiated by comparing the sizes of the cellulose structures, which globally stay the same. Also in liquid environments congruence of the height (marked by red circles in Fig. 58) and phase (marked by red circles in Fig. 59) signals can be found at certain positions, once more that refers to the embedding of vague crystalline features. However, conglomeration of material on the tip cannot be excluded as periodic patterns occur in both the height and phase images.



**Fig. 58:** Collection of height images of TMSC samples with varying preparation parameters (spin rate and concentration). Regions with assumed higher crystallinity are marked by red circles.

Apart from these artefacts no grave differences in the structure due to varying preparation parameters can be detected, neither in height nor in phase images. In liquid environments the amorphous character of TMSC dominates as well. Moreover, the resolution is significantly increased in liquid environment as it has already been reported by T. Aschl [4]. The amazing resolution in liquid can be seen in Fig. 60, which displays a  $100 \times 100$  nm 3D height detail of the representative TMSC (15 g/l, 6300 rpm) sample. This image emphasizes the flatness of the TMSC samples,  $R_q$  values that average around 1 nm have never been realized with the FSEC samples due to the rather abrasive ultramicrotomy treatment.

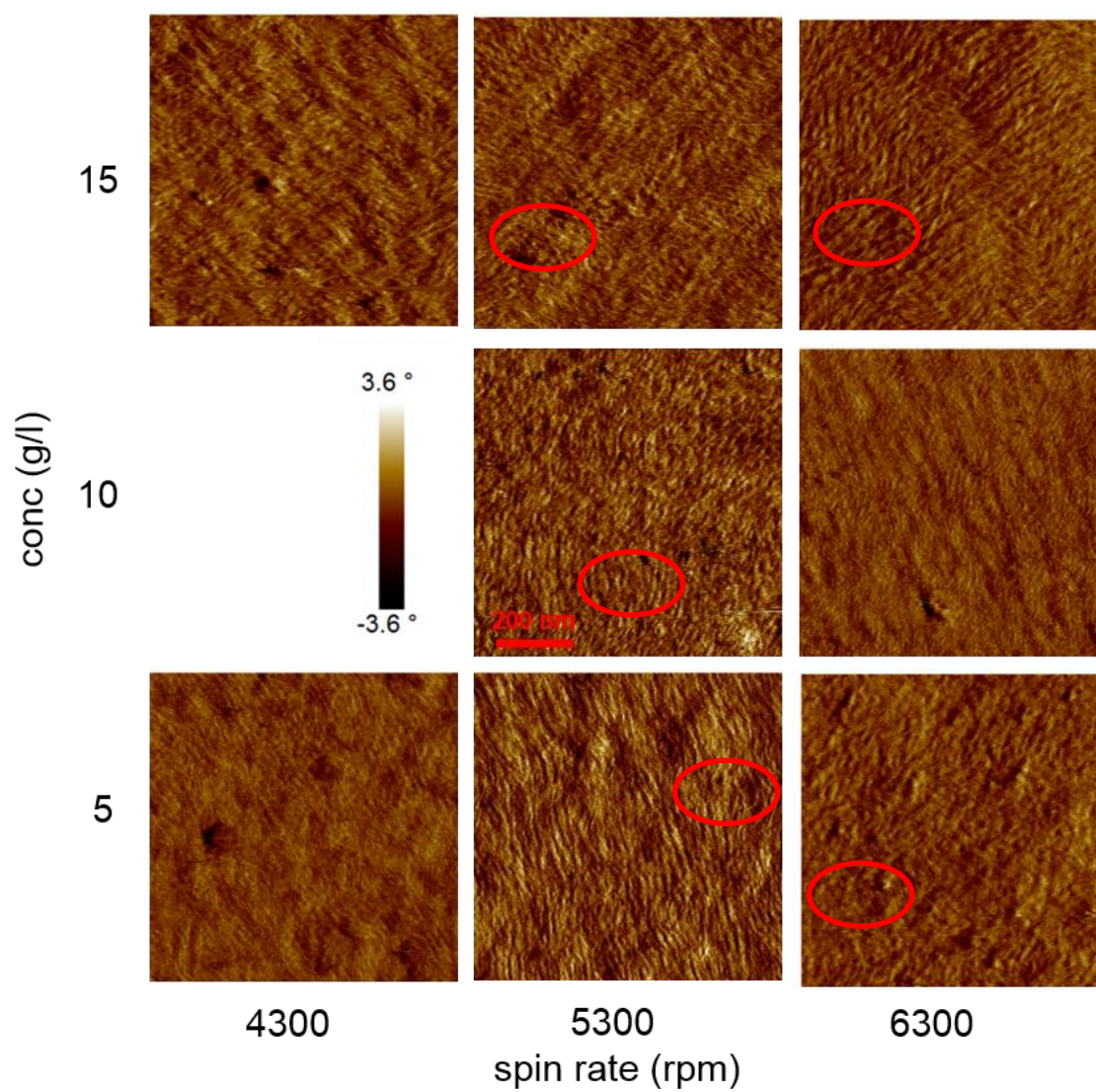
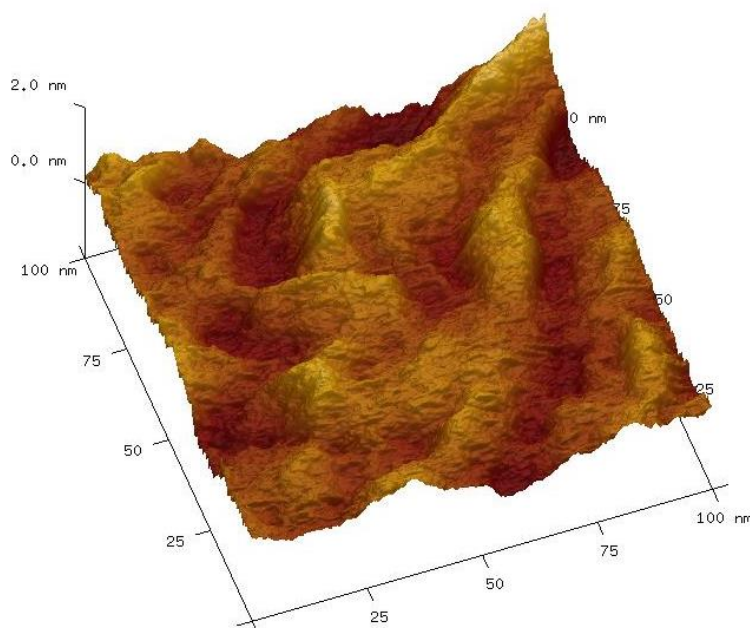


Fig. 59: Collection of phase images of TMSC samples with varying preparation parameters (spin rate and concentration). Regions with assumed higher crystallinity are marked by red circles.



**Fig. 60:** 100 nm 3D height detail of a TMSC sample (15 g/l, 6300 rpm).

### Layer thickness depending on the preparation parameters in dry and liquid environments

As mentioned before the preparation parameters for the TMSC samples are the concentration of TMSC in the solvent and the spinning speeds. By adjusting these parameters it should be possible to obtain tunable samples, as the layer thickness is of particular interest for the amorphous TMSC. Thus the layer thicknesses of the resulting samples are analysed by AFM both in dry and liquid environments. Fig. 61 shows the layer thickness as a function of the spin rate and the dependency on the TMSC concentration (black, red, blue) in dry (left) and liquid (right) environments. The spin rate has a rather low influence on the thickness of the layers; it can thus be neglected. The parameter responsible for tuning the TMSC samples is the concentration of the TMSC in the solvent. The average layer thicknesses are represented by coloured lines. These mean values of layer thickness are presented in Table 5. The swelling of the layer in liquid can be estimated by a factor of 2. Fig. 62 displays the TMSC layer thickness as a function of the concentration of TMSC in Xylol with first-order fits in dry (red) and liquid (blue) environments. Varying the concentration of TMSC in the solvent offers control over the layer properties, the thickness of the cellulose films can thus be adjusted precisely.

**Table 5:** Mean thickness  $d$  of TMSC layers in dry and liquid environments depending on the TMSC concentration  $c$ .

| $c/(g/l)$ | $d_{dry}/nm$ | $d_{liquid}/nm$ |
|-----------|--------------|-----------------|
| 5         | $20 \pm 1$   | $40 \pm 5$      |
| 10        | $50 \pm 5$   | $100 \pm 8$     |
| 15        | $80 \pm 13$  | $180 \pm 30$    |

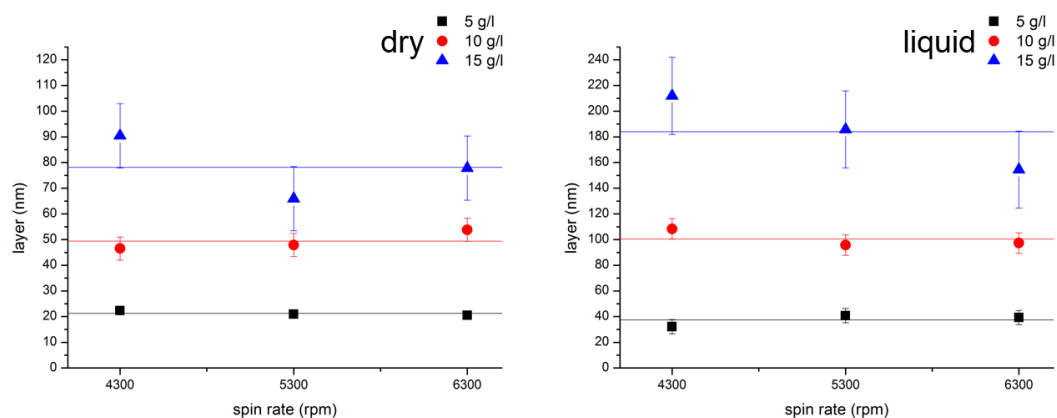


**Fig. 61:** Layer thickness as a function of the spin rate (x-axis) and dependency on TMSC concentration (black, red, blue) in dry (left) and liquid (right) environments. The coloured lines represent the mean value of the layer thickness. Note the y-axis scale which emphasizes the swelling of the layers in liquid estimated by a factor of 2.

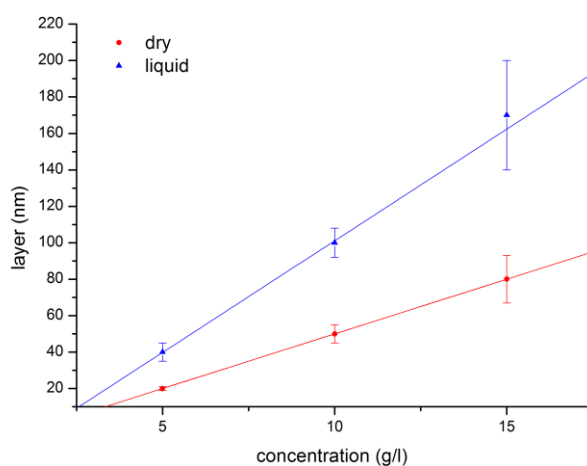


**Fig. 62:** TMSC layer thickness as a function of the concentration of TMSC in Xylol with first-order fits in dry (red) and liquid (blue) environments.

### 6.3.1.5 Enzymatic degradation experiments on TMSC

The TMSC samples are tested for their suitability in enzymatic degradation experiments. Therefore, the TMSC samples are exposed to the supernatant, which is known for its high activity due to synergistic effects, and to CBH2, which represents a single cellulase capable of attacking both amorphous and crystalline regions [15].

#### SVG on TMSC

As a proof of concept a TMSC sample is exposed to the SVG supernatant to see if degradation can be observed. The sample is scratched with tweezers to allow the wafer surface to be used as a reference plane. Fig. 63 displays before-after 10  $\mu\text{m}$  height images of the exposure to SVG. Due to the enzymatic attack a multitude of gaps appears (marked by blue arrows) and the  $R_q$  value increases from 3.4 nm to 5.1 nm; these effects both indicate (minor) degradation. The low activity of the supernatant can be explained by the rather low enzyme concentration (see Table 3 on page 22) used in this experiment. Still, interesting observations of the degradation process can be obtained. The cellulose surface is not

attacked along the edge, but at already existing gaps, as it has been reported previously by J. Dohr [2] and Bubner et al. [40]. The widely amorphous structure of the TMSC samples becomes apparent in this AFM experiment as there is no sign of crystalline features which are excavated during exposure to SVG. All these findings suggest the suitability of TMSC as amorphous cellulose sample. In the next step a single cellulase is applied on TMSC to study its behaviour.

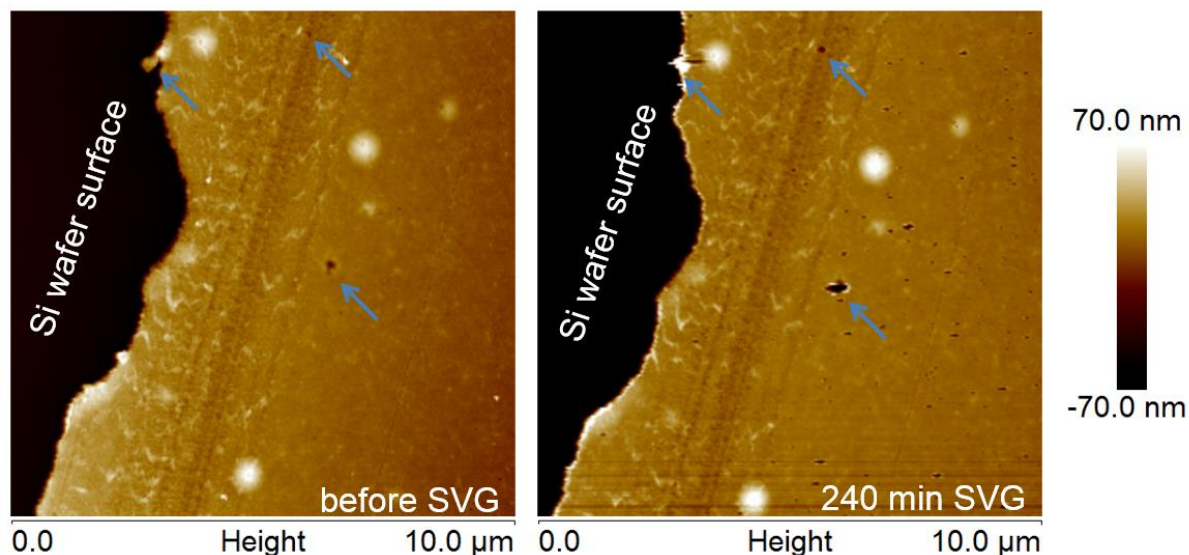


Fig. 63: Before (left) and after (right) exposure 10  $\mu\text{m}$  height images of a TMSC sample. SVG is applied for 4 hours. The blue arrows mark features where degradation is visible. The left dark part displays the Si wafer surface.

### CBH2 on TMSC

A TMSC sample is exposed to CBH2, the exo-glucanase with reported endo-glucanase properties [15]. Hence CBH2 is expected to attack the widely amorphous cellulose film and probable excavated crystalline features as well.

The enzymatic concentration is again rather low; thus the activity of CBH2 on the amorphous sample is little, yet degradation is recognizable. Fig. 64 shows 5  $\mu\text{m}$  height images before (left) and after 2.5 hours of exposure (right) to CBH2. As in the SVG experiment, already existing gaps are widened during enzymatic attack and no crystalline features are excavated. Also this experiment suggests the amorphous properties of TMSC.

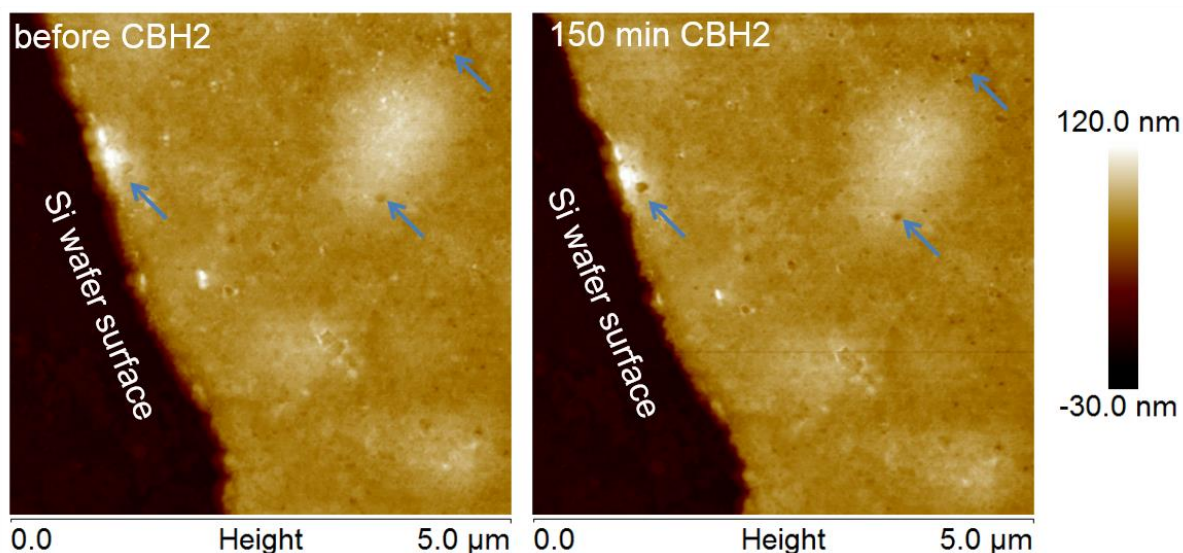


Fig. 64: Before (left) and after (right) exposure 5  $\mu\text{m}$  height images of a TMSC sample. CBH2 is applied for 2.5 hours. The blue arrows mark features where degradation is visible. The left dark part displays the Si wafer surface.

The enzymatic degradation experiments conducted on TMSC samples show that degradation is observable. The exposure to SVG and CBH2 both confirm the amorphous characteristics of TMSC as no crystalline features are excavated. The embedding of vague crystalline fibres in the amorphous matrix that is assumed in the AFM morphology investigations in section 6.3.1.4 cannot be visualized in these experiments that are conducted on large scales to obtain an overview of the enzymatic attack on TMSC. Still, the results of the SVG and CBH2 experiments show that the amorphous TMSC substrate is suitable for enzymatic degradation investigations! The next step is to find a substrate that represents the crystalline features in the cellulose samples. Thus, nano-crystalline cellulose is intensively tested in the next chapter.

## 6.3.2 NCC

The proved and tested FSEC samples contain crystalline residues which are embedded in the amorphous cellulose matrix and consist of cellulose I. The need for representing the crystalline properties also with the spin cast cellulose leads to the introduction of nano-crystalline cellulose (NCC). The preparation procedure is described in chapter 4.5. In this section the NCC samples are examined by Raman spectroscopy, SEM, EDX and TEM. The main focus is placed on AFM measurements.

### 6.3.2.1 Raman spectroscopy of NCC

The preparation of NCC according to Edgar et al. [37] leads to cellulose I crystals. Fig. 65 depicts the spectra of crystalline cellulose I (pink) and NCC (cyan) which are FFT smoothed (3 points) and normalized. The Raman spectrum of NCC is in very good accordance with the crystalline reference spectrum [39] and its characteristic peaks [28, 29]. This confirms the highly crystalline structure of NCC.

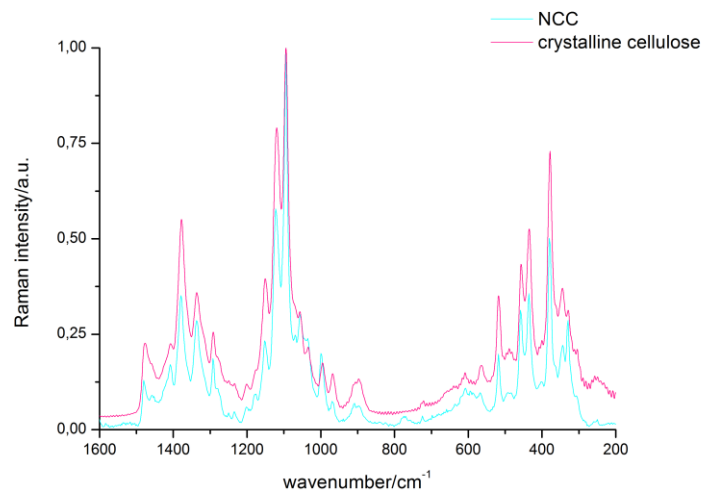


Fig. 65: Raman spectra comparing crystalline cellulose (pink) [39] to NCC (cyan).

### 6.3.2.2 SEM and TEM of NCC

SEM and TEM investigations of NCC give first insights into the well-defined structures and dimensions of NCC. Fig. 66 depicts SEM images of the NCC samples at different stages of preparation. The left image shows the highly concentrated NCC gel where the fibres are packed closely together. In the right image single crystalline fibres (approx. 200 nm × 30 nm) that can be found in the filtered clear solution (see chapter 4.5 for the preparation of NCC) are illustrated. During the SEM examinations EDX measurements were conducted that showed the elemental composition of NCC (carbon and oxygen) with minor residues of sulphur that derive from the preparation process.

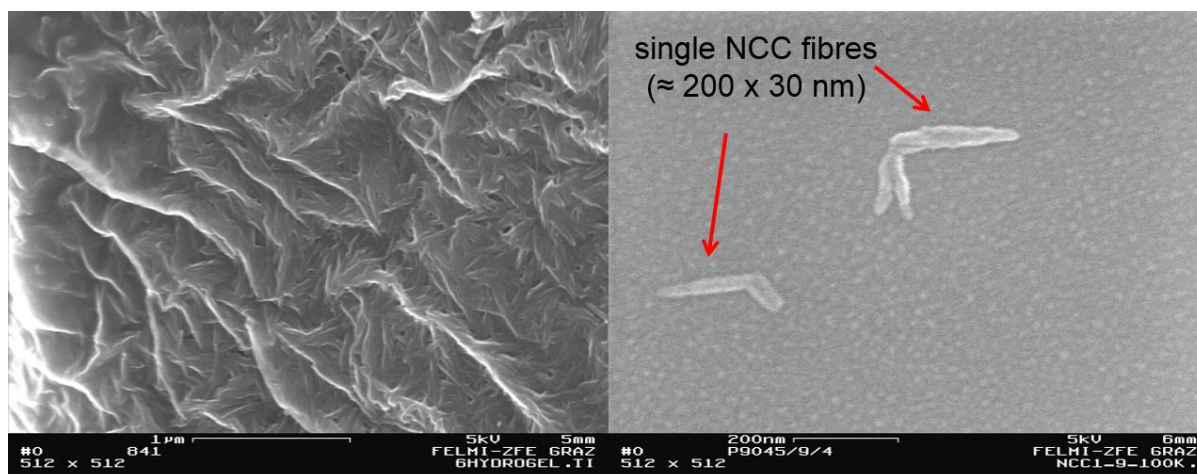


Fig. 66: SEM images of the highly concentrated NCC gel (left) and single fibres (right) from the filtered clear solution with dimensions of approx. 200 nm x 30 nm.

For TEM examinations a NCC sample is stained (for 2 min, 2 wt. % Uranyl acetate in H<sub>2</sub>O) on a carbon film that serves as carrier material. Fig. 67 shows the crystalline nano-whiskers. Single fibres and several packs of fibres are displayed. The long drawn-out, needle-shaped fibres vary in length, groups of shorter ( $\approx 100$  nm) and longer fibres ( $\approx 200$  nm) can be found. The widths of the fibres largely range from 20 nm to 40 nm. A detailed analysis of the properties of NCC is conducted by AFM in the next section.

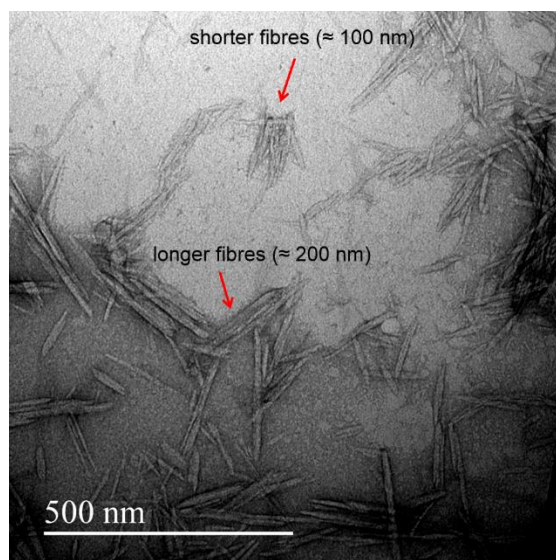


Fig. 67: TEM image of NCC that reveals the shape of single NCC fibres.

### 6.3.2.3 AFM of pre-filtered spin coated NCC in dry environments

The first spin casting test with pre-filtered NCC is examined by AFM in tapping mode. The NCC solution is spin coated on a silicon wafer with a spinning speed of 4300 rpm for 1 min. In contrast to Edgar et al., who produced films covering the whole wafer [37], here only a very little amount stays on the wafer due to the high surface tension of the NCC solution. Still, the surfaces of NCC are very flat; the  $R_q$  values lie slightly below 10 nm. Fig. 68 shows AFM height images of the pre-filtered sample. Like in the SEM and TEM images (see section 6.3.2.2) crystalline features with different lengths can be seen, they range from 50 nm to 200 nm, the bigger part of features lies between 100 nm and 200 nm. Note the rather elliptical shape of the smaller features (marked by red arrows). Here the limits of lateral resolution in AFM are reached due to the convolution of the AFM tip as the pointed tips visible in the SEM (Fig. 66) and TEM (Fig. 67) images cannot be resolved.

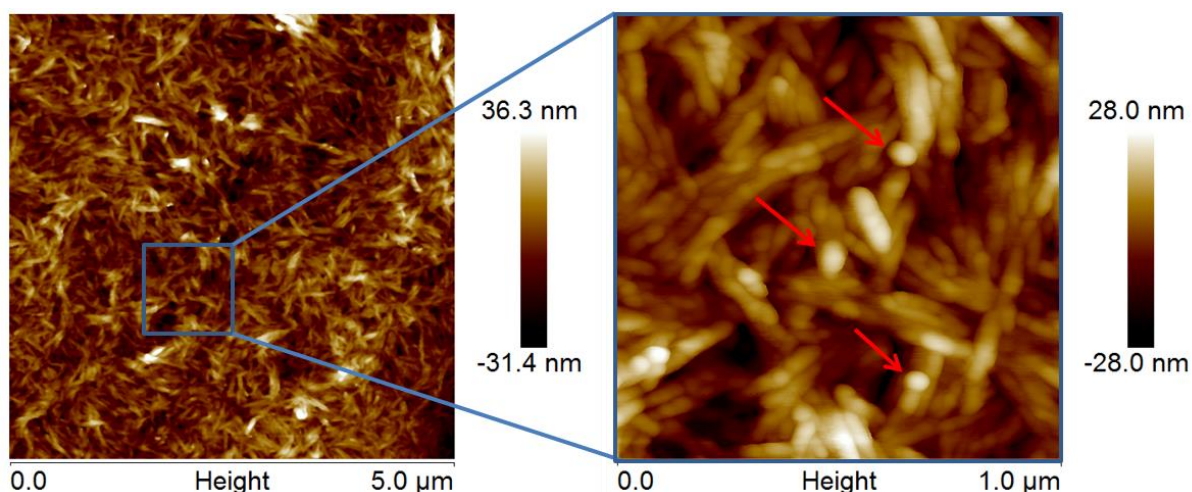
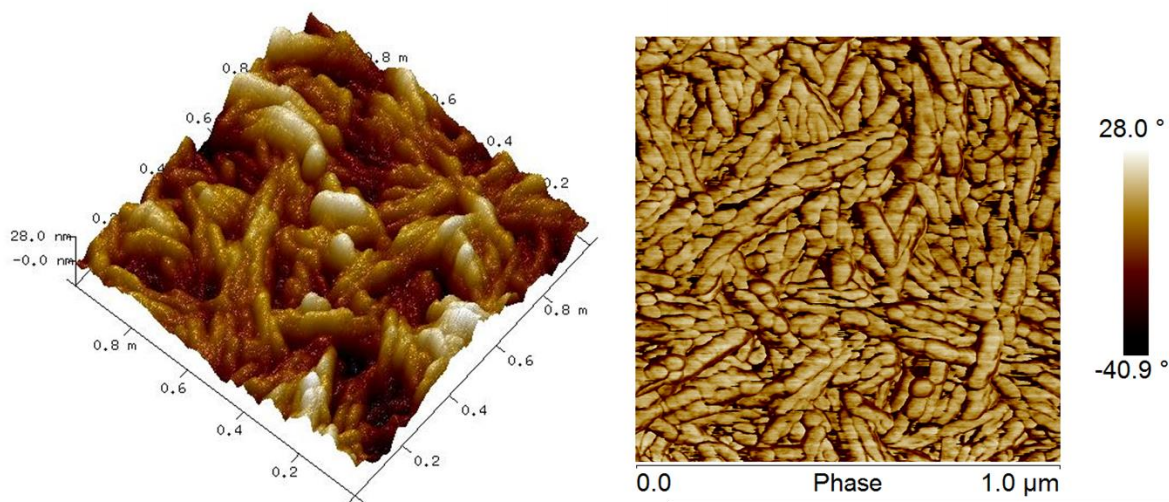


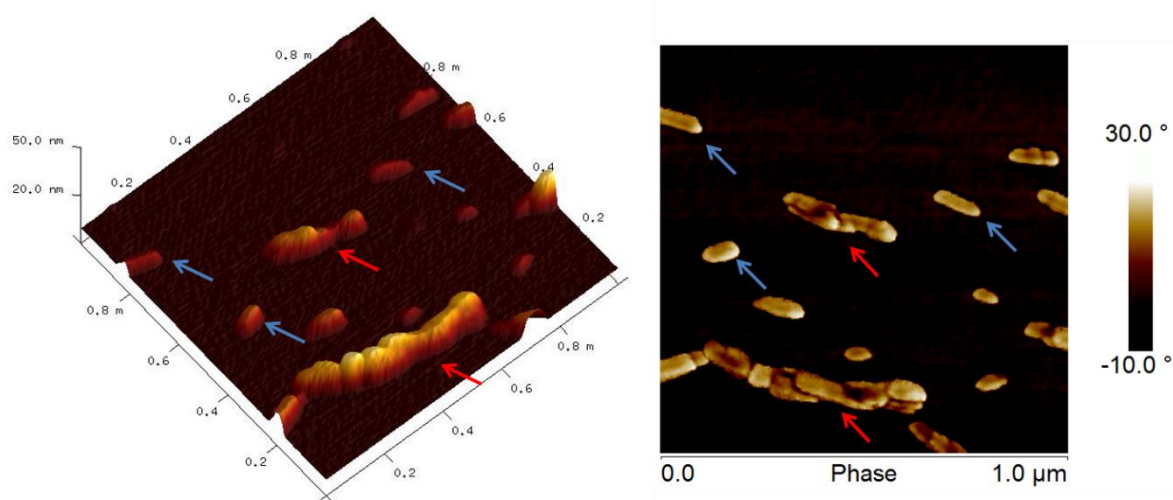
Fig. 68: AFM height images of the pre-filtered NCC sample. Smaller features ( $< 50$  nm) are marked by red arrows in the 1 μm image (right).

Fig. 69 illustrates a 3D (left) and the phase image (right) of the 1  $\mu\text{m}$  detail in Fig. 68. The nano-whiskers are clearly visible. Comparing the phase image (right) to the height image in Fig. 68 reveals the crystalline structure of NCC also in AFM (previously tested by Raman spectroscopy in section 6.3.2.1) as the phase edges can be unmistakably assigned to the variations in height.



**Fig. 69:** 3D height (left) and phase image (right) of the 1  $\mu\text{m}$  detail of the pre-filtered NCC sample in Fig. 68.

Fig. 70 depicts a 3D (left) and the corresponding phase image (right) of NCC fibres on a Si wafer that were separated by ultrasonic treatments. The varying height profiles of the fibres in the 3D height images suggest that features significantly longer than 200 nm (marked by red arrows) consist of piled fibres. This piling could also explain the phase variations along the features in the phase images (red arrows). Single features (marked by blue arrows in Fig. 70) show lengths between 60 nm and 130 nm and smooth height profiles, thus no variations in the phase signals can be detected. The heights of the single features ranges from 5 nm to 10 nm. By reason of these low values the convolution artefacts of the tip have to be considered and values for the width of the fibres (ranging from 45 nm to 60 nm) cannot regarded to be reliable. This also manifests in the elliptical shapes of smaller features and the blunt ends of the longer features. In the SEM (Fig. 66) and TEM (Fig. 67) images in section 6.3.2.2 the fibres clearly show pointed ends. Nevertheless, NCC represents very well-defined purely crystalline features which will be tested for their suitability in enzymatic degradation experiments in the following section.



**Fig. 70:** 3D height (left) and phase image (right) of NCC fibres in dry environments. Blue arrows mark single features. Red arrows indicate piled features.

### 6.3.2.4 Enzymatic degradation experiments on NCC

Like for the amorphous TMSC samples the enzymatic degradation experiments conducted on NCC should serve as a proof of concept of this type of substrate. For these investigations the highly-concentrated NCC gel is dissolved in isopropanol. This solution is treated 3 times with a sonicator for 30 seconds, respectively, to get a homogenous distribution of NCC in the solution; in between the sonication cycles the solution is water-cooled. The solution is spin coated on silicon wafers right after these preparation steps (spinning speed: 4300 rpm for 1 min).

The crystalline structure of NCC has been confirmed by Raman spectroscopy, SEM, TEM and AFM investigations. Therefore NCC is exposed to CBH1, which is known to be active on crystalline cellulose. The second enzymatic degradation experiment of NCC is conducted with SVG to see the influences of the enzymatic mixture on the purely crystalline substrate.

#### CBH1 on NCC

As for the TMSC samples this experiment serves as proof of concept for enzymatic degradation experiments conducted on the new NCC samples. The NCC sample is placed in the liquid cell filled with buffer solution and continuously observed for 4 hours during exposure to CBH1, which degrades crystalline cellulose. For observing the potential degradation of the NCC film, images along the edge of the film are taken, so that the silicon wafer can be used as a fixed reference area, as the silicon substrate is not affected by the enzymes. Before-after 2.5  $\mu\text{m}$  height (top) and phase (bottom) images can be seen in Fig. 71. Height degradation and roughness analysis shows, that the crystallites are just slightly affected by the enzymes, a mean degradation velocity of  $v_{d,CBH1} = 0.1 \text{ nm/min}$  can be measured. The  $R_q$  value stays rather stable during the course of the experiment,  $R_q = 61.2 \pm 3.3 \text{ nm}$ . This indicates that the degradation is indeed very small. The minor differences are also substantiated by the phase images, where the crystalline features that are only slightly affected are marked by blue arrows. Alterations of features at the edge can be attributed to tip influences. The recalcitrance of the NCC conglomerate against enzymatic attack of CBH1 makes the packed NCC fibres a potential alternative to the Avicel residues in the FSEC samples, which are almost not degraded by the enzymes.

Single crystalline features are marked by red arrows in the phase images in Fig. 71. These structures are attacked by CBH1. A sequence of phase images of these features during CBH1 exposure is shown in Fig. 72. The degradation of the fibre marked by the blue arrow can be observed, lengthwise degradation is strongly assumed. The NCC samples allow very detailed observations of the degradation process; these investigations will be intensified in the experiments conducted on combined TMSC/NCC substrates. In the next step the resistance of the packed NCC fibres is investigated by applying the supernatant to see whether synergistic effects of cellulases lead to degradation of NCC.

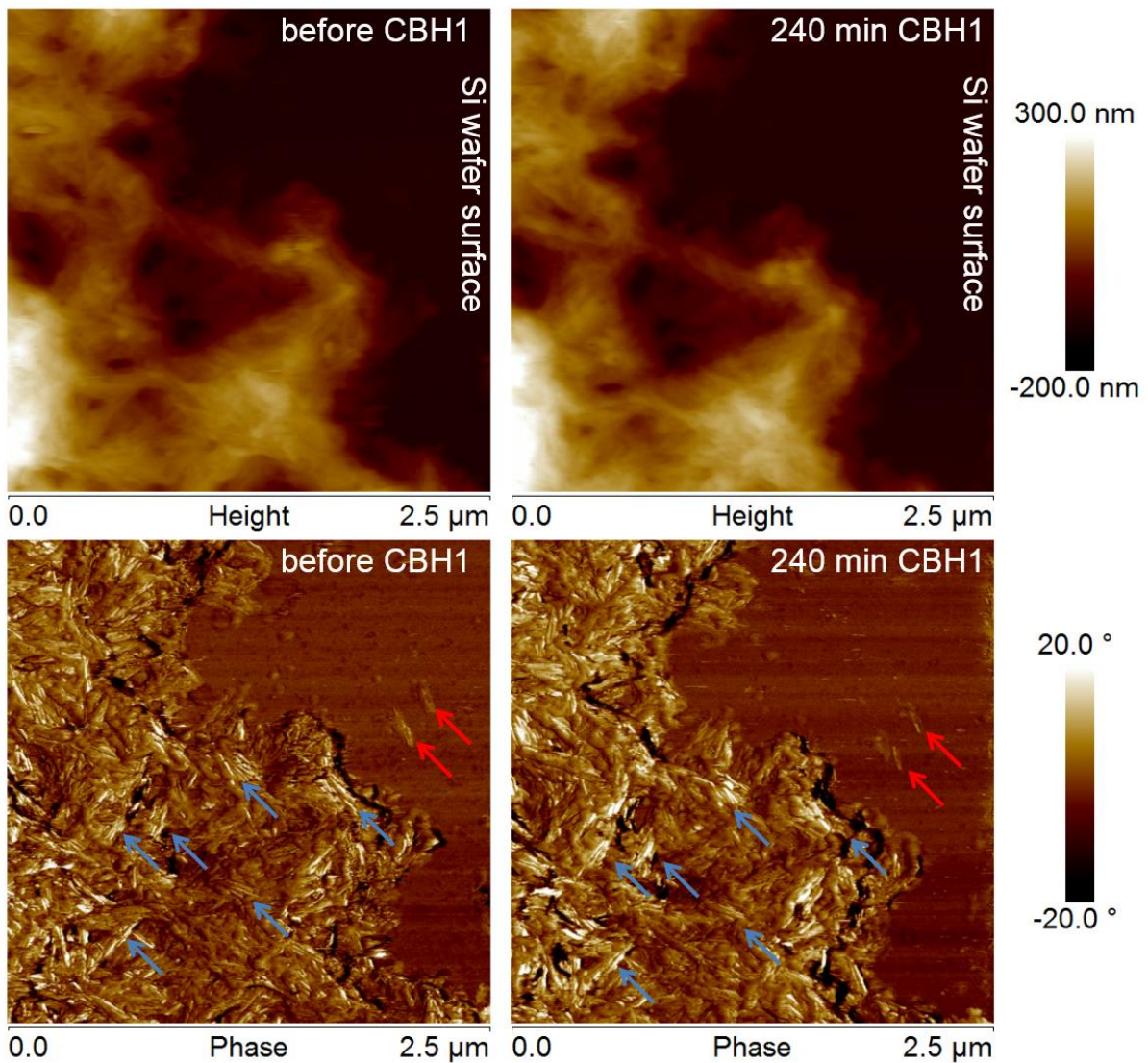


Fig. 71: Before (left) and after (right) exposure 2.5  $\mu\text{m}$  height (top) and phase (bottom) images of a NCC sample. CBH1 is applied for 4 hours. In the phase images the blue arrows mark crystalline features in the NCC conglomerate that are only slightly effected. The red arrows point at single crystalline features that are altered during exposure to CBH1.

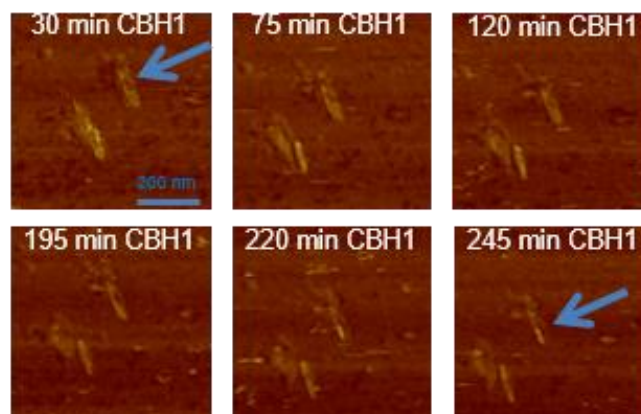
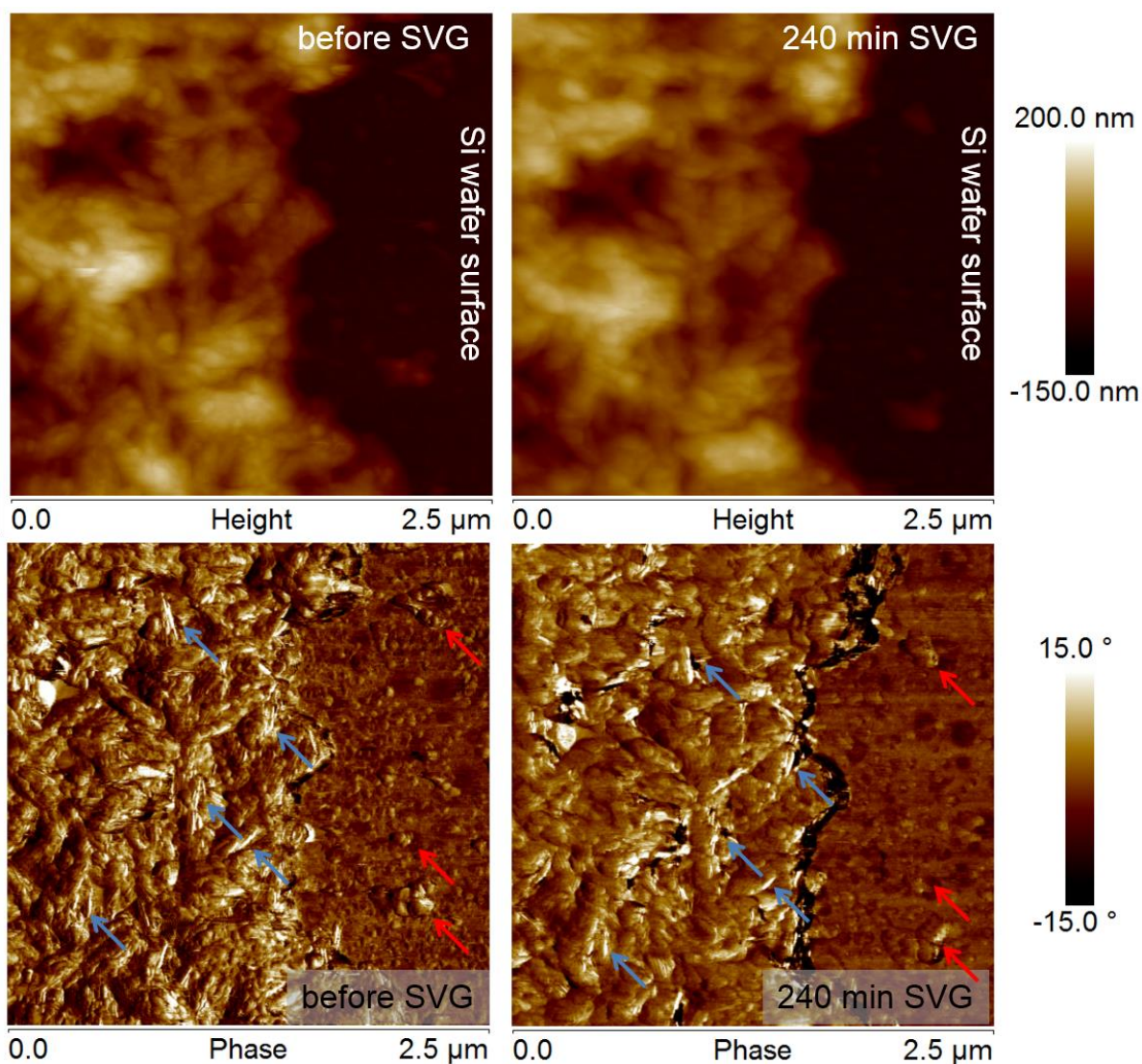


Fig. 72: Sequence of phase images of the single crystalline features during CBH2 exposure that are marked by red arrows in Fig. 71. The blue arrow marks a fibre that is supposed to be degraded lengthwise.

### SVG on NCC

Exposing NCC to the supernatant SVG for 4 hours should give insights into the behaviour of the enzymatic mixture as the single cellulase CBH1 only has effects on the single fibres but not on the packed substrate. Before-after 2.5  $\mu\text{m}$  height (top) and phase (bottom) images can be seen in Fig. 73. In thorough height degradation analysis no effects of degradation can be registered; analysis of roughness provides a mean value for  $R_q = 41.4 \pm 1.1$  nm. This indicates almost no or very little degradation. Apart from slightly reduced information in the height images, which can be traced back to the swelling of the cellulose fibres in liquid and probable agglomeration of material on the tip, no changes can be noticed in the pack of fibres. Alterations along the edge can again (as in the CBH1 experiment) be attributed to tip influences. Also the phase images become more indistinct; overall only minor effects on the crystallites can be observed (marked by blue arrows in the phase images in Fig. 73). The NCC samples form cellulose of type I [37]. Also the Avicel residues in the FSEC samples are known to consist of cellulose I. These features remain largely unchanged by cellulases. The large conglomerate of crystalline fibres seems to act like one of these residues that are not accessible to SVG. The same observations have been made in the CBH1 experiment (see above). Like in the CBH1 experiment on NCC single crystalline structures are affected by the enzymatic attack (marked by red arrows) although in this experiment no details of degradation can be observed. As SVG shows almost no activity on the NCC sample residues of amorphous cellulose can be excluded.

Further investigations with well-distributed single fibres in the amorphous TMSC matrix (= combined TMSC/NCC samples in chapter 6.3.3) will follow.



**Fig. 73:** Before (left) and after (right) exposure 2.5  $\mu\text{m}$  height (top) and phase (bottom) images of a NCC sample. SVG is applied for 4 hours. In the phase images the blue arrows mark crystalline features in the NCC conglomerate that are only slightly effected. The red arrows point at single crystalline features that are altered during exposure to SVG.

### 6.3.3 TMSC/NCC

Intensive testing of TMSC and NCC showed, that the two types of substrate represent the amorphous and crystalline structures of cellulose respectively. In the enzymatic degradation experiments of TMSC degradation is clearly observable. Exposing NCC to CBH1 and SVG reveal that larger conglomerates are not attacked by the enzymes, they behave like the Avicel residues in the FSEC samples. Single crystalline features are altered and indications of lengthwise degradation of the fibres can be observed. Thus single NCC fibres are regarded to be suitable for representing well-defined crystalline structures in the cellulose substrates. Hence the next logical step is to combine the TMSC and NCC substrates to form a new type of sample that can serve as an alternative to the FSEC samples.

To obtain single NCC fibres in the amorphous TMSC matrix a knife point of the highly concentrated NCC gel is mixed into 4 ml of the TMSC solution; several drops of isopropanol are added. After 30 seconds of sonication the sample is spin casted right away (speed: 4300 rpm, duration: 1 min) and finally exposed to HCl vapour. It is crucial, that the NCC concentration is not too high to guarantee operational samples.

An AFM height image of a TMSC/NCC sample in dry environments can be seen in Fig. 74. The NCC fibres (marked by the blue arrows) are embedded in the amorphous matrix (brown surface). This new type of samples offers full control over the properties of the substrate. The thickness  $d$  of the amorphous film can be adjusted by varying the concentration of TMSC in the solvent (here:  $d \approx 32$  nm). The NCC fibres with their well-defined features (dimensions of single features approx.  $200$  nm  $\times$   $30$  nm  $\times$   $10$  nm) are homogeneously distributed over the amorphous matrix by sonication of the TMSC/NCC solution and subsequent spin casting. Moreover, the sample is very flat (overall  $R_q \approx 9$  nm), predominantly amorphous regions feature  $R_q \approx 2$  nm.

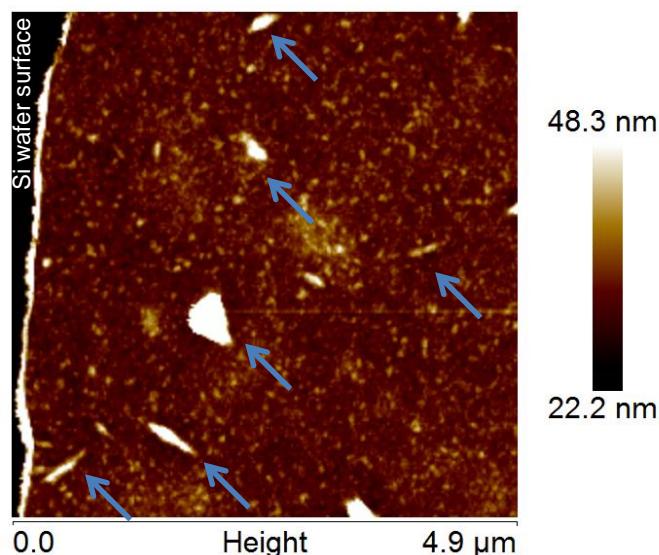


Fig. 74: AFM height image of a TMSC/NCC sample in dry environments. The blue arrows mark NCC fibres.

The following degradation experiments will show the behaviour of the new type of sample during enzymatic attack and their suitability for these investigations.

### 6.3.3.1 Enzymatic degradation experiments on TMSC/NCC

The suitability of the new TMSC/NCC substrate in enzymatic degradation experiments is tested by applying SVG and by a synergism experiment with CBH2/CBH1. In both investigations the amorphous film is expected to be degraded while single NCC features are excavated and eventually degraded as well. Hence the new sample should offer the possibility of detailed observation of the degradation process on the different cellulose structures (amorphous/crystalline) with quantitative estimations of degradation (Si wafer = absolute marker) that have never been realizable with the FSEC samples.

#### SVG on TMSC/NCC

The TMSC/NCC sample is placed in the liquid cell filled with buffer solution and continuously observed for 4 hours during exposure.  $2.5$   $\mu$ m height (top) and phase (bottom) images 10 (left), 132 (middle) and 201 (right) minutes after adding SVG are shown in Fig. 75. It is clearly visible that the TMSC film is degraded during the course of the experiment; already after 3.5 hours the amorphous film is completely degraded. Height degradation analysis supplies a mean degradation velocity of  $v_{d,a,SVG} = 0.6$  nm/min for the amorphous regions. Investigation of the degradation of the amorphous film indicates internal variations of crystallinity within the amorphous matrix as features of assumed higher crystallinity are excavated before being degraded as well (see middle image in Fig. 75). This can be substantiated by the phase images where variations in the edges of the signal can be assigned to

variations in the height images (marked by green circles). This confirms the assumptions made in chapter 6.3.1.4 where internal structures of higher crystallinity in the amorphous TMSC films were first hypothesized.

Embedded NCC fibres are marked by blue arrows in Fig. 75. The degradation experiments on NCC showed that single crystalline features are altered by the enzymes (in contrast to larger packs of fibres which are not accessible). This observation can also be made in this experiment on TMSC/NCC where the single crystalline features are excavated and eventually degraded as well. The degradation velocity for crystalline fibres averages out at  $v_{d,c,SVG} = 0.8 \text{ nm/min}$ ; when the fibres are excavated the velocity is higher ( $v_{d,c,SVG} = 1.0 \text{ nm/min}$ ). These results confirm the theory of different degradation values for different substrate areas in T. Ganner's master thesis [3]. When the amorphous matrix around the crystalline fibres vanishes due to the enzymatic degradation more contact surface on the crystalline fibres is available for enzymatic attack. Thus the fibres are degraded faster. Also the  $R_q$  value decreases significantly within the course of the experiment ( $v_{d,Rq,SVG} = 0.2 \text{ nm/min}$ ). Comparing this experiment to the SVG and CBH1 investigations on the NCC samples, the results are in accordance with the expected behaviour: single fibres of NCC are accessible to cellulases! The combined TMSC/NCC samples are quickly prepared alternatives to the FSEC samples with adjustable, well-defined properties and simplify quantitative analysis of the degradation process as the silicon wafer surface can be used as reference plane. Moreover, detailed studies of degradation that have not been possible with the FSEC samples can now be conducted on this new type of substrate!

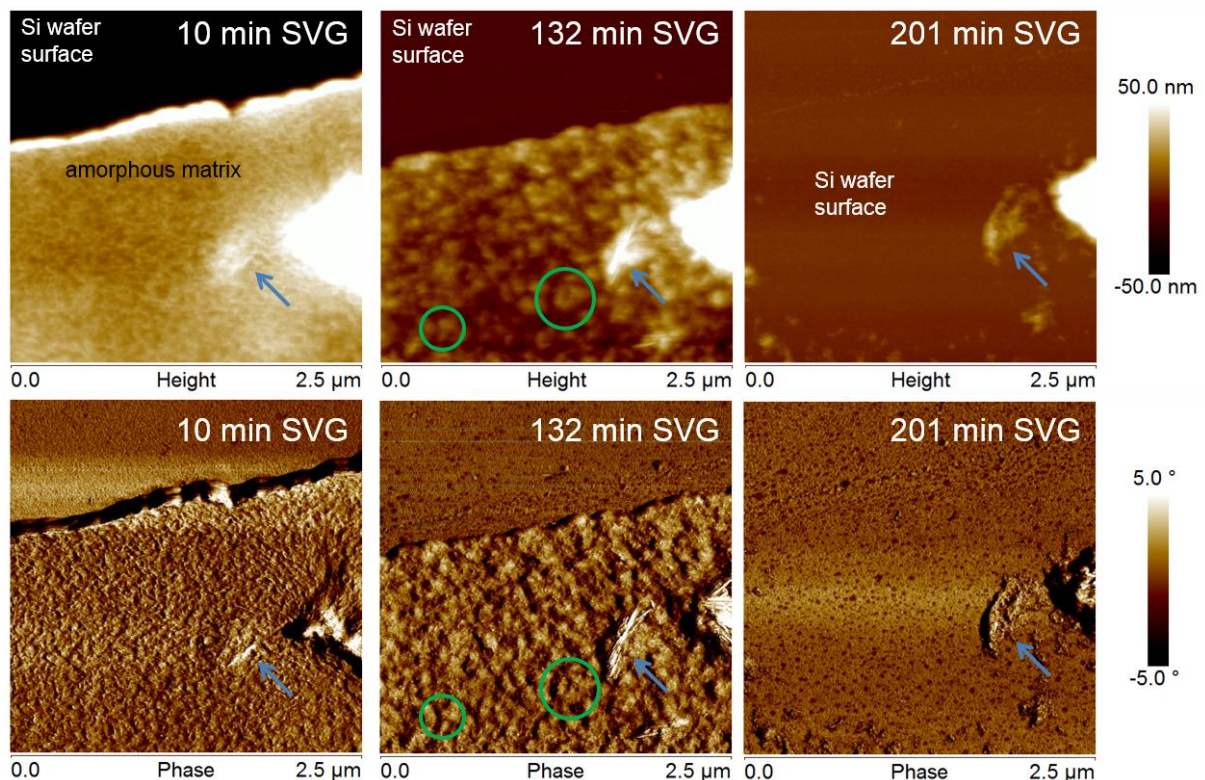


**Fig. 75:** Sequence of 2.5 µm height (top) and phase (bottom) images of a TMSC/NCC sample after 10 (left), 132 (middle), and 201 (right) minutes of exposure to SVG. The amorphous matrix is degraded and the Si wafer surface fully uncovered. Blue arrows mark single NCC features embedded in the amorphous matrix, which are excavated and degraded. Green circles mark features of higher crystallinity within the amorphous matrix.

### CBH2/CBH1 on TMSC/NCC

The suitability of the newly introduced TMSC/NCC samples is proven by the exposure to SVG (see above). The next step is to monitor single cellulase exposure to CBH2, immediately followed by exposure to CBH1 to observe synergistic effects of the enzymes. CBH2 is expected to attack amorphous regions at first, so that crystalline features are excavated and then degraded as well, as CBH2 has been reported to be active on both cellulose structures [3]. Subsequently, CBH1 will degrade the largely exposed crystalline features.

2.5  $\mu\text{m}$  height images after 31 min (left) of CBH2 and 148 min of CBH2 and 242 min of CBH1 (right) are shown in Fig. 76. Blue arrows mark NCC features embedded in the amorphous matrix, which will be excavated by CBH2. The excavation of these features can be observed in the sequence of phase images in Fig. 77 where NCC structures are marked by yellow and green circles. As expected, CBH2 attacks both the amorphous and the crystalline regions of the cellulose sample. The high scan rate ( $\approx 1$  image/4 min) allows the detailed observation of the degradation process of the crystalline fibres, they are degraded lengthwise. These observations have already been made in the enzymatic degradation experiments on NCC and are thus confirmed by this experiment on the combined TMSC/NCC samples. During the 2.5 hours of exposure to CBH2 crystalline fibres are excavated quickly, the first structures inside the amorphous matrix are already visible after applying CBH2 for 31 min (marked by blue arrows in Fig. 76) due to the rather high enzyme concentration. The velocity of degradation of the amorphous areas can be estimated by  $v_{d,a,CBH2} = 0.3 \pm 0.1$  nm/min. The crystalline fibres are degraded substantially faster. The roughness  $R_q$  of the sample is very homogenous during CBH2 exposure,  $R_q = 40 \pm 2$  nm which indicates homogenous degradation of the substrate.

The synergistic effects of CBH2/CBH1 can be observed by analysing the degradation quantitatively. Adding CBH1 accelerates the degradation process, the velocity of degradation increases to  $v_{d,a,CBH2+CBH1} = 0.4 \pm 0.1$  nm/min. The synergism of cellulases is therefore also proven on TMSC/NCC samples. The degradation is still very homogenous; this becomes manifest in small changes in the  $R_q$  value of  $v_{Rq} < 0.1$  nm/min. These values give an insight into the quantitative degradation on the TMSC/NCC samples; however they should not be compared to absolute values obtained from former experiments on FSEC samples, as the enzymatic concentrations are not the same.

By comparing overview images (not shown here) at the beginning and end of the experiment the scan area of the 2  $\mu\text{m}$  consecutively taken images is clearly discernible. This indicates tip influences.

Nevertheless, detailed information about the (synergistic) degradation process can be obtained. This experiment confirms the applicability of the TMSC/NCC samples as alternatives to the FSEC samples in synergistic investigations as well and completes the proof of concept of this new type of substrate.

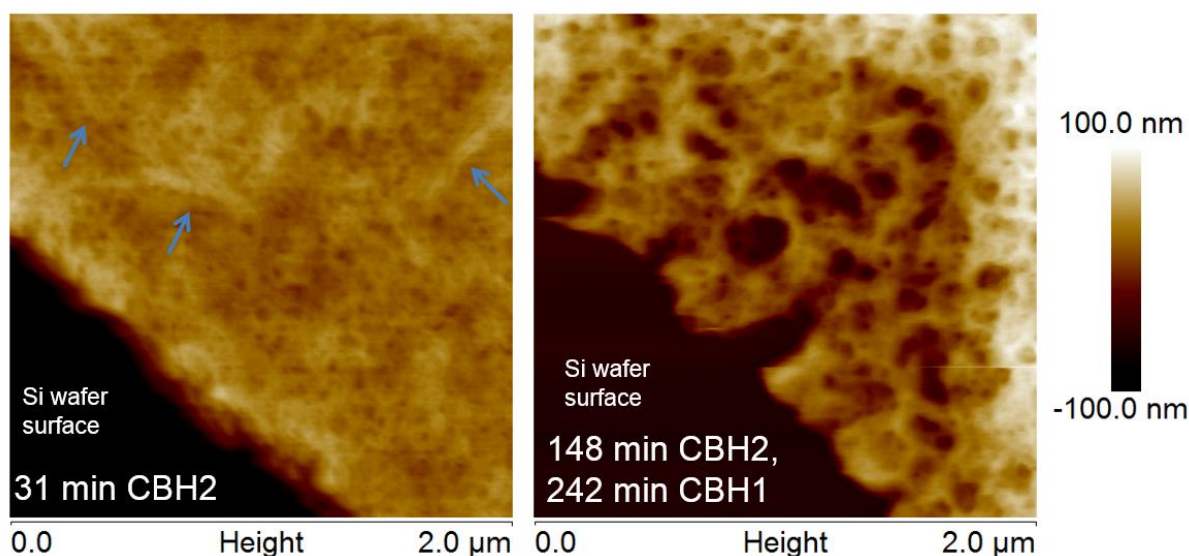


Fig. 76: 2  $\mu\text{m}$  height images of a TMSC/NCC sample after 31 min of CBH2 (left) and 148 min of CBH2 and 242 min of CBH1 (right). The blue arrows in the left image mark NCC features embedded in the amorphous matrix.

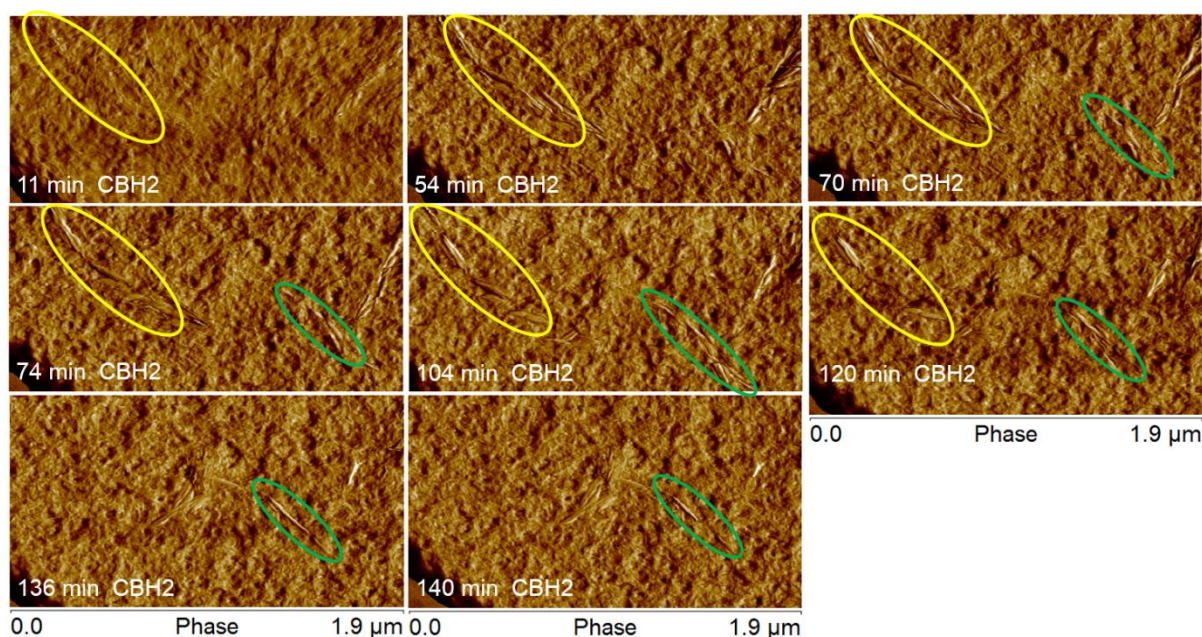


Fig. 77: Sequence of phase images during CBH2 exposure. The yellow and green circles mark NCC features that are excavated and degraded. Lengthwise degradation of the fibres can be observed.

### 6.3.4 Summary and outlook SCC

Spin cast cellulose (SCC) samples are quickly prepared and offer reproducible, well-defined structures. These newly introduced samples are a combination of TMSC and NCC substrates. Investigations (XRD, Raman spectroscopy) of TMSC reveal its amorphous structure. Raman spectroscopy of NCC demonstrates its crystalline structure (cellulose I). AFM examinations of the layer thickness of the TMSC films determine the concentration of TMSC in the solvent to be the only parameter for controlling the film thickness. Moreover the morphology of TMSC is studied by AFM. The samples are very flat ( $R_q < 2 \text{ nm}$ ) and widely amorphous. However, superimposing height and phase profiles in certain areas hypothesize the occurrence of internal structures with higher crystallinity in the TMSC samples. Nevertheless these

crystalline features are just vague in comparison to the well-defined structures provided by NCC (dimensions of single crystals (approx.  $200\text{ nm} \times 30\text{ nm} \times 10\text{ nm}$ ). The values of dimensions of NCC are received from SEM, TEM and AFM investigations.

The findings of the characterization experiments evidence that combing TMSC and NCC is an alternative to the well-tested FSEC samples. These assumptions are corroborated by the enzymatic degradation experiments conducted on the single components as well as on the combined TMSC/NCC substrate. Degradation is observable both quantitatively and qualitatively. Degradation of the high-resolution nano-crystalline fibres can be scrutinized in great detail and shows the lengthwise decomposition of these structures.

For obtaining comparable quantitative results of former degradation experiments the enzyme concentration on this new type of substrate has to be adjusted in future investigations.

The only limitations of these substrates are the flat layers, which are quickly degraded. Thus long-time studies cannot be conducted with single layer samples. However, multi-layer substrates can be produced, which offer a wide range of possibilities, especially when layers with varying properties are combined. Another possibility to extend the film thickness and thus the period of observation of the degradation process is the increase of concentration of TMSC in the solvent. Tests have to be performed to find the limit of solution.

Once more it should be emphasized that the combined TMSC/NCC sample represents a real alternative to the FSEC samples in several aspects. Many models that were found in experiments conducted on FSEC samples could be confirmed with the TMSC/NCC samples. Enzymatic attack was observed to occur at already existing gaps as reported by Bubner et al. [40]. The amorphous and crystalline features are degraded selectively at different velocities and CBH2 is not only active on crystalline but also on amorphous structures as stated by Ganner et al. [15]. Larger packs of NCC behave like Avicel residues in the FSEC samples and are not attacked by the enzymes. Synergistic effects of CBH1 and CBH2 can be proven as well as quantitative measurements are facilitated by the Si wafer surface which serves as absolute surface marker. All these investigations can be conducted with very high spatial resolution in the lower nanometer range. Moreover, the spin casting process provides very flat samples that have never been achieved by ultramicrotomy cuts and the preparation process of the TMSC/NCC samples is completed within 2 hours in comparison to the strenuous, 1 week procedure of the FSEC samples.

All these factors make TMSC/NCC a very promising new type of cellulose substrate!

## 7 Summary

Atomic force microscopy (AFM) represents an excellent tool for real time observation of enzymatic cellulose degradation in liquid environments. However, the demands on the cellulose substrates, investigated by AFM, are very high: **1)** they have to be nano-flat in order to provide highest lateral resolution towards molecular cellulose tracking and **2)** they need to be tunable by means of its crystalline and amorphous contents. While natural samples are not suitable for such investigations as they are rough and show uncontrolled composition, tunable artificial substrates represent an ideal approach for AFM based real time investigations. Based on previous work at the Institute for Electron Microscopy and Nanoanalysis, all requirements were fulfilled by fractional solvent exchange cellulose samples (**FSEC**), which feature multiphase structures (i.e. amorphous and crystalline regions) like natural cellulose. Undissolved crystalline residues enable the quantitative measurement of degradation, as they are almost not affected by the enzymes. However, the embedding of crystalline features cannot be precisely controlled during the preparation process by means of spatial distribution and crystal sizes. Therefore, the well-studied FSEC1 samples [2, 3, 4] are further developed by adding additional crystalline Avicel flakes after the completed mixing procedure (**FSEC2**). Characterization of these new FSEC2 samples via light microscopy, X-ray diffraction, and Raman spectroscopy show improvement regarding the controlled embedding of crystalline features. In consequence of this apparent improvement enzymatic degradation experiments are conducted not only on FSEC1 but also on FSEC2 samples to study the influences of GH61, which has been reported to increase the activity of cellulases [16, 17, 18, 19]. The boost of activity by GH61 can be confirmed for EG1, CBH2, and the supernatant SVG. This is reflected in a substantial increase of the degradation velocity compared to the activity in the reference experiments conducted with single cellulases. Nevertheless, the enzymatic degradation experiments on FSEC2 reveal that the crystalline residues are widely torn out during the ultramicrotomy cutting and complicate the quantitative analysis of the degradation process. Hence, a new type of substrate had to be found which provides control over compositional properties, suitable for quantitative measurements.

Following previous activities, spin cast cellulose (**SCC**) samples were re-considered and characterized in much more detail. As a main aspect, the spin casting process provides highly reproducible [35] samples in terms of thickness and surface roughness down to the sub-nm range. However, to meet our requirements, the SCC samples have to be multiphasic which is realized by a two component approach: **1)** the amorphous phase is introduced by trimethylsilyl cellulose (**TMSC**) [38] while **2)** crystalline features are embedded using nano-crystalline cellulose (**NCC**) [37]. The amorphous character of TMSC is confirmed by XRD, Raman, and AFM investigations although a small amount of nano-crystalline areas has been found. Such TMSC films provide very flat surfaces ( $R_q < 2$  nm) with defined thickness control via TMSC concentration in the solvent. On the other hand, Raman spectroscopy confirms NCC as purely crystalline cellulose. The dimensions of the well-defined nano-crystalline fibres (approx.  $200 \text{ nm} \times 30 \text{ nm} \times 10 \text{ nm}$ ) are studied by SEM, TEM, and AFM. The suitability of both phases, TMSC and NCC, for enzymatic degradation experiments has individually been investigated by real time AFM using single cellulases and supernatants, which proved the expected behaviour: while amorphous TMSC film and single NCC features are accessible for the relevant enzymes, NCC agglomerates behave like Avicel residues in FSEC samples and are widely unaffected.

By combining the TMSC and NCC samples a new TMSC/NCC substrate is introduced. Conducting several enzymatic degradation experiments on the novel type of sample confirms that TMSC/NCC samples are an excellent alternative to the FSEC samples. Very detailed structural and quantitative analysis of the degradation process can be performed in high resolution. Many models of enzymatic degradation that are based on results from experiments on FSEC samples could be confirmed with the

TMSC/NCC samples (e.g. embedding of crystalline residues, selective degradation of amorphous/crystalline features, exo- and endo-glucanase character of CBH2, synergism). Another crucial advantage of the TMSC/NCC samples is their fast fabrication time of about 2 hours compared to the 1 week procedure of FSEC samples.

Together, with the full control over the properties (film thickness, embedding of crystalline features), the new TMSC/NCC samples developed in this thesis represent a very promising type of artificial cellulose substrate that should facilitate the detailed investigation of the enzymatic degradation of cellulose which in turn should lead to the improvement of the production of second generation biofuels.

## 8 Outlook

The introduction of the combined TMSC/NCC spin cast samples offers an excellent tunable alternative to the FSEC samples with their cumbersome preparation.

The new type of substrate allows unlimited possibilities of taking a detailed look on the degradation process of cellulose in both structural and quantitative respects. The investigations may range from studying the influences of new enzymes to the establishment of multi-layered cellulose samples with varying layer properties to study the degradation process selectively. All these studies will be possible on nano-scale level on quickly prepared samples with full control over their properties.

## 9 List of abbreviations

|        |   |
|--------|---|
| AA9    | auxiliary activity 9                        |
| AFM    | atomic force microscope/microscopy          |
| AGU    | anhydroglucose units                        |
| BGL    | $\beta$ -glucosidase                        |
| BMIMCl | 1-N-butyl-3-methylimidazolium chloride      |
| CBH    | cellobiohydrolase                           |
| CBM    | carbohydrate-binding module                 |
| CDH    | cellobiose dehydrogenase                    |
| EC     | enzyme commission number                    |
| EDX(S) | energy dispersive X-ray (spectroscopy)      |
| EELS   | electron energy loss spectroscopy           |
| EG     | endo-glucanase                              |
| FSEC   | fractional solvent exchange cellulose       |
| GH61   | family 61 glycoside hydrolase               |
| LIMI   | light microscope/microscopy                 |
| NCC    | nano-crystalline cellulose                  |
| PMO    | polysaccharide monooxygenases               |
| PSD    | position sensitive photodetector            |
| SCC    | spin cast cellulose                         |
| SEM    | scanning electron microscope/microscopy     |
| SPM    | scanning probe microscope/microscopy        |
| STM    | scanning tunnelling microscope/microscopy   |
| TEM    | transmission electron microscope/microscopy |
| TMSC   | trimethylsilyl cellulose                    |
| XRD    | X-ray diffractometry                        |

# 10 List of tables

|  |    |
|--|----|
| Table 1: <i>Trichoderma reesei</i> cellulases. [1] The cellulases used within this thesis are marked bold. ....          | 5  |
| Table 2: Effective forces between tip and sample .....   | 11 |
| Table 3: Overview of AFM enzymatic degradation experiments .....   | 22 |
| Table 4: Comparison of degradation velocities $v_d$ in the GH61-cellulase and cellulase reference experiments. ....      | 43 |
| Table 5: Mean thickness $d$ of TMSC layers in dry and liquid environments depending on the TMSC concentration $c$ . .... | 51 |

# 11 List of figures

|   |    |
|---|----|
| Fig. 1: Molecular structure of cellulose showing the non-reducing and reducing ends and the numbering of the C atoms. $n$ = degree of polymerization (DP). [7] .....  | 2  |
| Fig. 2: Crystal structure of cellulose I $\beta$ (left) and cellulose II (right). a) Projection of the unit cell on the a-b plane; the parallel chains of cellulose I and the antiparallel chains of cellulose II can be seen. b) Projection of the unit cell parallel to the (100) plane of cellulose I and to the (010) plane of cellulose II. The hydrogen bonds are drawn as well. [7] .....                                    | 3  |
| Fig. 3: Conversion of the polymorphs of cellulose. [9] .....  | 3  |
| Fig. 4: Structural organization in plants. [6] .....  | 4  |
| Fig. 5: Structure of cellobiose. [13] .....   | 5  |
| Fig. 6: Scheme of the hydrolysis of amorphous and crystalline cellulose by cellulases. Open squares represent non-reducing ends, solid squares represent reducing ends. The collaboration of the enzymes – the synergism – becomes clear. [14] .....  | 5  |
| Fig. 7: Side view of the catalytic module of CBH1 processing a cellulose chain (red) in its tunnel. [3]6  | 6  |
| Fig. 8: Front view of the catalytic module of CBH2. [3] .....   | 6  |
| Fig. 9: Side and bottom view of EG3, representing the shape of EGs with the trench and the grabber. [3] .....   | 6  |
| Fig. 10: Current view on enzymatic degradation of cellulose. C1 and C4 oxidizing GH61 enzymes are shown which generate optimal (non-oxidized) ends for CBH1 and CBH2 (oxidized sugars in red). Thus, new chain ends for the CBHs are created (indicated by the arrows on the bottom). [17] .....  | 7  |
| Fig. 11: The main components of the AFM. 1: tip. 2: cantilever. 3: motion system. 4: detection system. [23] .....   | 8  |
| Fig. 12: Influences on the image quality. Higher resolution can be achieved with a fine tip (left); a dull tip (middle) is not able to resolve fine features. Particles that stick to the tip can distort the true structure of the sample (right). [23] .....  | 9  |
| Fig. 13: SEM images of v-shaped (top) and rectangular (bottom) cantilevers. The right column shows a pyramidal (top) and a tetragonal (bottom) tip. [23] .....  | 9  |
| Fig. 14: Left: By applying a positive or negative voltage a piezocrystal either expands or contracts. This behaviour is used in the tube scanner of the motion system of an AFM (right). [23] .....   | 10 |
| Fig. 15: The piezoelectric elements are moved by applying reverse voltage to the associated segments. [23] .....  | 10 |
| Fig. 16: Optical detection system and image acquisition of an AFM. Left: the cantilever's initial position/bending. Middle: The cantilever is deflected due to change in height, the laser beam hits a different position on the PSD. Right: the feedback system controls the motion system so that the cantilever gets back to its initial position/bending. The deflection signal is processed to obtain an AFM image. [23] ..... | 11 |
| Fig. 17: Effective forces between tip and sample during the approach. The overall Lenard-Jones potential is depicted in blue, the repulsive electron-electron and the attractive Van der Waals interactions are drawn in red and green. [23] .....  | 12 |
| Fig. 18: Damping of the amplitude and shifting of the resonance frequency when the tip couples with the sample in tapping mode. [23] .....  | 13 |
| Fig. 19: AFM phase mode. The phase lag of the free cantilever (left) is different from the phase lag of the cantilever that is coupled with the sample (right). The phase image provides information about the material's composition and topological features. [23] .....  | 13 |
| Fig. 20: Liquid cell (in-house construction by T. Ganner [3]) .....   | 14 |

|  |    |
|--|----|
| Fig. 21: Resonance curves of a cantilever in air (left) and in liquid (right). [4] .....   | 14 |
| Fig. 22: XRD spectra of cellulose I (left, including amorphous cellulose) and cellulose II (right). [26]<br>.....  | 15 |
| Fig. 23: Leica ultramicrotome. [32] .....  | 17 |
| Fig. 24: Drying of the gel between glass slides (left) and resulting stiff flakes after the fractional<br>solvent exchange (right). [3] .....  | 18 |
| Fig. 25: Depiction of the cutting process of an embedded FSEC sample by ultramicrotomy. [2] .....  | 18 |
| Fig. 26: TMSC samples with 1 to 5 layers spin coated on the Si wafer. [32].....  | 19 |
| Fig. 27: Graphical overview of the substrate development in this thesis.....   | 21 |
| Fig. 28: LIMM images of FSEC1 (left), FSEC2 (middle) and FSEC3 (right) samples. The red squares<br>indicate the area for the subsequent characterisation experiments via Raman spectroscopy. ....  | 24 |
| Fig. 29: XRD spectra of FSEC1 (blue), FSEC2 (red), FSEC3 (olive) and Avicel (black). ....  | 25 |
| Fig. 30: Raman spectra of a FSEC1 sample. The insert shows a mapping of the marked region in the<br>LIMM images in Fig. 28. The cyan curve represents the crystalline spectrum with its characteristic<br>peaks (marked by +). The pink curve shows the amorphous spectrum with its characteristic peaks<br>(marked by *). ....  | 26 |
| Fig. 31: Raman spectra of a FSEC2 sample. The insert shows a mapping of the marked region in the<br>LIMM images in Fig. 28. The cyan curve represents the crystalline spectrum with its characteristic<br>peaks (marked by +). The pink curve shows the amorphous spectrum with its characteristic peaks<br>(marked by *). ....  | 26 |
| Fig. 32: Raman spectra of a FSEC3 sample. The insert shows a mapping of the marked region in the<br>LIMM images in Fig. 28. The cyan curve represents the crystalline spectrum with its characteristic<br>peaks (marked by +). The pink curve shows the amorphous spectrum with its characteristic peaks<br>(marked by *). ....  | 26 |
| Fig. 33: 10 $\mu\text{m}$ AFM phase images of a FSEC1 (left), FSEC2 (middle), and FSEC3 (right) sample.<br>The blue frames mark Avicel residues in the FSEC1 and FSEC3 samples. Such residues can barely be<br>found in the FSEC2 samples. ....  | 27 |
| Fig. 34: Before (left) and after (right) exposure 10 $\mu\text{m}$ height images of a FSEC1 sample. SVG is<br>applied for 5 hours. The blue frames mark the crystalline reference residue. ....  | 30 |
| Fig. 35: 3D-height details of the crystalline residue in Fig. 34. The residue is marked by a blue frame<br>in the images before (left) and after (right) exposure to SVG. The blue arrows point at grooves caused<br>by ultramicrotomy; the green arrows indicate internal crystalline features that are excavated. ....   | 30 |
| Fig. 36: Before (left) and after (right) exposure 2 $\mu\text{m}$ height (top) and phase (bottom) images of a<br>FSEC1 sample. GH61 is applied for 4 hours. The green arrows indicate the groove caused by<br>ultramicrotomy that goes right through the residue. The blue arrows in the phase images mark several<br>of the crystalline fibres that are unaffected by the enzymes. ....                                     | 31 |
| Fig. 37: Before (left) and after (right) exposure 10 $\mu\text{m}$ height images of a FSEC1 sample. After 4<br>hours of GH61 SVG is applied for 3 hours. The blue frames mark the crystalline reference residue. .   | 32 |
| Fig. 38: Before (left) and after (right) exposure 2.5 $\mu\text{m}$ 3D height images of a FSEC2 sample. EG1 is<br>applied for 4 hours. The blue arrows mark regions of higher crystallinity than the amorphous matrix<br>which are excavated by EG1.....   | 32 |
| Fig. 39: Sequence of height images during EG1 exposure. The scale bar is 500 nm. Blue arrows point<br>at amorphous regions that are degraded by EG1. Green arrows indicate regions with higher<br>crystallinity that are excavated.....  | 33 |
| Fig. 40: Sequence of 2.5 $\mu\text{m}$ height (top) and phase (bottom) images of a FSEC1 sample. The left<br>images are taken before exposure to GH61, the images in the middle show the sample after 4 hours of<br>GH61 and right before exposure to EG1. The right images illustrate the situation after 3.5 hours of<br>EG1 exposure. The residue is marked. Blue arrows in the height images point to amorphous regions. |    |

|  |    |
|--|----|
| Green arrows indicate crystalline structures that are excavated by EG1. In the phase images the red arrows mark crystalline features that are not affected by GH61 and excavated by EG1.....   | 34 |
| Fig. 41: Before (left) and after (right) exposure 2.5 $\mu\text{m}$ 3D height images of a FSEC2 sample. CBH2 is applied for almost 5 hours. The blue arrows mark regions of higher crystallinity that are excavated by CBH2. ....  | 35 |
| Fig. 42: Sequence of height images during CBH2 exposure. The scale bar is 500 nm. Blue and green circles mark regions of higher crystallinity that are excavated and degraded by CBH2. ....  | 35 |
| Fig. 43: Before (left) and after (right) exposure 2 $\mu\text{m}$ height (top) and phase (bottom) images of a FSEC2 sample. GH61 is applied for 4 hours. Green arrows in the height images indicate widening of already existing gaps. The blue arrows in the height and the phase images indicate assumed crystalline regions that are affected by GH61. The green arrows in the phase images mark additional crystalline features that are altered. .... | 36 |
| Fig. 44: Before (left) and after (right) CBH2 exposure 2.5 $\mu\text{m}$ 3D height images of a FSEC2 sample. After 4 hours of GH61, CBH2 is applied for 4 hours. The blue arrows mark regions of higher crystallinity that are excavated by CBH2. ....   | 37 |
| Fig. 45: Before (left) and after (right) exposure 1.5 $\mu\text{m}$ height images of a FSEC2 sample. CBH1 is applied for more than 3 hours. The blue arrows mark gaps that are widened during exposure to CBH1. ....   | 38 |
| Fig. 46: Before (left) and after (right) exposure 1.5 $\mu\text{m}$ height (top) and phase (bottom) images of a FSEC2 sample. GH61 is applied for 4 hours. Blue arrows in the height images indicate widening of already existing gaps. The green arrows in the phase images indicate crystalline features that are affected by GH61. ....   | 39 |
| Fig. 47: Before (left) and after (right) CBH1 exposure 2.5 $\mu\text{m}$ height images of a FSEC2 sample. After 4 hours of GH61 CBH1 is applied for 4 hours. The blue arrows mark same spots.....  | 40 |
| Fig. 48: Before (left) and after (right) exposure 10 $\mu\text{m}$ overview height images of a FSEC2 sample. GH61 and CBH1 are applied for 4 hours, respectively. The blue frames mark the area of the 2.5 $\mu\text{m}$ images that are taken consecutively during enzymatic exposure.....  | 40 |
| Fig. 49: Before (left) and after (right) exposure 2.5 $\mu\text{m}$ height (top) and phase (bottom) images of a FSEC2 sample. GH61 is applied for 4 hours. Blue arrows in the height images indicate widening of already existing gaps. The green arrows in the phase images indicate crystalline features that are affected by GH61.....  | 41 |
| Fig. 50: Before (left) and after (right) CBH1 exposure 2.5 $\mu\text{m}$ height images of a FSEC2 sample. After 4 hours of GH61 CBH1 is applied for 4 hours. The blue arrows mark gaps that are widened during exposure to CBH1. The green circles indicate crystalline areas.....   | 42 |
| Fig. 51: Before (left) and after (right) exposure 10 $\mu\text{m}$ overview phase images of a FSEC2 sample. GH61 and CBH1 are applied for 4 hours, respectively. The blue frames mark the area of the 2.5 $\mu\text{m}$ images that are taken consecutively during enzymatic exposure.....   | 42 |
| Fig. 52: Bar graph of the degradation velocities $v_d$ of the supernatant SVG and the cellulases EG1 and CBH2 in comparison to the degradation velocities of the cellulases with prior exposure to GH61 (marked in yellow).....  | 44 |
| Fig. 53: XRD spectra of a TMSC (red) and a FSEC (blue) sample with the crystalline reference spectrum of Avicel (black).....   | 46 |
| Fig. 54: Raman spectra of crystalline cellulose (pink) [39] and TMSC (cyan). ....  | 46 |
| Fig. 55: Light microscopy images of 3 different TMSC samples with different concentrations of TMSC in Xylol. The samples are scratched with tweezers on the left. The scale bar is 10 $\mu\text{m}$ . ....   | 47 |
| Fig. 56: 1 $\mu\text{m}$ height and phase AFM images of a TMSC sample (15 g/l, 6300 rpm) representing the morphology of the TMSC samples in dry environments. The red bar marks the region for the profiles in Fig. 57. ....   | 48 |

|  |    |
|--|----|
| Fig. 57: Left: Phase (top) and height (bottom) profiles taken at the position marked by the red bar in the detail phase (top) and height (bottom) images on the right (also in Fig. 56). The blue boxes in the profiles indicate probable crystalline features. The scale bar for the phase and height images is 100 nm. ....  | 48 |
| Fig. 58: Collection of height images of TMSC samples with varying preparation parameters (spin rate and concentration). Regions with assumed higher crystallinity are marked by red circles. ....  | 49 |
| Fig. 59: Collection of phase images of TMSC samples with varying preparation parameters (spin rate and concentration). Regions with assumed higher crystallinity are marked by red circles. ....   | 50 |
| Fig. 60: 100 nm 3D height detail of a TMSC sample (15 g/l, 6300 rpm). ....   | 51 |
| Fig. 61: Layer thickness as a function of the spin rate (x-axis) and dependency on TMSC concentration (black, red, blue) in dry (left) and liquid (right) environments. The coloured lines represent the mean value of the layer thickness. Note the y-axis scale which emphasizes the swelling of the layers in liquid estimated by a factor of 2. ....                           | 52 |
| Fig. 62: TMSC layer thickness as a function of the concentration of TMSC in Xylol with first-order fits in dry (red) and liquid (blue) environments. ....  | 52 |
| Fig. 63: Before (left) and after (right) exposure 10 $\mu\text{m}$ height images of a TMSC sample. SVG is applied for 4 hours. The blue arrows mark features where degradation is visible. The left dark part displays the Si wafer surface. ....  | 53 |
| Fig. 64: Before (left) and after (right) exposure 5 $\mu\text{m}$ height images of a TMSC sample. CBH2 is applied for 2.5 hours. The blue arrows mark features where degradation is visible. The left dark part displays the Si wafer surface. ....  | 54 |
| Fig. 65: Raman spectra comparing crystalline cellulose (pink) [39] to NCC (cyan). ....   | 55 |
| Fig. 66: SEM images of the highly concentrated NCC gel (left) and single fibres (right) from the filtered clear solution with dimensions of approx. 200 nm x 30 nm. ....   | 55 |
| Fig. 67: TEM image of NCC that reveals the shape of single NCC fibres. ....  | 56 |
| Fig. 68: AFM height images of the pre-filtered NCC sample. Smaller features (< 50 nm) are marked by red arrows in the 1 $\mu\text{m}$ image (right). ....  | 56 |
| Fig. 69: 3D height (left) and phase image (right) of the 1 $\mu\text{m}$ detail of the pre-filtered NCC sample in Fig. 68. ....  | 57 |
| Fig. 70: 3D height (left) and phase image (right) of NCC fibres in dry environments. Blue arrows mark single features. Red arrows indicate piled features. ....  | 57 |
| Fig. 71: Before (left) and after (right) exposure 2.5 $\mu\text{m}$ height (top) and phase (bottom) images of a NCC sample. CBH1 is applied for 4 hours. In the phase images the blue arrows mark crystalline features in the NCC conglomerate that are only slightly effected. The red arrows point at single crystalline features that are altered during exposure to CBH1. .... | 59 |
| Fig. 72: Sequence of phase images of the single crystalline features during CBH2 exposure that are marked by red arrows in Fig. 71. The blue arrow marks a fibre that is supposed to be degraded lengthwise. ....  | 59 |
| Fig. 73: Before (left) and after (right) exposure 2.5 $\mu\text{m}$ height (top) and phase (bottom) images of a NCC sample. SVG is applied for 4 hours. In the phase images the blue arrows mark crystalline features in the NCC conglomerate that are only slightly effected. The red arrows point at single crystalline features that are altered during exposure to SVG. ....   | 61 |
| Fig. 74: AFM height image of a TMSC/NCC sample in dry environments. The blue arrows mark NCC fibres. ....  | 62 |
| Fig. 75: Sequence of 2.5 $\mu\text{m}$ height (top) and phase (bottom) images of a TMSC/NCC sample after 10 (left), 132 (middle), and 201 (right) minutes of exposure to SVG. The amorphous matrix is degraded and the Si wafer surface fully uncovered. Blue arrows mark single NCC features embedded in the  |    |

---

|   |    |
|---|----|
| amorphous matrix, which are excavated and degraded. Green circles mark features of higher crystallinity within the amorphous matrix. ....   | 63 |
| Fig. 76: 2 $\mu\text{m}$ height images of a TMSC/NCC sample after 31 min of CBH2 (left) and 148 min of CBH2 and 242 min of CBH1 (right). The blue arrows in the left image mark NCC features embedded in the amorphous matrix. .... | 65 |
| Fig. 77: Sequence of phase images during CBH2 exposure. The yellow and green circles mark NCC features that are excavated and degraded. Lengthwise degradation of the fibres can be observed. ....                                  | 65 |

---

## 12 Bibliography

- [1] J.-L. Wertz, O. Bédué and J. P. Mercier, *Cellulose Science and Technology*, Lausanne: EPFL Press, 2010.
- [2] J. Dohr, *Enzymatic degradation of superflat cellulose surfaces*, Graz, Austria: Karl Franzens University of Graz, 2011.
- [3] T. Ganner, *Enzymatic cellulose degradation via atomic force microscopy in liquid environments*, Graz, Austria: Graz University of Technology, 2012.
- [4] T. Aschl, *Tunable artificial cellulose substrates for in situ AFM investigation*, Graz, Austria: Graz University of Technology, 2013.
- [5] C. E. Mortimer and U. Müller, "Chemie," Stuttgart, Thieme, 2003, pp. 593-597.
- [6] S. Pérez and D. Samain, "Structure and Engineering of Celluloses," *Advances in Carbohydrate Chemistry and Biochemistry*, vol. 64, 2010.
- [7] D. Klemm, B. Heublein, H.-P. Fink and A. Bohn, "Cellulose: faszinierendes Biopolymer und nachhaltiger Rohstoff," *Angewandte Chemie* 117, p. 3422 – 3458, 2005.
- [8] "Rules of Carbohydrate Nomenclature," *The Journal of Organic Chemistry*, 1963.
- [9] A. C. O'Sullivan, "Cellulose: the structure slowly unravels," *Cellulose* 4, pp. 173-207, 1997.
- [10] S. Park, J. O. Baker, M. E. Himmel, P. A. Parilla and D. K. Johnson, "Cellulose crystallinity index: measurement techniques and their impact on interpreting cellulase performance," *Biotechnology for Biofuels*, vol. 3, no. 10, 2010.
- [11] M. Slaytor, "Cellulose Digestion in Termites and Cockroaches: What role do symbionts play?," *Comp. Biochem. Physiol.*, vol. 103B, no. 4, pp. 775-784, 1992.
- [12] M. K. Bhat and S. Bhat, "Cellulose degrading enzymes and their potential industrial applications," *Biotechnology Advances*, vol. 15, pp. 583-620, 1997.
- [13] Cellobiose, "PubChem," [Online]. Available: <http://pubchem.ncbi.nlm.nih.gov/summary/summary.cgi?cid=439178>. [Accessed 26 10 2013].
- [14] L. R. Lynd, P. R. Weimer, W. H. van Zyl and I. S. Pretorius, "Microbial Cellulose Utilization: Fundamentals and Biotechnology," *Microbiology and Molecular Biology Reviews*, vol. 66, no. 3, pp. 506-577, 2002.

- 
- [15] T. Ganner, P. Bubner, M. Eibinger, C. Mayrhofer, H. Plank and B. Nidetzky, "Dissecting and Reconstructing Synergism," *The Journal of Biological Chemistry*, vol. 288, no. 52, p. 43215–43222, 2013.
- [16] G. R. Hemsworth, G. J. Davies and P. H. Walton, "Recent insights into copper-containing lytic polysaccharide mono-oxygenases," *Current Opinion in Structural Biology*, vol. 23, pp. 1-9, 2013.
- [17] S. J. Horn, G. Vaaje-Kolstad, B. Westereng and V. G. Eijsink, "Novel enzymes for the degradation of cellulose," *Biotechnology for Biofuels*, vol. 5, no. 45, 2012.
- [18] R. Kittl, D. Kracher, D. Burgstaller, D. Haltrich and R. Ludwig, "Production of four *Neurospora crassa* lytic polysaccharide monooxygenases in *Pichia pastoris* monitored by a fluorimetric assay," *Biotechnology for Biofuels*, vol. 5, no. 79, 2012.
- [19] L. L. Leggio, D. Welner and L. De Maria, "A Structural Overview of GH61 Proteins - Fungal Cellulose Degrading Polysaccharide Monooxygenases," *Computational and Structural Biotechnology Journal*, vol. 2, no. 3, 2012.
- [20] G. Binnig, E. Weibel and H. Rohrer, "Surface Studies by Scanning Tunneling Microscopy," *Physikalical Review Letters*, vol. 49, pp. 57-61, 1982.
- [21] G. Binnig and C. Quate, "Atomic Force Microscope," *Physical Review Letters*, vol. 56, no. 9, pp. 930-933, 1986.
- [22] R. García, *Amplitude Modulation Atomic Force Microscopy*, Weinheim: Wiley-VCH, 2010.
- [23] *Courtesy of Harald Plank, Institute for Electron Microscopy and Nanoanalysis (FELMI-ZfE), TU Graz, Austria, www.felmi-zfe.at.*
- [24] S. H. Cohen and M. L. Lightbody, Eds., "Atomic Force Microscopy/Scanning Tunneling Microscopy 2," New York, Plenum Press, 1997, pp. 147-150.
- [25] L. Bergmann and C. Schaefer, "Lehrbuch der Experimentalphysik Band 6 - Festkörper," Walter de Gruyter, 2005, pp. 111-218.
- [26] U. Richter, T. Krause and W. Schempp, "Untersuchungen zur Alkalibehandlung von Cellulosefaser. Teil 1. Infrarotspektroskopische und röntgenographische Beurteilung der Änderung des Ordnungszustandes," *Die Angewandte Makromolekulare Chemie*, vol. 185, pp. 155-167, 1991.
- [27] W. Demtröder, "Laserspektroskopie 2," 6. ed., Heidelberg, Springer Spektrum, 2012, pp. 111-139.
- [28] K. Schenzel and S. Fischer, "NIR FT Raman spectroscopy - a rapid analytical tool for detecting the transformation of cellulose polymorphs," *Cellulose*, vol. 8, pp. 49-57, 2001.

- [29] K. Schenzel, S. Fischer and E. Brendler, "New method for determining the degree of cellulose I crystallinity by means of FT Raman spectroscopy," *Cellulose*, vol. 12, pp. 223-231, 2005.
- [30] L. Bergmann and C. Schaefer, "Lehrbuch der Experimentalphysik Band 3 - Optik," Walter de Gruyter, 2004, pp. 1031-1132.
- [31] G. Lang, "Histotechnik," Wien, Springer-Verlag, 2006, pp. 123-158.
- [32] *Courtesy of the Institute for Electron Microscopy and Nanoanalysis (FELMI-ZfE), TU Graz, Austria, www.felmi-zfe.at.*
- [33] S. Zhu, Y. Wu, Q. Chen, Z. Yu, C. Wang, S. Jin, Y. Ding and G. Wu, "Dissolution of cellulose with ionic liquids and its application: a mini-review," *Green Chemistry*, no. 8, pp. 325-327, 2006.
- [34] R. P. Swatolski, S. K. Spear, J. D. Holbrey and R. D. Rogers, "Dissolution of Cellulose with Ionic Liquids," *Journal of the American Chemical Society*, vol. 124, no. 18, pp. 4974-4975, 2002.
- [35] M. Köhler, "Nanotechnologie," Weinheim, Wiley-VCH Verlag GmbH, 2001, pp. 58-60.
- [36] E. Kontturi, P. C. Thüne and J. W. Niemantsverdriet, "Novel method for preparing cellulose model surfaces by spin coating," *Polymer* 44, pp. 3621-3625, 2003.
- [37] C. D. Edgar and D. G. Gray, "Smooth model cellulose I surfaces from nanocrystal suspensions," *Cellulose* 10, pp. 299-306, 2003.
- [38] E. Kontturi, L.-S. Johansson, K. S. Kontturi, P. Ahonen, P. C. Thüne and J. Laine, "Cellulose Nanocrystal Submonolayers by Spin Coating," *Langmuir* 23, pp. 9674-9680, 2007.
- [39] S. B. Engelsens, "Raman Spectra of Carbohydrates," [Online]. Available: <http://www.models.life.ku.dk/~specarb/cellulose.html>. [Accessed 13 11 2013].
- [40] P. Bubner, J. Dohr, H. Plank, C. Mayrhofer and B. Nidetzky, "Cellulases Dig Deep," *The Journal of Biological Chemistry*, vol. 287, no. 4, pp. 2759-2765, 2012.